2021

Measurement and Mitigation of Optical, Recombination and Resistive Losses in Silicon Photovoltaics

Mohammad Jobayer Hossain
University of Central Florida

University of
Central Florida

STARS
Showcase of Text, Archives, Research & Scholarship

MEASUREMENT AND MITIGATION OF OPTICAL, RECOMBINATION AND RESISTIVE
LOSSES IN SILICON PHOTOVOLTAICS

by

MOHAMMAD JOBAYER HOSSAIN
M.S. University of Central Florida, 2020
M.S. Tennessee Technological University, 2016
B.S. Khulna University of Engineering and Technology, 2012

A dissertation submitted in partial fulfilment of the requirements
for the degree of Doctor of Philosophy
in the College of Optics and Photonics
at the University of Central Florida
Orlando, Florida

Fall Term
2021

Major Professor: Kristopher O. Davis

ABSTRACT

Today, most of the photovoltaic cells in the market are made of silicon. Great achievements are being attained every year in terms of reducing the price of this kind of cells and improving their efficiency, reliability and durability. However, further improving the cell performance is a challenging task because of the presence of optical, recombination and resistive loss mechanisms in the cell. This work is focused on the measurement and mitigation of these losses.

Mitigation of the optical, recombination and resistive losses at first require quantifying those losses and their impacts on the cell performance metrics accurately. Traditionally, solar cells have been measured using characterization techniques like current-voltage, and Suns-V_{OC}, which express the performance metrics in terms of the global cell parameters for the entire cell. However, solar cell is a large area device and different parts on a cell produce different amount of electricity because of the nonuniform distribution of the crystalline defects over the cell and the process variations. Spatial distributions of the cell parameters are valuable because they provide the in depth information about the root causes behind the performance drop of a cell, and points to its remedy. Camera based luminescence imaging and point by point measurement of quantum efficiency and reflectance on the cell are used in this work to find the spatial distribution of the parameters. A new method of parameter imaging is implemented by incorporating the quantum efficiency scanning with the luminescence measurement. A comprehensive methodology to evaluate losses and process variations in silicon solar cell manufacturing is also presented here. The nature of the distributions and correlations in this study provide important insights about loss mechanisms in industrial solar cells, helping to prioritize efforts for optimizing the performance of the production line.

As an effort to mitigate the optical, recombination and resistive losses in the silicon solar cells, self-assembled multifunctional nanostructures are developed. These nanostructures can reduce

the optical losses in the near band edge, thus contribute in increasing the photogenerated current density. They also contribute in reducing the surface recombination loss by passivating the silicon surface. Additionally, they shows promising results in reducing spreading resistance, which eventually helps the charge transport mechanism in the cell.

An overview of the recent trends and endeavors in silicon photovoltaics is first given, followed by a chapter on the important concepts in silicon photovoltaics. The next chapter describes the solar cell manufacturing process and different performance issues related to it. Chapter 4 introduces different measurement techniques used for quantifying the optical, recombination and resistive losses. The following chapters present the crux of this work: method developed for measurement and mitigation of optical, recombination and resistive losses in silicon photovoltaics.

To Mom (Most Zobaida Begum), Dad (Md Jakir Hossain), and Grandpa (Abdul Karim Sarker),

who always encouraged me to think big and go on every adventure in life, especially this one.

ACKNOWLEDGMENTS

This thesis presents the research I have been conducting for the last several years. However, it could not have been finished without the help, support and guidance of many individuals.

I still remember the day I first talked with Professor Kristopher O. Davis about research. I am grateful that he kept trust in me and gave me the opportunity to work with him. He helped me find my area of interest from a wide variety of options in photovoltaics research and guided me throughout my PhD journey. Besides the technical skills, I closely observed his unique leadership style, which I believe is a valuable asset to succeed in career. Prof. Davis was kind enough to help me out whenever I faced a roadblock in my research. Throughout my PhD I enjoyed a collaborative and cordial relationship with Dr. Davis which made my time very productive. Although I have not directly worked with Professor Winston V. Schoenfeld in a project, my research has been extremely benefited by his labs, equipped with necessary characterization set ups. Prof. Schoenfeld is also the one who introduced me with Dr. Davis after knowing my interest in photovoltaics research. I greatly appreciate his support.

In the early stage of my PhD I attended the HOPE workshop at National Renewable Energy Laboratory (NREL). The speech of Dr. Pauls Stradins in that event gave a deep insight about different practical aspects of solar cell research. This later on helped me immensely in taking a direction in my research. I have been fortunate to have him on my committee and he continued giving advice whenever I needed. I feel lucky to have worked with Professor Pieter G. Kik and his group. His deep understanding of photonics and systematic way of conducting research has helped me immensely. I am also grateful to him for allowing me to use his lab when I needed. I would also like to express my heartiest grattitude to Professor Ronald Driggers and Professor C. Kyle Renshaw. Professor Driggers gave me great advice about research methodology and career prospects.

Professor Renshaw also asked good questions and gave important suggestions for laying out this dissertation.

Big thanks to Dr. Steven Johnston at NREL for giving me the opportunity to work with him on certain cell issues. Also thanks to Dr. Dana Sulas for helping me with some characterizations and sharing her insights. I conducted part of my research at Brookhaven National Laboratory under the guidance of Dr. Gregory Doerk. I appreciate all his mentorship and support during my stay there and afterwards. This work was also benefited from the characterization done by Adriene Blum of Sinton Instruments.

I would like to acknowledge Dr. Eric Schneller for his mentorship besides Dr. Davis. His help in learning tools and softwares has made my PhD journey a lot easier. I would also like to acknowledge the help and support I received from Dr. Haider Ali, Dr. Mengjie Li, Dr. Geoffrey Gregory, Nafis Iqbal, Dylan Colvin, Jannatul Ferdous Mousumi, Mengdi Sun, Rafaela Frota, Nicole Karam Pannaci. Be it a characterization or fabrication related help, putting a purchase order on my request, accompanying me setting up an instrument in the lab, or sharing your thoughts on something - all these have contributed to the successful completion of this dissertation. Thank you!

TABLE OF CONTENTS

LIST OF FIGURES

xviii

LIST OF TABLES

CHAPTER 1: INTRODUCTION

Today, electricity is a part and parcel of our everyday life. Without electricity we cannot think of most of the modern amenities we use; from home appliances, to communication media, industry, recreation, and healthcare. The means to produce electricity is limited, although the global energy consumption is rapidly increasing because of increase in population, rising prosperity and improvement in quality of life. Traditionally the major portion of the total electricity has been produced using the fossil fuels like coal, oil, and natural gas. However, there are two serious risks in using fossil fuels. First, their reserve being limited, they are diminishing day by day posing threats to the advancements of the future human civilization. This necessitates the quest for sustainable alternatives. The second risk is on our existence. We have already seen the negative consequences of burning fossil fuels on our environment. We must focus more on developing renewable energy sources to combat problems like global warming, climate change, diseases and natural calamities occurring due to environmental pollution. It is great to see that global renewable energy production has been rising rapidly in the recent years as illustrated in figure 1.1. Also, thanks to the recent fact sheet published by the White House, the United States has set a target of reaching 100% carbon free electricity generation by 2035 [3].

Solar, wind, water, geothermal and bio-energy are the notable renewable energy sources. As compared to fossil fuels, these renewable energy sources are unlimited and available in nature. Solar energy is of the greatest potential among these sources. It has appeared as the most rapidly growing renewable energy source, although it is still behind the wind energy as depicted in figure 1.2. There are several reasons behind solar energy's rapid growth. Firstly, solar electricity can be produced anywhere. Secondly, solar panels are simpler to install in comparison with wind turbine or hydro-power dams. Thirdly, the operation is silent as no mechanical motion is involved. Fourthly, the systems have longer lifespan. Fifthly, lesser maintenance is required than it's other renewable
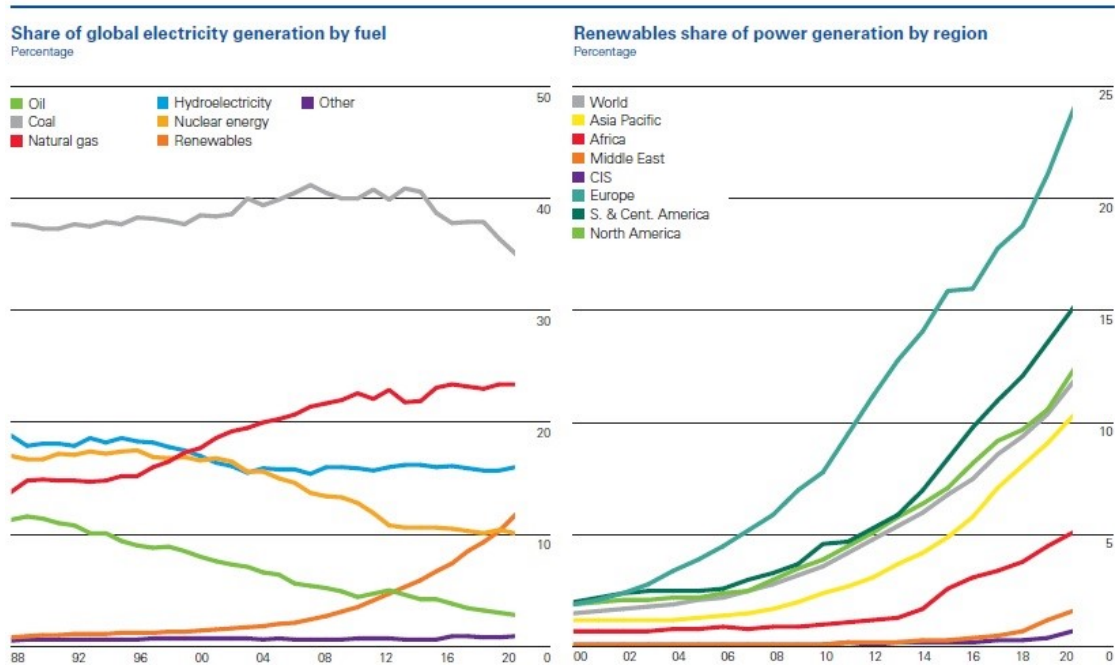
Figure 1.1: Global energy generation trend over the recent years (reproduced from [19]). X-axis represents the years

energy counterparts.

The light coming from the sun is the most abundant energy resource on earth. In a given year, roughly 885 million terawatt-hours (TWh) of solar energy reaches the earth's surface [87], which is 5277 times greater than the energy consumed by mankind in 2018 [2] and 4200 times the energy human civilization would need in the year 2035 [10]. The sunlight that falls on earth in just 1 hour and 25 minutes would be sufficient to meet the global energy demand in a whole year, if the full potential of that sunlight could be utilized.

Despite having huge potential, only a small portion of solar energy is utilized to generate electricity. As of the year 2021, global solar electricity share is only 3.2% [19], which was even lower in the previous years. The main reason behind this was the high installation costs of the photovoltaic
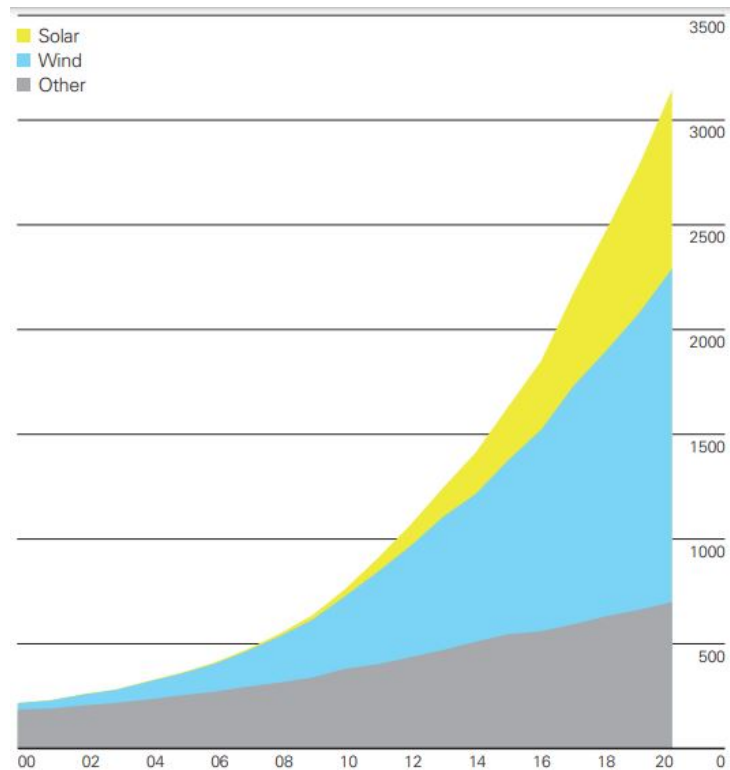
Figure 1.2: Renewable energy trend over the recent years (reproduced from [19]). Y-axis represents the energy produced in TWh and X-axis represents the years

(PV) systems, although there is no fuel cost associated with solar electricity. In contrast, the coal, oil and natural gas based powerplants being established many years ago were selling electricity at a cheaper price. However things have been changed drastically in the recent years. Thanks to the public awareness about the environment and the government subsidies PV industry received initially. With the initial frameworks completed and the remarkable advances in PV technologies by the academic and industrial research, the last couple of years have seen a huge decline in the PV electricity price. Figure 1.3 illustrates that the solar electricity continues to decline for all the residential, commercial, and utility-scale PV systems; the decline is driven largely by both the increased module efficiency and lowered hardware costs. PV energy conversion has appeared as

3
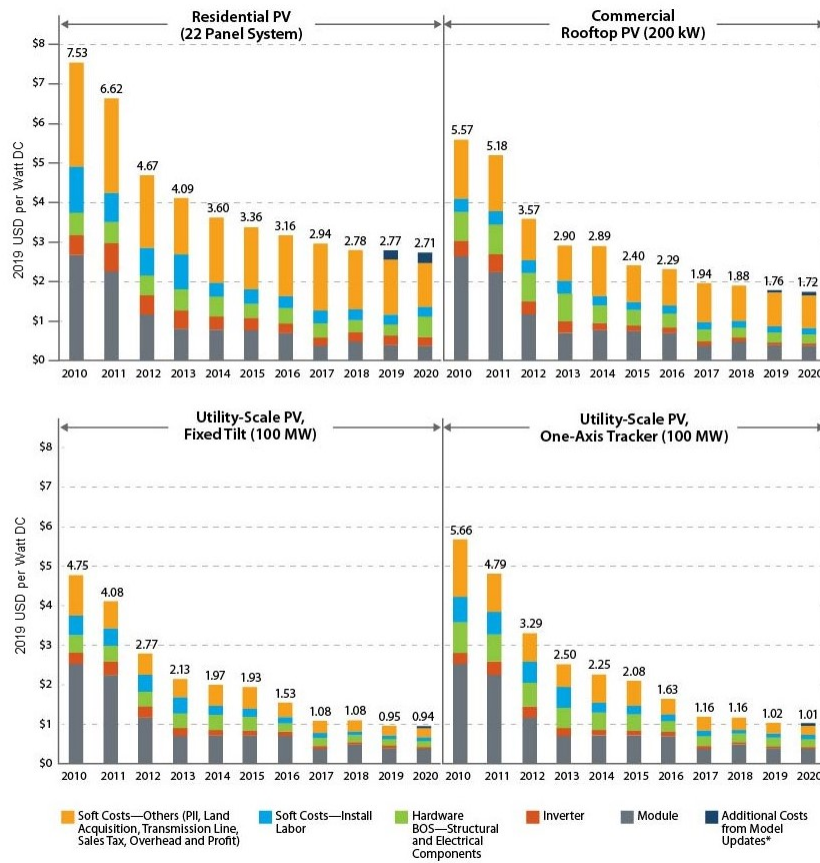
Figure 1.3: NREL PV system cost benchmark summary (inflation-adjusted), 2010–2020. Y-axis represents the 2019 USD per Watt DC [49]

the cheapest source of electricity recently [44]; even cheaper than the fossil fuel based electricity generation. Today, utility-scale PV (fixed-Tilt) electricity costs less than 0.94$ per W(DC). In 2020, the global PV market size was USD 170.55 billion, which is expected to reach USD 293.18 billion in 2028 [4].

Sunlight is abundant on earth and PV cells can convert the incident photons into electricity. A wide variety of materials are used for making PV cells. These are organic materials, perovskites, III-V semiconductors, Silicon (Si) etc. Although all these materials follow a similar light-matter

4

interaction principle for photo-current generation, Si has appeared to be the most used material for PV cell manufacturing. Today more than 95% PV cells in the market are made of Si [133]. There are several reasons behind this dominance. Firstly, Si is the second most dominant material on earth. Secondly, there is no concern of toxicity in using Si. Thirdly, Si has a bandgap which is very close to the optimum bandgap required for solar electricity generation at AM 1.5G solar spectrum. Moreover, it leverages from the technologies already developed in the well-established semiconductor industry.

The most influential factor in the solar electricity price calculation is efficiency of the cell. The module manufacturing and installation costs being almost saturated, the price in dollar per watt is heavily influenced by the efficiency of the cell. Figure 1.4 demonstrates the increase in crystalline silicon solar cell efficiency over the years. Thanks to the efforts of the academic and industrial researchers. The present world record of the silicon solar cell efficiency is 26.7% [173] with a heterojunction structure, when the highest efficiency limit of such a cell is about 30% [140] at AM 1.5G solar spectrum. The difference between the practical value and the Shockley–Queisser limit could be reduced to a great extent by mitigating optical, recombination and resistive losses occurring in the solar cells. The next important area of research that contributes to reducing the electricity price is the development of less expensive manufacturing processes and better measurement methods that is crucial for in line testing of the quality of the cells and modules produced. There is also another arena of PV research that is helping reduce the solar electricity price significantly. Currently the average lifetime of a PV cell is about 20 years and performance of a cell keeps degrading over its life span. Therefore, if the the degradation pathways are identified and stopped, the total throughput of a PV system increases and it leads to a lower dollar per watt.

The main fuel of a PV cell is the photons coming from the sun and being incident on it. The wavelength of these photons ranges from ultraviolet to infrared domain, including the visible domain. However, not all the incident photons can enter the cell, because part of it is reflected by the front
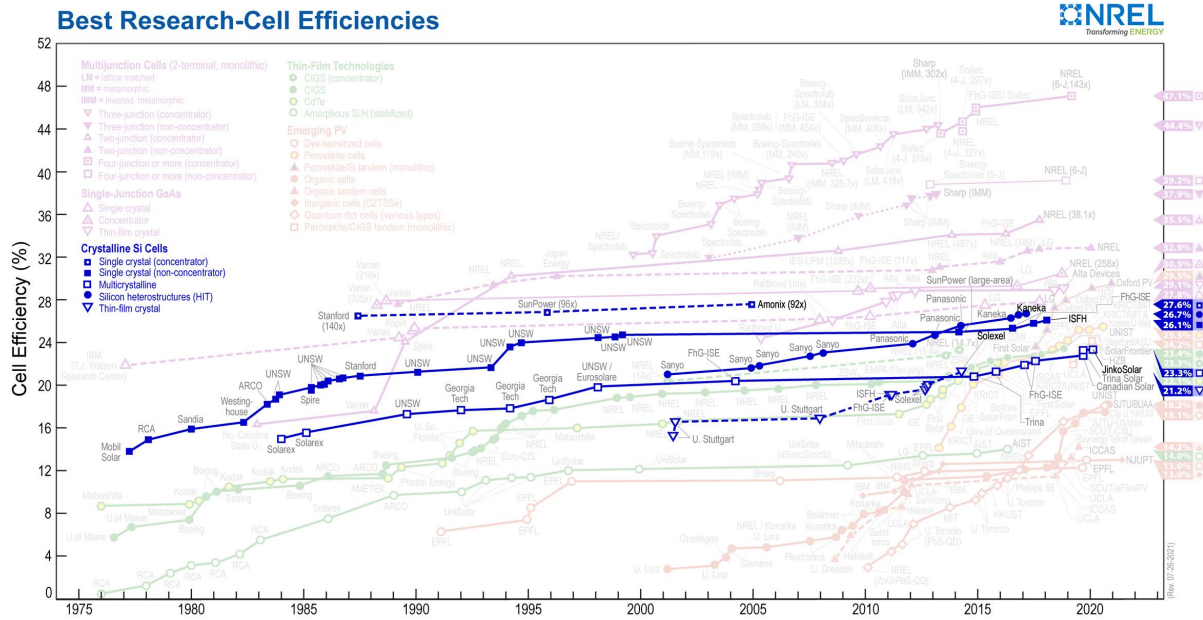
Figure 1.4: NREL best cell efficiency chart of crystalline silicon cells. This plot is courtesy of the National Renewable Energy Laboratory, Golden, CO

surface of the cell. Also, not all the photons entering the cell can be absorbed by it and converted to electron-hole pair, because only the ones having energy more than the bandgap of the material can be absorbed (for Si, it is 1.1 eV, or in other terms 1129 nm), considering a thick enough cell. However, because of the price constraints, cells are not made very thick, as a result the cells cannot utilize all the photons incident on it (optical loss). Because Si solar cells are made of thin silicon wafers sliced from Si ingots, the dangling bonds on those wafers leads to surface recombination loss in the cells. Different other nonradioactive recombination loss also occur in a cell due to the presence of the crystalline defects, dislocation centers, etc. Another form of loss occurs in a cell called resistive loss which occurs due to the non-zero resistance the photogenerated carriers (i.e., electrons and holes) face when they are extracted from the cell to the external circuit. All these losses contributes to the reduction in the efficiency of a cell and steps must be taken to mitigate them in order to obtain a high efficiency cell.

Efficient and quicker measurement methods play important role in the efforts to manufacture high efficiency and low cost solar cells. The manufacturing process of a solar cell is complex and comprises of many steps taken at controlled environment. In each of these steps they are measured and inspected for flaws. In an event when a wafer or cell does not pass the threshold, it is immediately discarded to avoid further use of resources for it when it is obvious that that cell is going to be invalid. Outside of these in-line measurement, performance monitoring of a cell or module (which is basically a group of cells working together) is also crucial to detect issues like cracks, and degradation.

In this work, new methods of measuring solar cells and modules are developed based on the luminescence and quantum efficiency characteristics. These methods are utilized to evaluate losses and process variations in a large number of cells and modules. A novel method of mitigating the optical, recombination and resistive losses is also developed, which shows the potential of increasing solar cell efficiency. These works are presented in the next chapters.

CHAPTER 2: IMPORTANT CONCEPTS IN SILICON PHOTOVOLTAICS

A solar cell produces voltage and current by absorbing photon and then converting it into electricity through a process called photovoltaic effect. This effect was originally demonstrated by Edmond Becquerel in 1839 and the first solar cell with a poor efficiency was made of selenium covered with a thin film of gold. Today solar cells are made of numerous materials, silicon solar cells being the dominant in the market.

The photovoltaic effect and the amount of the electricity produced depends on several complex mechanisms related to light-matter interaction, band to band transition, recombination processes and carrier transport. It is crucial to study and understand the structure and underlying physics of solar cells in order to engineer them to be highly efficient.

Sunlight

Light from sun is the major source of energy on earth. Sun is a giant sphere filled with hot plasma, which is continuously radiating a huge amount of energy in every direction. The radiation is isotropic in nature. However, because of the great distance it travels (approximately 150 million kilometers) before it reaches the earth, only the light that travels directly towards the earth's surface reaches it. With the temperature of 5777K on its surface, the sun can be considered as a black body. Therefore the energy density on sun's surface, W_s can be calculated using Stefan-Boltzmann law,

$$W_s = \sigma T^4 \tag{2.1}$$

Here, σ is the Stefan-Boltzmann constant ($5.67x10^8 \ Wm^{-2}K^{-4}$). Putting T=5777K in equation
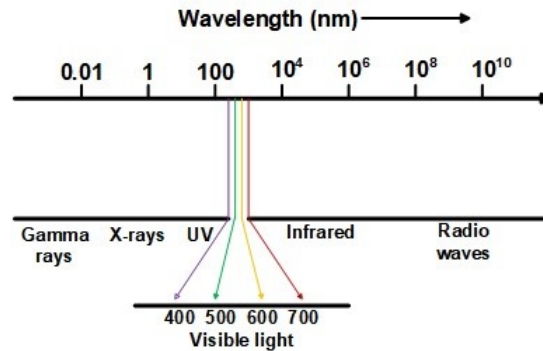
Figure 2.1: The relative position of sunlight in the electromagnetic spectrum

2.1, we find that an enormous amount of 63.15 MW power emits from just one square meter area on sun's surface. This after spreading much and facing lots of attenuation along the way when reaches earths atmosphere, the energy density falls into a number 1353 W/m^2 [67]. On the earth's atmosphere it further experiences reflection, scattering and absorption. Therefore when it reaches sunlight directly, the energy density falls to about 1000 W/m^2. Figure 2.2 illustrates the solar spectrum at different distance from earth's surface. The extraterrestrial solar spectrum (also known as AM0) represents the solar spectrum outside of the earth's atmosphere. The global tilt (also known as AM1.5G) and direct+circumsolar (also known as AM1.5D) are solar spectrum on earth's surface, both of them suffering from atmospheric absorption in certain wavelength regions (i.e., dips in the spectrum). When the direct+circumsolar spectrum only accounts for the direct illumination, the global tilt spectrum includes the diffuse component as well.

Light is an electromagnetic wave whose wavelength lies between gamma rays and radio waves. The radiation from sun ranges from 200 nm to 2500 nm wavelength. However, most of the solar energy lies in the visible wavelengths (400-700 nm). Its amazing that rod and cone cells in our eyes are sensitive to this wavelength range.
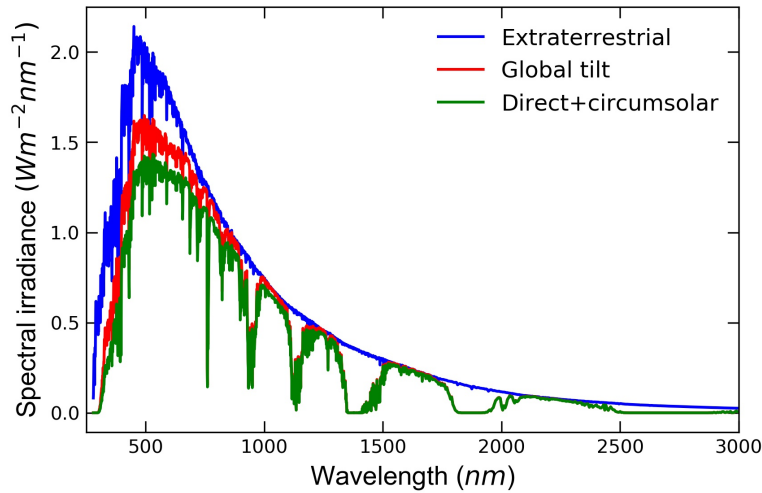
Figure 2.2: Solar irradiance at different distance from earth's surface (courtesy of ASTM International [101])

In the particle model of light, it consists of discrete energy packets called photons. Photons are mass-less and charge-less entity that interact with matters and discrete particles ((e.g. electrons, atoms and molecules)) on their way. The wave-particle duality of light allows us to calculate the energy of a photon E using this equation,

$$E = \frac{hc}{\lambda} \tag{2.2}$$

Here, h is the Planck's constant (6.625 x 10^{-34} Js), c is the speed of light in vacuum (2.998 x 10^{8} ms^{-1}), and λ is the wavelength of light. This equation expresses photon energy in Joules.

However, is is very common to express photon energy in electron-volts (eV) as well. One eV is the energy acquired by an electron when it is accelerated through a potential difference of 1 V (1 eV = 1.60218 × 10^{-19} J).

Solar Cell Structure

In simplistic view, a solar cell is semiconductor device that is made by sandwiching n-type emitter with a p-type base layer. Here, the n-type and p-type layers could be either the same material or different materials. The ones with different materials are called heterojunction solar cells, and the ones with the same material is called homojunction cells. The emitter of a solar cell is usually made of higher doping but lesser thickness than the base layer. Figure 2.3(a) illustrates the schematic of a cell. The front side of a cell is usually textured to reduce front reflection loss. In addition to texturing, an anti-reflection coating (around 70 nm) is also used to suppress the front reflection further. Front and rear contacts are fabricated to collect the photogenerated carriers (i.e. electrons and holes).

A solar cell is made by sandwiching an n-type emitter with a p-type base layer. The emitter is made of higher doping but lesser thickness than base layer. Sunlight enters into the cell from the emitter side. An antireflection (AR) coating layer is used to minimize light reflection into the cell. Without this layer, much of the light would bounce off the surface of the cell. While designing an AR coating layer, the refractive index and the thickness of the material are the two most important things to be considered.

Figure 2.3(b) demonstrates the front side of a practical silicon solar cell. The area of such a cell is 15.6 cm x 15.6 cm and thickness is 180 um. As depicted in the figure, metallic gridlines (usually made of Ag) with an width of approximately 60 um is fabricated on the front side to collect the carriers. These gridlines are connected to a wider contact path called basbar. Based on grid design, number of basbar varies from 2 to 5. They transfer the collected carriers to the external circuit. In the zoomed in view of the front side, gridlines are oriented vertically and two basbar are oriented horizontally. In a typical industrial Si solar cell, the front metal contacts block around 5% of the incident light [89, 90]. The entire rear side is usually covered by the rear side contact. Since the

11
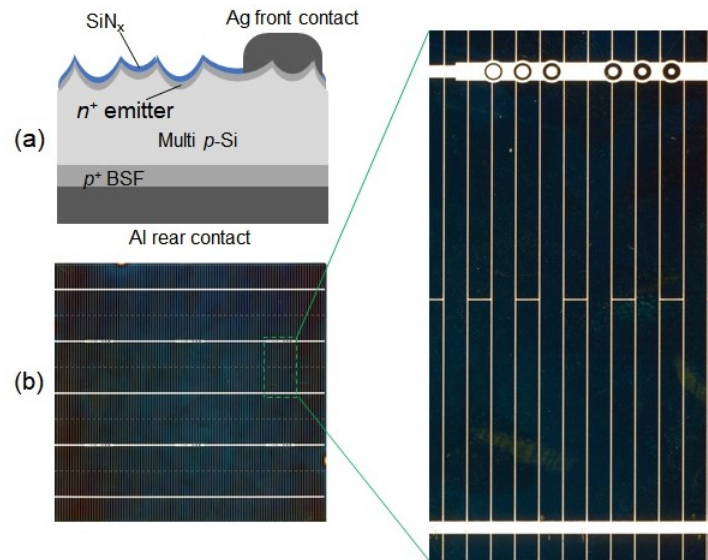
Figure 2.3: Solar cell structure (a) schematic (b) a practical silicon solar cell

entire rear side is metalized, the conductivity of the metal does not have to be as high as of Ag. Using Al provides sufficiently low resistance in the rear contact.

Semiconductor Physics

Solar cell is a semiconductor device capable of absorbing light and transforming it into electricity. This transformation happens though a complex light matter interaction involving absorption, electron-hole pair generation, recombination and carrier transport mechanism. It is crucial to study and understand the underlying semiconductor physics of solar cells for engineering them to be better.

Band Structure and Bandgap Energy

The electrons of an isolated atom occupy the atomic orbitals having discrete energy levels. When two such atom form a diatomic molecule, their atomic orbitals overlap. According to Pauli exclusion principle, no two electrons can have the same quantum number. Therefore an atomic orbital in such a molecule splits into two molecular orbitals of different energy levels and electrons now occupy these new orbital structure. In a crystal lattice a large number of atoms are bonded with each other by covalent bonds. Comparing with the diatomic molecule, Pauli exclusion principle for a crystal lattice suggests that there are a large number of energy levels that an electron occupy. The energy of the neighboring levels are very close to each other and can be treated as a band of energies. It is worth mentioning here that the formation of the bands is an aspect related to the electrons on the outermost shells, as these are the electrons whose orbitals overlap the most when the atoms bond with each other; the inner orbitals do not affect much.

Now, at absolute zero temperature, all the outer shell electrons (also called as valence electrons) of a semiconductor crystal are tightly bound to the nuclei. They cannot conduct and the semiconductor acts as an insulator. In this situation, all the electrons lie in the valence band and no electron in the conduction band. In case of the nonzero temperature, some of the electrons are excited due to the thermal energy and can move along the crystal; in other words, these electrons occupy the conduction band. Because of the finite width of the energy bands, there appears certain range of energy which no electron can occupy. This range is called the forbidden energy gap or bandgap energy of the semiconductor. The lowest energy level in the conduction band is denoted by E_c and the highest energy level in the valence band is denoted by E_v. Therefore, the bandgap energy of a semiconductor,

$$E_g = E_c - E_v \tag{2.3}$$

Bandgap energy is the lowest energy required to make a transition from valence band to conduction band. This required energy can be provided in the form of light, heat, etc. In the semiconductor materials, the band to band transition can occur in two different ways. Based on the transition process semiconductor materials are classified into two types: direct bandgap and indirect bandgap semiconductor.

Direct and Indirect Bandgap Semiconductor

It was mentioned earlier that the energy-momentum (E-P) relation follows a parabolic curve. Direct bandgap semiconductors are those semiconductor materials in which the valley of the conduction band and the peak of the valence band lie in the same momentum, as illustrated in figure 2.4(a). Band to band transition are easy in such a material; if suficient energy (greater than the bandgap energy) is provided to an electron in the valence band, it reaches the conduction band leaving behind a hole in the valence band (in other words, it starts conducting). Examples of direct bandgap semiconductors are InAs, GaAs, GaP, CdTe, etc [87]. An indirect bandgap semiconductor on the contrary is little different. The peak of the valence band and the valley of the conduction band are not lined up in the same momentum (figure 2.4(b)). Therefore, a band to band transition is not certain even though sufficient amount of energy is provided to the electron in the valence band. An electron can achieve the momentum required through either phonon (lattice vibration in simplistic view) absorption or phonon emission. Si and Ge are two well known indirect bandgap semiconductors. Because of the dependency on phonons, the band to band transition rate is lower in indirect band semiconductor than the direct band semiconductors.
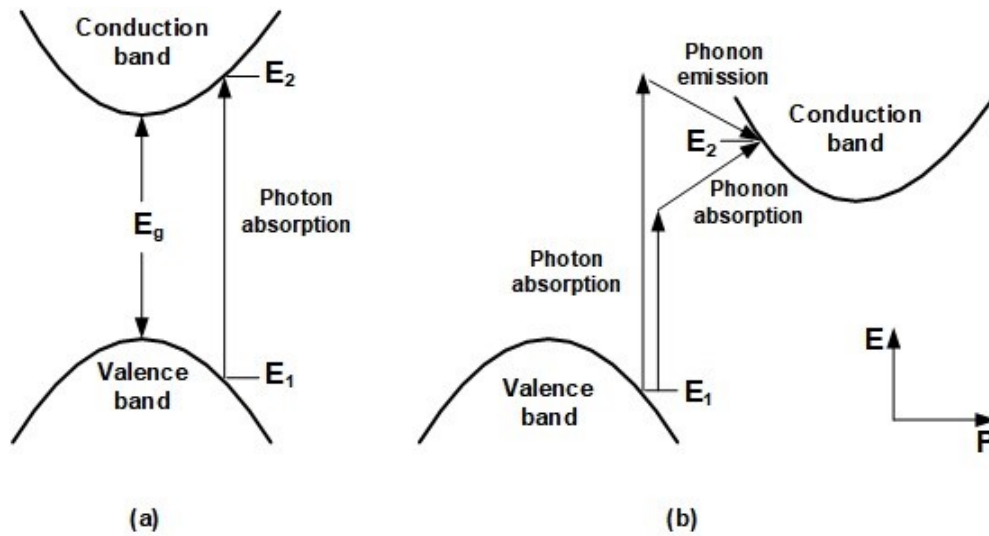
Figure 2.4: Band diagram of semiconductor materials of two types (a) direct bandgap (b) indirect bandgap

Optimum Bandgap for Single p-n Junction Solar Cell

Efficiency is the parameter of most interest in a solar cell. There are a wide variety of materials in nature, both direct bandgap and indirect bandgap type, which can be used to make solar cells. Therefore it is important to identify the most promising material that can provide the highest efficiency. William Shockley and Hans J. Queisser conducted a theoretical study in 1961 that established the relationship between the efficiency and the bandgap of the material, and calculated the highest possible efficiency [149]. They made the assumption that every incident photon that has the energy higher than the bandgap of the material is absorbed by that material and it produces one electron-hole pair. With this assumption, the ultimate efficiency of a single junction solar cell η can be expressed as,

$$\eta = \frac{h v_g Q_s}{P_s} \tag{2.4}$$

15
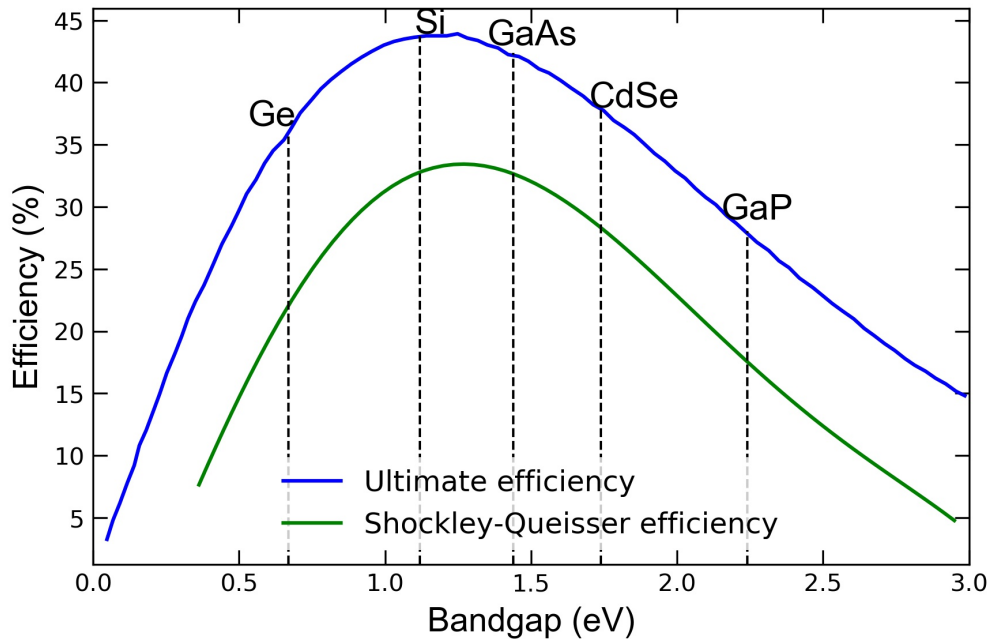
Figure 2.5: Dependence of efficiency on bandgap energy

Here, h is the Planck's constant, ν_g is the frequency representing the bandgap energy. Q_s is the photon flux, counting only those photons which has energy more than the bandgap energy and P_s is the total input power. The ultimate efficiency of a p-n junction solar cell is plotted in figure 2.5. We notice that the maximum efficiency of 43.9% could be achieved using a material of bandgap energy 1.24 eV. This is very close to the bandgap energy of Si (1.12 eV). The ultimate efficiency calculation does not consider the radiative recombination in the semiconductor materials, which is an inherent property. The efficiency with the consideration of radiative recombination is widely known as the Shockley–Queisser efficiency limit. As illustrated by the green curve in figure 2.5, the Shockley–Queisser limit for Si solar cells is 33.4%. The efficiency of solar cells for other materials are also denoted in the figure. We see that Si is the ideal material for solar cells. There has been a recent study which reevaluated the efficiency limit with the considerations of Auger recombination and the intrinsic carrier concentration [140]; these considerations were missing in
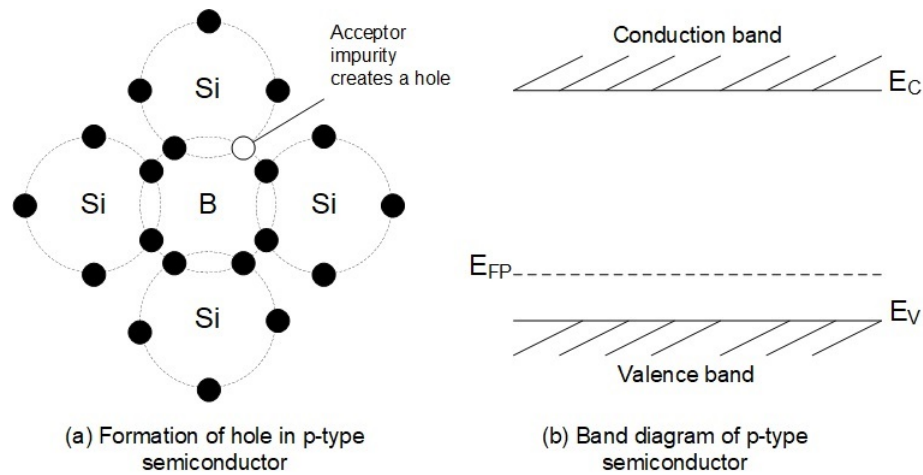
Figure 2.6: p-type semiconductor (Si) and it's band diagram

the previous studies. In this new study, the limiting efficiency of a Si solar cell became 29.43%, with a 110 um thickness. The current world record of the practical Si solar cell is 26.7% [173]. The industrial Si solar cells are also approaching this fundamental efficiency limit, with the efficiency values ranging from 16.5% to 22.5% [168, 17]. Multijunction solar cell structures [95, 155] have emerged as a way to increase the fundamental efficiency limit associated with a single junction cell. These multijunction cells use multiple materials with comparable lattice constants, where the material with the highest bandgap energy absorbs the blue light and the material with the lowest bandgap energy absorbs light in the infrared region, and so on.

Doping

Doping is a widely used process in optoelectronic devices, which is basically the addition of small number of foreign atoms to an intrinsic semiconductor. It changes the characteristics of a semiconductor material considerably. Depending on what impurity is used for the doping, the doped semiconductor are called either p-type or n-type.

17
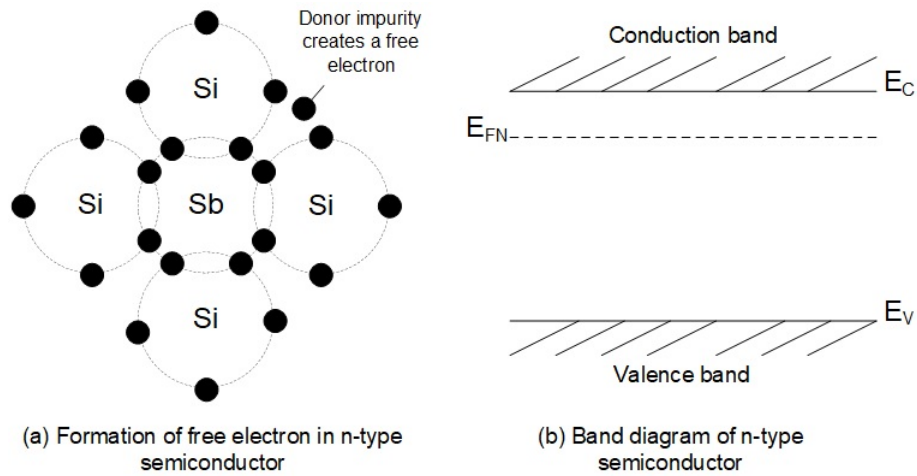
Figure 2.7: n-type semiconductor (Si) and it's band diagram

p-type semiconductor

When a trivalent atom, for example boron (B) is added to the crystal lattice of a semiconductor material like Si, the three outer shell electrons make bonding with four neighboring Si atoms, leaving a vacant space as illustrated in figure 2.6. The absence of electron created this way is called a hole, and the semiconductor (Si in this case) is called a p-type semiconductor. A hole behaves like a separate, positively charged particle with its own dispersion curve and effective mass. P-type doping removes some electrons that occupy the top of the valence band states. As a result, to account for this occupancy change, the Fermi level in the Fermi-Dirac distribution shifts closer to the valence band as illustrated in figure 2.6(b).

n-type semiconductor

When a pentavalent atom, for example antimony (Sb) is added to the crystal lattice of a semi-conductor material like Si, the four outer shell electrons make bonding with four neighboring Si

atoms, leaving a free electron as illustrated in figure 2.7. The free electron created this way can move along the crystal. The semiconductor (Si in this case) is now called a n-type semiconductor. N-type doping adds some electrons at the bottom of the conduction band states. As a result, to account for this occupancy change, the Fermi level in the Fermi-Dirac distribution shifts closer to the conduction band as illustrated in figure 2.7(b).

Carrier Generation and Transport Mechanism in Solar Cells

A large part of how well a particular material will act as a solar cell depends on its light absorption capability. The valence and conduction bands overlap in the metals and there is no band to band transition when sunlight falls on a metal. Therefore, they are not suited for solar cell applications. The bandgap in the insulators on the other are too high to satisfy for an incident photon. Semiconductors are great for both light absorption and carrier transport, their electrical and optical properties being easily engineered by doping, bandgap engineering and other approaches.

The amount of light absorbed by a semiconductor is expressed by its absorption coefficient, α. Higher value of α means the semiconductor is more absorptive. If light of intensity I_0 impinges on a piece of semiconductor then it's intensity I after travelling certain distance x becomes,

$$I = I_0 e^{-\alpha x} \tag{2.5}$$

Now, α of a material depends on the extinction coefficient (the imaginary part of the refractive index) of that material, κ.

$$\alpha = \frac{4\pi\kappa}{\lambda} \tag{2.6}$$

Equation 2.6 shows that the absorption coefficient is a wavelength dependent parameter. Not all the wavelengths are absorbed by the material in the same rate. One thing is crucial for the absorption

though, the wavelength of the light has to be such that the photon energy (as written in equation 2.2) is at least equal to the bandgap of the material.

When a photon of energy more than the bandgap energy fall on a semiconductor, the electron in the outer shell starts conducting leaving behind a hole in the valence band (in other words, the electrons are excited to the conduction band). These generated carriers move along the semiconductor and they needs to be collected to the external circuit before they loose their energy through recombination process (described later). In a typical Si cell, the emitter is heavily doped n$^+$, the base wafer is p doped and the rear side is highly doped p$^+$. This arrangement creates two junctions, one in the front (n$^+$-p) and the other one in the rear side (p-p$^+$) is a high-low junction. These two junctions collect the photogenerated holes and electrons respectively.

Now, under external excitation (e.g., illumination), the energy of the electron and hole are characterized by the quasi Fermi energies E$_{FN}$ and E$_{FP}$. The concentration of electron and hole can be expressed as,

$$n_0 + \Delta n = N_C \ exp \left[\frac{-(E_C - E_{FN})}{KT} \right] \tag{2.7}$$

$$p_0 + \Delta p = N_V \ exp \left[\frac{-(E_{FP} - E_V)}{KT} \right] \tag{2.8}$$

Here, n_0 and p_0 are the concentration of electron and hole in equilibrium respectively. Also, $\Delta n = \Delta p$ are the corresponding excess concentration under excitation, k is the Boltzmann constant, and T is the temperature. Multiplying equation 2.7 and 2.8 we obtain,

$$(n_0 + \Delta n)(p_0 + \Delta p) = N_C \ N_V \ exp \left[\frac{-(E_C - E_V)}{KT} \right] exp \left[\frac{(E_{FN} - E_{FP})}{KT} \right] \tag{2.9}$$

Or,

$$(n_0 + \Delta n)(p_0 + \Delta p) = n_i^2 \ exp \left[\frac{(E_{FN} - E_{FP})}{KT} \right] \tag{2.10}$$

20
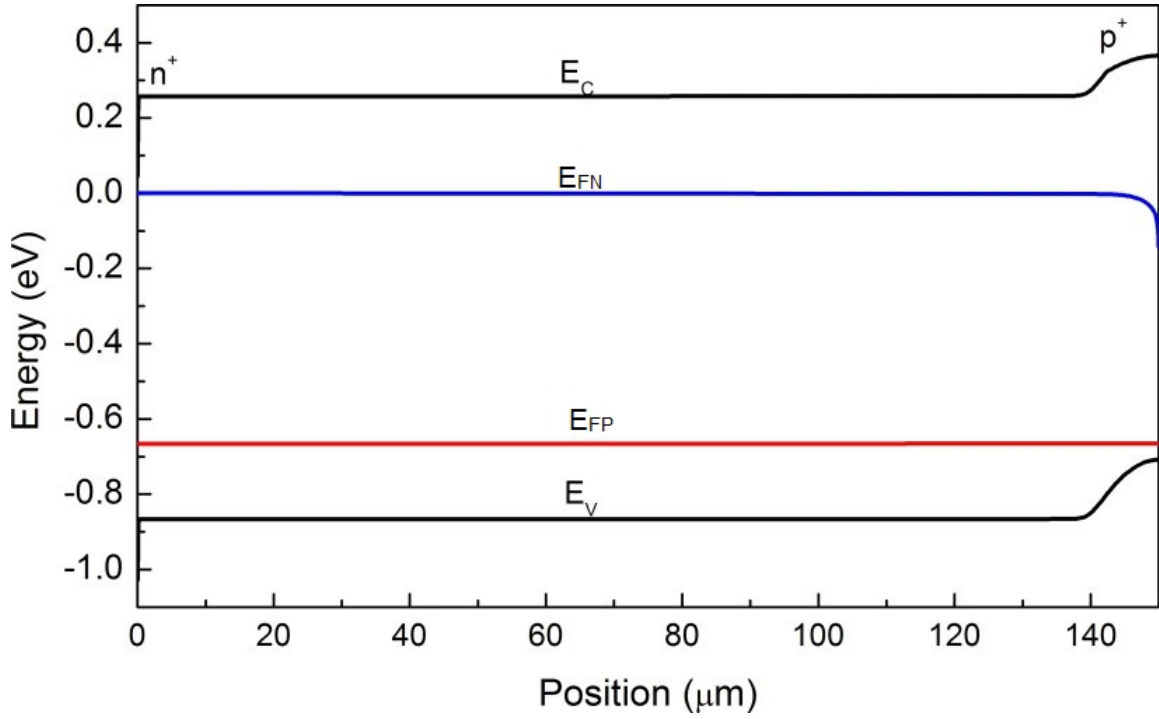
Figure 2.8: Band diagram of a 150-um-thick n$^+$pp$^+$ Si solar cell in open-circuit conditions having negligible recombination at the front n$^+$ region and a 10-um-thick p$^+$ region at the rear side (reproduced from [32])

Here n_i is the intrinsic carrier density. In equation 2.10, there is no E_C or E_V term. Therefore, the maximum open circuit voltage (iV_{OC}) attainable from a cell depends on the energy of the quasi Fermi levels, E_{FN} (minority electron quasi Fermi level) and E_{FP} (minority hole quasi Fermi level).

$$iV_{OC} = \frac{E_{FN} - E_{FP}}{q} \tag{2.11}$$

Here, q is the charge of an electron ($1.6x10^{-19}$ Coulomb). The practical implication of this equation is, even if the energy of a photon causing the band to band transition is very high, the maximum voltage we can obtain from a cell will be equal to the quasi Fermi level splitting. The band diagram of a silicon solar cell having p$^+$ BSF is illustrated in figure 2.8. Now, the driving force behind the

electron current is the gradient of the electrochemical potential of electron, which is equa to E_{FN} [32]. Similarly, the driving force behind the hole current is the gradient of the electrochemical potential of hole, which is equa to $-E_{FP}$. Considering the carrier mobility in only x direction, we can express the electron and hole current as,

$$J_n = \mu_n \, n \, \frac{dE_{FN}}{dx} \tag{2.12}$$

$$J_p = \mu_p \, p \, \frac{dE_{FP}}{dx} \tag{2.13}$$

Here, μ_n and μ_p are the electron and hole mobilities respectively. It worth's mentioning here that the gradient of the electrochemical potential is small in the base region (p doped) of the cell and is limited by the photocarrier generation under standard illumination. However, the gradient his very high near the rear contact.

Carrier Recombination Process and Pathways in Solar Cells

Not all the photogenerated carriers can contribute to the photocurrent that is extracted, some of them are lost through recombination processes. An electron in the conduction band of a semiconductor stays in a meta-stable state, which makes it very vulnerable to loss of energy very quickly. Recombination is the process by which an electron in the conduction band meets a hole in the valence band and then both of them become annihilated. The annihilation process gives energy which is either lost or reused, depending on the type of the recombination. In a broad sense, recombinations can be classified into two types:

1. Radiative recombination

2. Nonradiative recombination
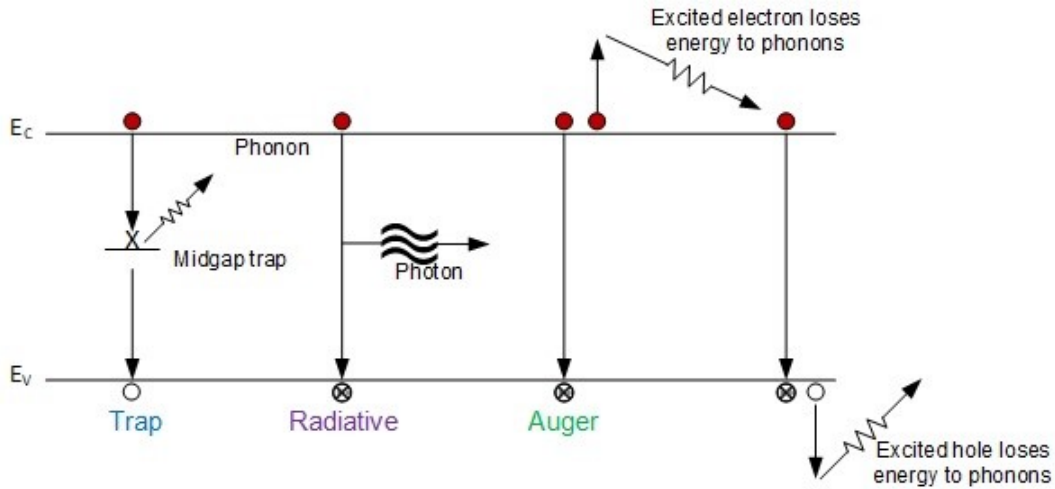
Figure 2.9: Recombination pathways in solar cells

Radiative Recombination

In the radiative recombination process, the energy from electron and hole annihilation emits in the form of light, a process very similar to how spontaneous emission works in a light emitting diode. The energy of the photons emitted depends on the energy of the electron and holes recombined. The photons emitted, if they have sufficient energy, can excite electrons sitting in the valence band again.

The rate of radiative recombination R_{rad} can be expressed as,

$$R_{rad} = B(pn - n_i^2)$$
(2.14)

Here B is called the radiative recombination constant, n_i is the intrinsic carrier concentration, and n and p are the concentration of free electrons and holes respectively. From this equation, we understand that increasing the electron and hole concentration increases radiative recombination.

Nonradiative Recombination

In this type of recombination, no photon is emitted due to the annihilation of the electrons and holes, rather the energy is lost through excitation of phonons (i.e., lattice vibration). Nonradiative recombination can further be classified into two types:

(a) Shockley-Read-Hall recombination

(b) Auger recombination

Shockley-Read-Hall Recombination

It is very common to have crystalline defects, dislocation centers and traps in the solar cell and the wafers they are made from. When an excited electron conducting in the semiconductor meets such a defect, dislocation center or trap, it loose its energy through phonon emission. This kind of recombination may occur both on the bulk of the semiconductor, or the unpassivated surfaces where there are danging bonds.

Auger Recombination

The Auger recombination is similar to the radiative recombination, except the fact that the emitted energy is given to another carrier in the conduction or valence band. This carrier (either electron or hole) then relaxes through thermal loss. The rate of the Auger recombination can be written as [151],

$$R_{rad} = (C_n n + C_p p)(pn - n_i^2) \tag{2.15}$$

Here, n is the free electron concentration, p is the free hole concentration. C_n and C_p are the Auger coefficients. We come to the conclusion that, if carrier concentration increases due to either

24

excessive doping or increased intensity of the incident light, Auger recombination increases. This process is the dominant recombination pathway in the emitter as it's doping level is relatively higher than the base region.

Minority Carrier Lifetime

In the solar cell operation, minority carriers (electrons and holes) are accumulated in two different sides of the cell. Since these carriers stay in a meta-stable state, they can loose their energy through recombination. So, they have to be extracted from the cell before they recombine. The time between the generation of the carriers and their recombination is called the minority carrier lifetime, or just carrier lifetime. It is a very important parameter that heavily influences solar cell performances.

In a material where the number of minority carriers is less than the doping (called a low level injection material), carrier lifetime τ is directly proportional to the excess carrier concentration Δn and inversely proportional to the recombination rate R.

$$\tau = \frac{\Delta n}{R} \tag{2.16}$$

However, as described earlier, recombination may occur through different pathways. Therefore, the minority carrier lifetime can be expressed as,

$$\frac{1}{\tau} = \frac{1}{t_{rad}} + \frac{1}{t_{nonrad}} = \frac{1}{t_{rad}} + \frac{1}{t_{SRH}} + \frac{1}{t_{Auger}} \tag{2.17}$$

Also, recombination occurs in both the surface and the bulk of the semiconductor. The lifetime

can also be expressed as following,

$$\frac{1}{\tau} = \frac{1}{t_{bulk}} + \frac{1}{t_{surface}}$$ (2.18)

Solar Cell Optics: Photon Management

Need for Photon Management

An important solar cell performance metric, short-circuit current density (J_{SC}) is proportional to the number of photons absorbed by the absorber material (eg., Si). A planar Si surface reflects about 30% to 50% of the incident light depending on the wavelength. This huge portion of the incident light cannot be absorbed by the cell and converted into electricity. Therefore necessary mechanisms have to be deployed in order to reduce the reflectance of the front side of the cell. Now, silicon is an indirect band-gap material, which makes its absorption coefficient drop rapidly when the incident wavelength approaches the band gap energy. It means required thickness for absorbing all the photons (or in other words, absorption length, L) increases rapidly with wavelength, λ. To illustrate further, for λ =800 nm, L=10 um whereas for λ =1100 nm L=3 mm [176]. Using a very thick silicon wafer in the order of 6 mm could ensure absorption of all the light over the band-gap. However, it is not suitable in terms of both the carrier transport and the cost i.e. photogenerated electrons and holes now have to travel a greater distance and by doing so they loss their energy through recombination process. A rear side reflector+deflector that reflects light at an angle greater than the critical angle solves this problem. It provides the cell with a few more chances of absorbing the long wavelength photons which were not absorbed in the first pass. The quality of a reflector is measured in terms of the path length enhancement it introduces. Path length enhancement is the ratio between the short-circuit current generated from a solar cell with and without the rear reflector. In practice, a path length enhancement factor of up to 10 can be achieved [128, 13].

26

(a) Front structures

Planar Si surface — ARC(s) — Si

Macrotextured Si surface — ARC(s) — Si

Nanostructured Si surface — Si

Dielectric nanostructures — Dielectric — Si

Dielectric — Si

(b) Rear structures

Si — Metal — Metal reflector

Si — Metal — Metal reflector with dielectric

Si — Metal — Macrotextured Si surface

Si — Metal — Distributed Bragg grating

Si — Metal — Grating
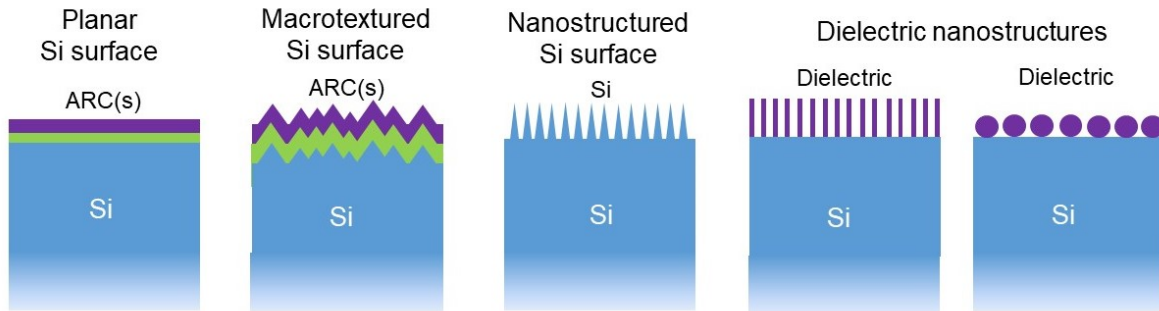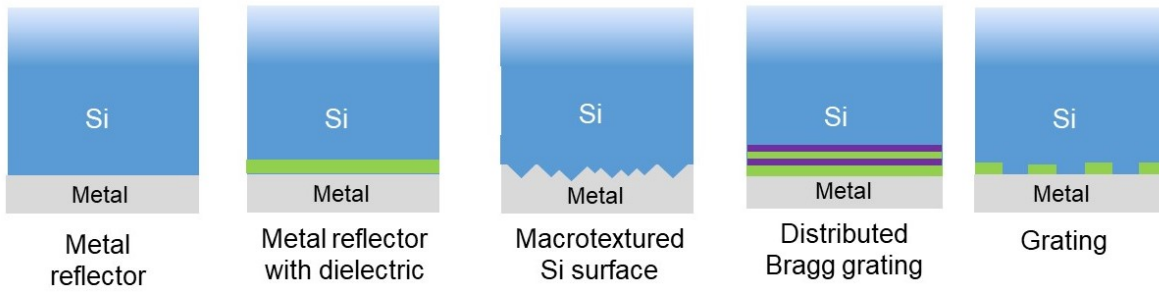
Figure 2.10:   Simplified picture of different photon management structures used in the front and read side of silicon solar cell

Therefore, both the front and rear side light trapping are essential for proper photon management.

Front Side Photon Management Approaches

To enhance the optical transparency of the solar cell, different techniques have been employed on the front side of the cell, including antireflective coating (ARC), surface texturing and incorporating resonators. Some of these structures are illustrated in figure 2.10(a).

Single layer dielectric ARC is a simple technique to mitigate the reflectance losses. Owing to its feasible fabrication process, low price, and added benefit of surface passivation, SiNx ARC is

widely used in commercial solar cells. The refractive index (n) of crystalline silicon at 550-600 nm is approximately 4, hence SiNx (n=2) is widely used as the coating material [159, 163]. However, the optical performance of single layer ARC is wavelength and polarization dependent. Besides, its angular optical response is limited, which is a crucial drawback in practical applications [165]. A double layer (e.g., ZnS+MgF) ARC coating provides further reduction in reflection. However, being too expensive, PV industry does not use this approach.

To extend the spectral and angular responses of ARC to a wider range, various approaches have been studied. Currently these methods can be divided into two categories: patterning on layers with different materials and direct patterning on the silicon wafer (surface texturing). In these architectures, nano or microstructures with gradually varying geometries allow higher transmission. Unlike traditional single layer ARC, these approaches show broadband (and some of them omnidirectional) optical response due to its graded index distribution and thus destructive interference of a wide range of wavelengths, which is necessary for solar cells.

Antireflective nanostructures with different shapes have been studied, including nanowires, nanopillars, nanodomes, nanospheres, nanorods and nanocones. For example, Jeong et al. have studied the performance of an ultra-thin silicon nanocone solar cell [102]. In this study, silicon nanocones are fabricated on top of a silicon substrate which helped achieve more than 80% external quantum efficiency (EQE) from 400-800nm incident wavelengths.

Surface texturing is another method of reducing reflection losses. The major difference between surface texturing and antireflective nanostructure is that surface texturing is directly etched or deposited on the substrate, without adding a new layer with different materials. Therefore, surface texturing has good fabrication simplicity. Similar to antireflective nanostructures, enhanced transmission into the cell is achieved due to altered internal angles and graded refractive index caused by gradually varying geometry. For example, a nanotextured multicrystalline (mc-Si) solar cell

was reported by Kafle et al. [104]. In this study, nanotextures are etched on a 195 um thick p-type mc-Si wafer by dry exothermic plasma etching. Fellmath et al. has reported another Al-BSF c-Si solar cell with pyramid texturing on the front surface [54]. A cost-effective method of achieving nanostructure silicon is called black silicon (b-Si) due to its low reflection, which is another candidate for light trapping. B-Si has a wide absorption spectrum, especially at visible and infrared range, rendering high power conversion efficiency of solar power. Savin et al. reported a b-Si solar cells with interdigitated back contacts (IBC) that mitigates reflection losses on the front side [142]. The b-Si is fabricated by deep reactive ion etching (DRIE). Due to the needle-like silicon textures with high aspect ratio, an effective medium is formed. As a result, most of the reflection loss is eliminated.

An alternative approach of improving the device performance is incorporating optical resonators. When nanoparticles are embedded inside the solar cell, the field distribution is highly confined in the active layer by the excited resonant modes, thus enhancing the absorption of the incident photons [35]. However, additional plasmonic absorptions can be induced by metallic nanoparticles. Various materials have been adopted as nano resonators, including dielectric (Mie resonance) and metallic (plasmon resonance) materials. By applying particles with different sizes, multiple resonant peaks are excited, thus rendering broadband optical response. Besides, these nanoparticles also scatter light, which extends the length of the optical path inside the active region. For example, a broadband spherical nanoshell solar cell has been reported by Yao et al. [170]. In this configuration, a single layer of silicon nanospheres with 50nm thickness is deposited on the 1 um silicon substrate. The incident light is coupled into whispering-gallery modes (WGMs) inside the spheres and transmitted into the substrate. Multiple resonant modes with different resonant peaks are excited, leading to broadband optical absorption.

In industry, a combination of the random pyramid (Si) texturing and SiNx ARC is used most of the time.

Similar to the front side, several rear side photon management techniques have been developed. Most of the shorter wavelength photons already being absorbed in the cell, it is of great interest that these techniques provide high reflectance and scattering around Si band edge; scattering increases path length, providing more chances of absorbing the photons to the cell [132]. Figure 2.10(b) illustrates some of the rear side photon management approaches.

In Al-BSF solar cells [159], an aluminum back reflector is printed on the rear side of the silicon wafer which acts as both a mirror, and a contact for the charge collection. In the PERC cells localized passivation layers are added on the rear side contacts to reduce the recombination loss and increase back-reflection; putting the passivation layer between the silicon and the metal contact reduces the optical absorption loss in the metal occuring through evalescent coupling [93], thus increasing the rear reflectance. [76, 98]. In IBC solar cells, interdigitated metallic contacts are placed on the rear side of the solar cells to eliminate the shadowing loss. These contacts act as back reflectors and enhance the absorption of the incident photons. Surface textures are etched on both sides of the silicon wafer, yielding longer diffusion length of charge carriers. Additionally, a thin film layer of the same material (a-Si) is sandwiched between the silicon wafer and a doped a-Si layer to passivate the interface on the rear side of the cell, improving total quantum efficiency. [153, 172].

Patterned nanostructures are also used for light trapping on the rear side. For example, Zhu et al [177] reported an a-Si:H solar cell with nanocone back reflectors. In addition, the scattering of the incident light is enhanced inside the plane, leading to enhanced optical path and effective absorption.

Various types of gratings on the rear side of the cell have been studied. Compared to planer rear

reflectors, grating structures can support resonant modes within the gratings and better enhance the optical path length by scattering. A hybrid grating-photonic crystal back reflector silicon solar cell has been reported by Zeng et al. [176]. In this design a reflection grating is placed on the rear side of the cell and a 1D distributed back reflector (DBR) layer is deposited under the grating.

Resonating modes boost the light harvesting on the rear side of the solar cell. Tu et al. has reported an application of double wall carbon nanotubes (DWCNTs) in amorphous silicon (a-Si) solar cells [157]. By spin coating the DWCNT solutions on Ti/Ag back contacts, plasmon resonances are excited and the light scattering is enhanced in the range from 589-700 nm.

Solar Cell Electrical Characteristics

The output of a solar cell is electricity. Therefore it is desirable to observe the electrical characteristics of a cell. The following section provides an idea about the electrical characteristics of a cell.

Electrical Model of a Solar Cell

The equivalent circuit model of a solar cell is depicted in figure 2.11. The ideal solar cell consists of a current source (with current density, J), and dark current loss represented as a diode. However, a practical solar cell also has series resistance R_s and shunt resistance R_{sh}. In a practical solar cell, the contact resistivity and sheet resistance of both the front and rear side of the cell contribute to the series resistance. The shunt resistance represents the bulk resistance across the p-n junction. Higher shunt resistance is good for a cell, because it directs most of the photo-currents to the external load. Now, sometimes because of the manufacturing issues like nonuniform doping, or front contact cutting through the junction and touching the base of the cell may create shunts

31
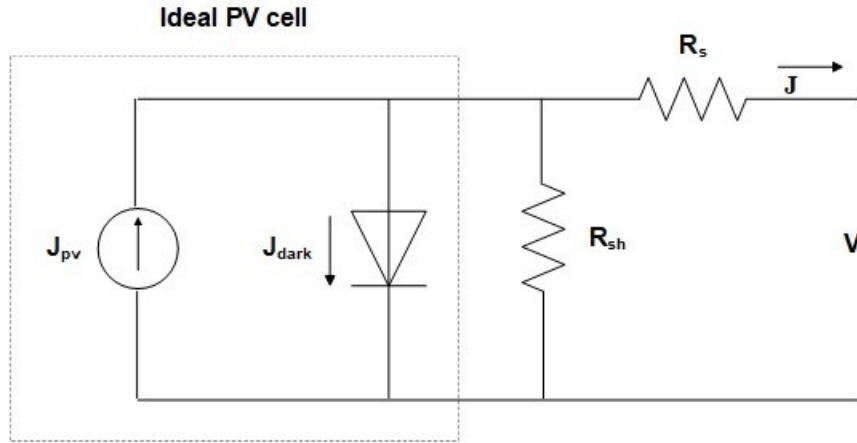
Figure 2.11: Electrical model of a solar cell

[89, 90].

Current-Voltage characteristics

The current-voltage characteristics of a solar cell is illustrated in figure 2.12 and can be described by equation 2.19. There are certain points on the current density (J) vs. voltage (V) curve which are of great interest. First of all, short-circuit current density (J_{sc}), which is the current density when the voltage is 0. In this condition all the photogenerated currents flow to the external circuit. Therefore, J_{sc} is the maximum current density attainable from a cell and equal to the photogenerated current density J_{PV}. Similarly, V_{OC} is the open circuit voltage which is the maximum attainable voltage coming out of the cell.

$$J = J_{PV} - J_0 \left[exp \left(\frac{V + JR_S}{nkT} \right) - 1 \right] - \frac{V + JR_S}{R_{sh}} \tag{2.19}$$

As electrical power is the multiplication of voltage and current, it can be easily understood that

32
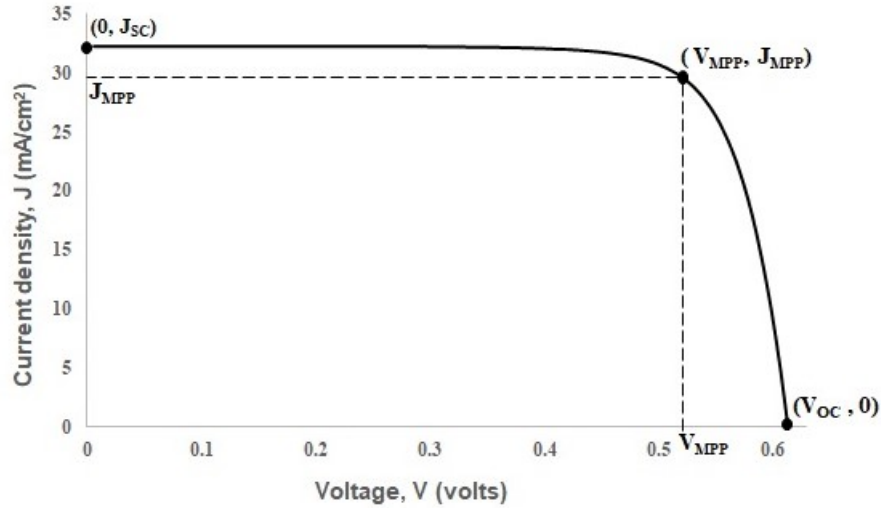
Figure 2.12:   Current-Voltage characteristics of a typical solar cell

the power from a cell depends on the operating point. The operating point at which the maximum amount of power can be extracted from a cell is called the maximum power point (MPP). Figure 2.12 marks the voltage and currents at MPP condition. We notice that V_{MPP} and J_{MPP} are lower than V_{OC} and J_{SC} respective.

Fill factor (FF) is an important parameter in solar cell performance analysis, which can be expressed as,

$$FF = \frac{V_{MPP} \, J_{MPP}}{V_{OC} \, J_{SC}}$$

(2.20)

Now, the most important parameter of a solar cell is the efficiency (η), which can be obtained from the J-V curve using the following equation,

$$\eta = \frac{V_{MPP} \, J_{MPP}}{P_{in}} = \frac{V_{OC} \, J_{SC} \, FF}{P_{in}}$$

(2.21)

Here, P_{in} is the total incident power (optical) on a cell. Customarily, efficiency is calculated for

33

1000 W/m^2 illumination.

CHAPTER 3: SOLAR CELL MANUFACTURING PROCESS AND PERFORMANCE ISSUES RELATED TO IT

In the way to improving solar cell performance, it is crucial to understand the manufacturing process and the common issues arising from the imperfections in the manufacturing line.

Solar Cell Manufacturing Process

In principle solar cell is just a simple p-n junction made of semiconductor material. However, in reality it's much more than that. Manufacturing solar cells require deep knowledge of material science, electrical and mechanical engineering. The manufacturing process consists of several steps from wafer to the finished cells. These steps [167, 27] are discussed in the following subsections.

Wafer

Solar cell manufacturing starts with wafers. These wafers are sliced from silicon ingots and can be either monocrystalline or multicrystalline. Multicrystalline wafers have wide range of spatial variations, defects, grain boundaries etc. which deteriorate their performance. Level of impurities is also higher in multicrystalline wafers. However, they are cheaper than their monocrystalline counterparts. The majority of the monocrystalline ingots for Si PV are produced using Czochralsky (Cz) process. Cz method depends on the crystal growth of molten silicon following the crystal structure of the seed crystal. Solidification process is widely used to make multicrystalline ingots. Directional solidification from melt is one type of solidification method where a moving temperature gradient is used for the crystallization. The solid-liquid planar interface in this process helps avoid micro-segregation. Another type of solidification is block casting, where molten silicon is al-
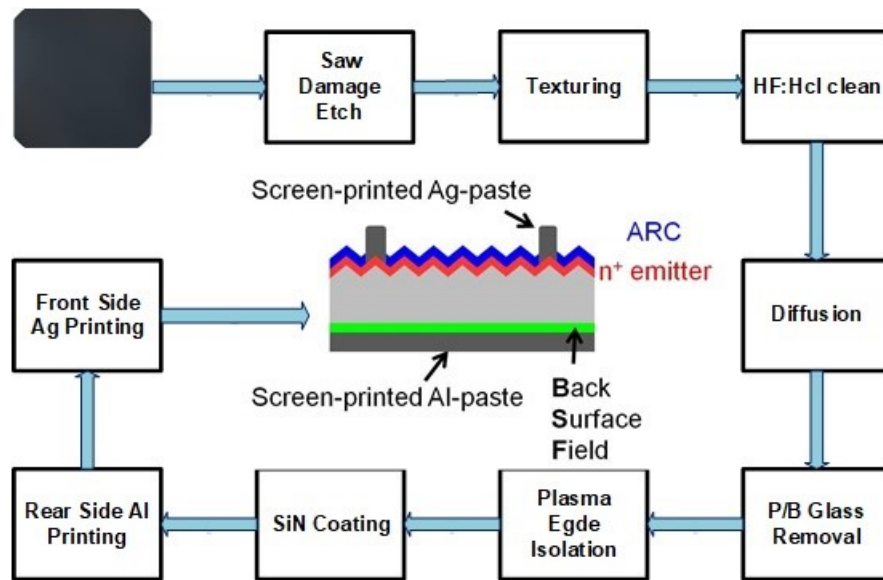
Figure 3.1: Pictorial diagram of the steps in a typical solar cell manufacturing process

lowed to cool in a crucible and form ingots with rectangular cross section, often called as 'brick's. Extreme care must be taken to minimize the impact of iron diffusion from the cast to the brick and to minimize stress at the grain boundaries, which can results in significant recombination. A typical thickness of the wafers used to make a Si PV cell is 200 μm.

Saw Damage Etch

Wafers are made by slicing semiconductor ingots by wire saws. The sawing process leaves marks, nonuniformity and contaminants on the surface of the wafer, which can act as a recombination centers in the finished solar cell. To eliminate these, the wafer is planarized by saw damage etch process. The process is dictated by NaOH concentration, temperature, etch time and rinse time.

Texturing

A flat surface can reflect more light than a rough surface. To achieve better light trapping, the surface of the solar cell is textured using chemical process. Proper use of NaOH and isopropanol provides pyramidal structures on the wafer surface. The height and coverage of the pyramids are dictated by the concentration of the chemicals, exhaust flow, temperature and etch time.

HF:HCl clean

Before sending the wafer to the diffusion furnace, it is essential to clean it very well and eliminate all the impurities. The texturing process can lead to residues of silicates. Some metal impurities can also be diffuse into the native oxide on the wafer surface. These are cleaned using HF and HCl. First the wafer is immersed at 1-5% HF solution. After rinsing with DI water, it is again immersed into 2% HCl solution. Then it is rinsed with DI water.

Diffusion

Diffusion process is required to form emitter and the p-n junction. For a p-type wafer, the emitter is n-type and vice versa. For n-type emitter, phosphorus doping is required and boron doping is required for p-type emitter. The diffusion is usually done inside tube furnaces. The factors dictating diffusion process are dopant concentration, nitrogen flow, and temperature.

Phosphorus/Boron Glass Removal

During the phosphorus diffusion process, there forms a substance on the wafer called phosphosilicate glass (PSG) which supplies the phosphorus dopants. It contains metal traces which is useful

for gettering. However, once the diffusion is done, PSG has to be removed. HF can remove PSG. The process is dictated by HF concentration, etch time and rinse time.

Edge Isolation

During the diffusion process, it also acts on the rear side and the edges. The doped portion of the edges has to be etched to keep the front and the rear side isolated, otherwise it will act as a shunt path. It is done by RF plasma etching. Edge isolation can also be done using chemical process or laser scribing. With the cell being thinner, it is being more desirable these days that the edge isolation is done through a non-contact method like laser scribing; such a method reduces the risk of crack formation on the cell.

Silicon Nitride Coating

Silicon nitride (SiN_X) acts as an antireflection coating (ARC) in the solar cell. In addition to its excellent anti-reflection characteristics, hydrogenated SiN_X (SiN_X:H) also provides surface passivation. SiN is coated onto the front surface of the wafer by plasma deposition method, which deposits on one side only. The deposition process is dictated by silane flow, ammonia flow, temperature and time. The typical thickness of SiN layer is in the order of tens of a nanometer.

Rear and Front Side Screen Printing

The front and the rear contacts are required for the collection of photogenerated carriers, electrons and holes. Usually full area Al is used for the rear contact. For the front side, Ag of about 5% area coverage is usually used for the front contact. The standard process for the rear side contact formation is screen printing. For the front side, a wide variety of methods are used. These methods
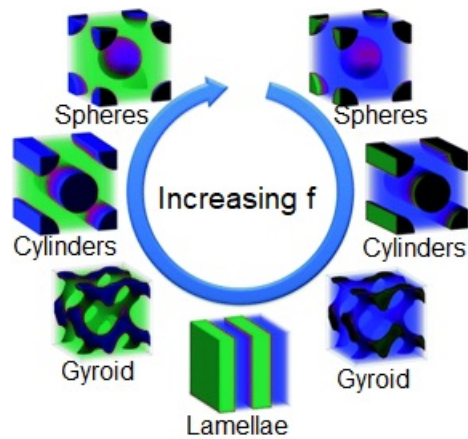
Figure 3.2: Formation of different block-copolymer self-assembled nanostructures. Here f is the volume fraction of one polymer block [31]

includes a combination of lithography and evaporation, sputtering of the seed metal layer and then plating, laser grooving of the Si and then contact formation through plating etc. [43]. Sometimes, Ni and Cu plating is also used as rear side contacts [108].

Block Co-Polymer Self Assembly Method of nanostructure Fabrication

In this work, multifunctional nanostructures are fabricated that can perform photon management on the rear side of the cell, provide surface passivation and helps lateral charge transport. These structures are fabricated using a bottom-up fabrication method called block co-polymer (BCP) self assembly.The self assembly process leverages the physical forces to make certain patterns. It is different than the lithography based top down fabrication approach.

The BCP self assembly [116, 122] method of nanofabrication was developed taking inspiration from the nature; nature builds important biological systems by harnessing the chemical forces. The most simple form of BCP is the diblock co-polymer, having two chemically distinct polymer blocks A and B that are covalently bonded together. One of these blocks is usually hydrophilic, and the other one hydrophobic. When such a BCP solution receives energy from external source (e.g. kinetic energy from spin coating or thermal energy from annealing), the chain of the polymer blocks mobilizes and it takes a distinct periodic form. Based on the volume fraction of the blocks and the processing conditions (e.g. temperature, atmospheric pressure) the BCP self assembly process can provide polymer structures like sphere, cylinders, gyroid, lamellae as illustrated in figure 3.2. In this figure, the two blocks are illustrated as blue and green color. It is also possible to obtain the inverse structures e.g., inverse-cylinders by changing the volume fraction of a block. Triblock co-polymers (having polymer block A, B and C) can also be used for more complex structures.

The degree of the BCP self-assembly process depends on three factors [34] (i) Segregation strength, typically expressed by Flory-Huggins interaction parameters (χ_{AB} for diblock co-plymer; χ_{AB}, χ_{BC} and χ_{CA} for triblock co-polymer). The segregation strength must exceed a certain threshold to occur the self-assembly and it is composition dependent. If it is below the threshold, the material forms a disordered morphology (ii) degree of polymerization, N (iii) volume fraction (f_A and f_B of the blocks A and B respectively such that $f_A + f_B = 1$). The shape of the structure heavily depends on the volume fraction as illustrated in figure 3.2. For a diblock co-polymer, the Flory-Huggins interaction parameter can be expressed as,

$$\chi_{AB} = \frac{z}{kT} \left[\varepsilon_{AB} - \frac{1}{2} \left(\varepsilon_{AA} + \varepsilon_{BB} \right) \right] \tag{3.1}$$

Here k is the Boltzmann constant, T is the temperature and z is the number of nearest neighbours in each repeat unit of the polymer. Also, ε_{AA}, ε_{AB} and ε_{BB} are the A-A, A-B and B-B interaction energies per repeat unit.

It worths mentioning here that the self-assembled structures have a pitch in the order of 30-40 nm. Research is being conducted to increase the pitch using directed self assembly [63], with the help of traditional lithography process. This method can provide a pitch of 100-300 nm pitch.

Fabrication of Al$_2$O$_3$ Nanostructures using Block Co-Polymer Self Assembly

The BCP structures can be used to form Al$_2$O$_3$ nanostructures. The fabrication steps are illustrated in figure 3.3. In this method, first the BCP structures are formed on the substrate by spin coating at certain speed and annealing at certain temperature. Once these polymer nanostructures are formed, the next step is to synthesize the Al$_2$O$_3$ nanostructures by vapor phase infiltration approach. In this process, vapor phase infiltration is performed using certain cycles of exposure to trimethylaluminum and water vapor in a commercial atomic layer deposition tool. Because of the chemical selectivity of Al$_2$O$_3$ deposition it is deposited almost exclusively within block A in the figure. After infiltration, the polymer template is removed by O$_2$ plasma ashing to reveal alumina replicas of the self-assembled A block structure (step 3).

Solar Cell Performance Issues Related to Manufacturing Imperfections

Crystalline defects and Dislocation Centers

These defects occur due to the imperfections in the growth process of the semiconductor ingot, out of which wafers are made.The defects and dislocation centers act as the recombination centers.
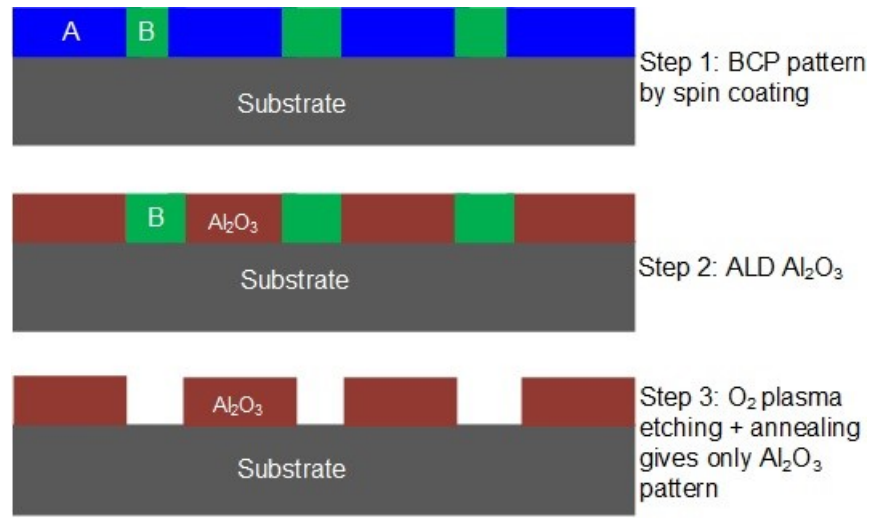
Figure 3.3: Fabrication of block-copolymer self-assembled Al_2O_3 nanostructures

These defects occur more in the multicrystalline wafers than the monocrystalline wafers. The recent record high efficiency cells are made of monocrystalline wafers which allowed them to avoid some of these losses.

Saw Marks

The imperfections in the saw damage removal from the wafer surface leave saw marks on the wafer which causes reliability issue in the cells. This saw marks often lead to micro cracks. Sometimes the crystal defect due to these saw mark promotes formation of blisters. It is also found that these saw marks can cause pill off of the SiN anti-reflection coating.

Issues Related to Edge Isolation

Edge isolation is usually done using laser scribing. At the time of edge isolation, the high temperature arising from the laser material interaction causes the silicon to melt down. The melting can cause an undesired effect called emitter drive-in, which allows P-atoms to go underneath the isolation groove. Also the melting of the material and the ablation and re-deposition of the materials along the perimeter (a distance in mm range) of the cell causes reduction of the active region of the cell.

High Surface Recombination

If both the surfaces or even just one surface of the cells are not passivated well, surface recombination occurs and it affects the cell current density, voltage and fill-factor. Due to manufacturing variability, sometimes certain region on the cells may be left unpassivated which affects cell performance.

High Auger recombination

Auger recombination is related to the excessive doping. Doping helps junction formation and separation of the photogenerated carriers. However, excessive emitter doping causes Auger recombination in the cell which reduces cell efficiency.

High resistivity

If the metal contacts does not form good contact with the semiconductor, it causes high contact resistivity. It is also very important to make sure that the contacts formed are Ohmic contacts.

Sometimes the thin gridlines in the front side break. Since current cannot pass through them, it increases the series resistance of the cell.

Shunts

Shunts are any regions on the solar cells with very small resistance across the p-n junction. Sometimes they are formed on the cell due to manufacturing imperfections. The presence of the shunt decreases the short circuit current density of the cell severally. Shunts can be of three types [37] : (a) linear shunts (b) non-linear shunts (c) junction pre-breakdown. Linear shunts are those which demonstrates Ohomic characteristics when a voltage is applied across them. It is more deadlier in terms of the cell performance than the other two. It can occur due to poor junction isolation, local non-homogeneities and cracks in the wafer prior to the emitter formation through diffusion, and presence of materials like SiC (i.e., material induced shunt). The nonlinear shunts are those that exhibit diode like nonlinear behavior. These shunts could be process induced or are related to the wafer quality. If there are scratches on the wafer before or after the diffusion process, the front metalization can cut through the emitter layer, touches the base and forms a Schottky diode. Local non-uniformity of the p-doing or presence of defects may also give rise to non-linear shunts. Junction pre-breakdown is the phenomenon in which the p-n junction breaks down at a lower reverse voltage than the usual value (i.e. -50V). Local contamination site on the Al surface prior to p-diffusion, presence of recombination active defects, texturing issues or bulk defects can lead to the shunts.

Microcrack Formation

Microcracks can form in the cell both at the time of handling of the wafers/cells and operation in the field. The environmental factors like bitter cold, violent wind, heavy snow, hail, and baking

sun can cause mechanical or chemical stress on the cell, leading to microcrack formation. The thermal cycle a cell goes through everyday expands, contracts, and flexes the metals contacts and interconnects leading to mechanical stress on the Si part. In addition to these reasons, cell bowing also can contribute to these kind of microcrack formation. It occurs due to the difference in thermal expansion coefficient between silicon and the metal contact and can occur at the time of contact firing or even at the time of operation.

CHAPTER 4: MEASUREMENT OF OPTICAL, RECOMBINATION AND RESISTIVE LOSSES IN SILICON PHOTOVOLTAICS

Measurement plays vital role in the efforts to improving cell performance and developing cost-effective manufacturing processes. Therefore it is important to become familiar with different metrology methods, their working principle, and limitations. Being an optoelectronic device, the characteristics of a solar cell depends on the cell optics, presence of various loss mechanisms, carrier transport properties etc. Therefore, measurement of a solar cell ranges from material characterization to performance testing.

The tradition method of measurement techniques mainly expresses the cell characteristics by the global parameters. A better approach is to provide the spatial distribution of the parameters. Both of these methods are introduced in the following sections.

Current-Voltage Measurement

Current-voltage (I-V) measurement is the most basic method of evaluating cell performances that provides the first-hand account of the cell performance issues. The outcome of this measurement is the I-V curve which is directly related to the cell efficiency. Figure 4.1 presents a solar simulator that can be used for I-V measurement.

The I-V characteristics of a cell is expressed by equation 4.1. Here, V_T is the thermal voltage, I_{PV} is the photogenerated current density, R_S is the series resistance and R_{sh} is the shunt resistance.

$$I = I_{PV} - I_0 \left[exp\left(\frac{V + IR_S}{V_T} \right) - 1 \right] - \frac{V + IR_S}{R_{sh}} \tag{4.1}$$

46
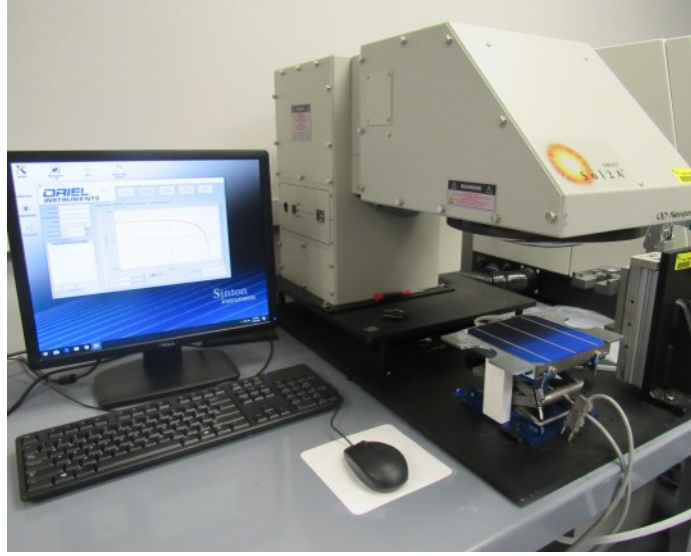
Figure 4.1: Solar simulator used for current-voltage measurement

Now, I_{pv} and I_0 are cell parameters that do not change with voltage. Taking derivative of equation 4.1 with respect to voltage and setting $\frac{dI_{pv}}{dV} = 0$ and $\frac{dI_0}{dV} = 0$, we get,

$$\frac{dI}{dV} = -\frac{I_0}{V_T} \left[exp\left(\frac{V + IR_S}{V_T}\right) \left(1 + R_S\frac{dI}{dV}\right) \right] - \frac{1}{R_{sh}} - \frac{R_S}{R_{sh}}\frac{dI}{dV} \tag{4.2}$$

Rearranging this equation we get,

$$\frac{dI}{dV}\left[1 + \frac{R_S}{R_{sh}} + \frac{I_0 R_S}{V_T}exp\left(\frac{V + IR_S}{V_T}\right)\right] = -\frac{I_0}{V_T}exp\left(\frac{V + IR_S}{V_T}\right) - \frac{1}{R_{sh}} \tag{4.3}$$

This relationship is valid for all the points on the I-V curve. Now, let us consider some special circumstances. In the short-circuit condition, $V = 0$, $I = I_{SC}$. Also, $I_{SC}R_S \leq V_T$ and I_0 is a small quantity. Therefore, we have,

$$I_0 exp\left(\frac{V + IR_S}{V_T}\right) = I_0 exp\left(\frac{I_{SC}R_S}{V_T}\right) \approx 0 \tag{4.4}$$

47

Now, R_S is much smaller than R_{sh}. Therefore, $\frac{R_S}{R_{sh}} \approx 0$. Applying this and equation 4.4 to equation 4.3, we obtain,

$$\frac{dI}{dV}\bigg|_{at\ V=0} = -\frac{1}{R_{sh}} \tag{4.5}$$

Rearranging we get,

$$R_{sh} = -\frac{dV}{dI}\bigg|_{at\ V=0} \tag{4.6}$$

This equation shows that the slope of the I-V curve at $V = 0$ is related to the shunt resistance, R_{sh}. Similarly, we can also consider another condition when $I = 0$ and $V = V_{OC}$ (i.e. open-circuit condition). In this condition, there is no current flowing to the external circuitry and the entire short-circuit current (which is equal to the photogenerated current) flows through the diode. We have,

$$I_0 exp\left(\frac{V + IR_S}{V_T}\right) = I_0 exp\left(\frac{V_{OC}}{V_T}\right) \approx I_{SC} \tag{4.7}$$

Applying this relationship to equation 4.3, we obtain,

$$\frac{dI}{dV}\left[1 + R_S\left(\frac{1}{R_{sh}} + \frac{I_{SC}}{V_T}\right)\right] = -\left(\frac{I_{SC}}{V_T} + \frac{1}{R_{sh}}\right) \tag{4.8}$$

Rearranging we get,

$$R_S\left(\frac{1}{R_{sh}} + \frac{I_{SC}}{V_T}\right) = -\frac{dV}{dI}\left(\frac{I_{SC}}{V_T} + \frac{1}{R_{sh}}\right) - 1 \tag{4.9}$$

$$R_S = -\frac{dV}{dI} - \frac{1}{\frac{1}{R_{sh}} + \frac{I_{SC}}{V_T}} \tag{4.10}$$

Now, R_{sh} is a big quantity and $\frac{1}{R_{sh}} << \frac{I_{SC}}{V_T}$. Therefore, we can have further simplification of the expression of the series resistance.

$$R_S = -\frac{dV}{dI}\bigg|_{at\ V=V_{OC}} - \frac{V_T}{I_{SC}} \tag{4.11}$$

This equation shows that the slope of the I-V curve at $V = V_{OC}$ is related to the series resistance.

48

The measured I-V curve provides important insights about different performances issues. Some abnormality of the I-V curve and their cause are discussed in the following subsections:

Lower Current Was Measured Than Expected

A cell or module may produce less current if it is degraded or soiled (meaning, covered with dusts), especially uniformly. Less current can also be measured if the irradiance sensor is oriented incorrectly, irradiance sensor calibration was wrong, irradiance was too low or the number of the solar cells in parallel orientation was not entered correctly in the model.

The Slope of the I-V Curve Near Jsc Is Not Normal

The slope of the I-V curve can become steeper than expected. This points to low shunt resistance of the cell that eventually reduces the fill factor and the efficiency. The potential reason of steeper slope are: existence of shunt path(s) in a cell, existence of shunt path(s) in the cell interconnects, mismatch of Isc among different cells on a module.

The Slope of the I-V Curve Near Voc Is Not Normal

The increase in the series resistance can reduce the steepness of the slope of the I-V curve between the Vmpp and Voc. It reduces the fill factor and efficiency, as a result. The potential causes behind the reduction of this steepness are: excess resistance of the PV wiring, increased series resistance of the module, or increased resistance of the interconnections.

Notches or steps can be seen in the I-V curve of a module. It indicates that there are mismatch of the current and voltage produced by the different regions on the module. The potential causes of these notches are partial shading, damaged PV cells on a module or short-circuit of the bypass diode.

Reflectance Measurement

Cell optics is an important factor in determining the amount of current produced. If the front side of the cell is reflective, light cannot go into the cell hence photogenerated current density reduces.Photon management mechanisms [35] are usually employed to reduce the front reflection. To assess the quality of such a photon management approach, one has to conduct the reflectance measurement. Figure 4.2 illustrates the reflectance curve of a typical silicon solar cell. Reflectance occurs from both the front and rear side of the cell. The rear side reflectance, also called as the escape reflectance is the percentage of light that enters into the cell, reaches the rear side of the cell not being absorbed in the active region, reflects back towards the front side of the cell and finally escapes from the cell. Escape reflectance occurs mostly in the long wavelength regions.

The reflectance in the figure 4.2 is the total reflectance comprising of the front and the escape reflectance. We notice that the total reflectance (solid line) is higher in the shorter wavelength. Then, it drops drastically until it starts increasing gradually. At longer wavelength around 1000 nm, the total reflectance starts increasing drastically again. The reason for this drastic increase is the escape reflectance. Thus, if a trend-line is drawn from 800 nm to 900 nm and extended beyond 1000 nm wavelength, that will be the front reflection beyond 1000 nm wavelength (shown as dotted line in the figure). Subtracting the front reflectance from the total reflectance gives the
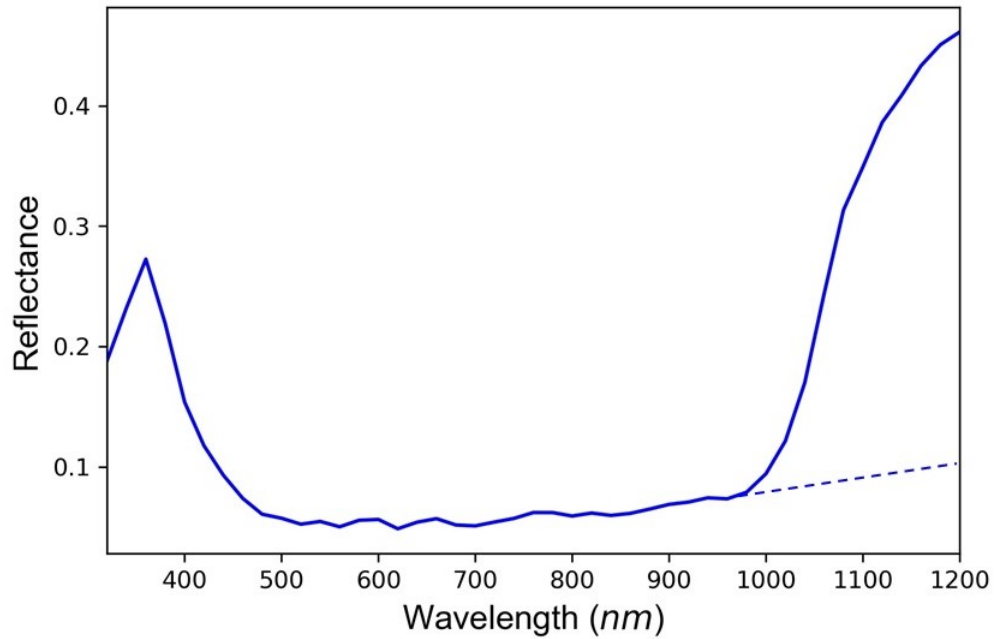
Figure 4.2: A typical reflectance curve of a silicon solar cell

escape reflectance.

$$t = \frac{\lambda_{min}}{4n} \tag{4.12}$$

Important insights about the quality of the anti-reflection coating (ARC) can be obtained from the reflectance spectrum. The ARC is nothing but the a thin film. Therefore, the wavelength of the minimum reflectance can be used to calculate the ARC thickness using equation 4.13. Here, n is the refractive index of the material used as ARC (usually, SiNx).

Suns-Voc and Lifetime Testing

Predicting the open circuit voltage (V_{OC}) of a cell at the early stages of the fabrication process is valuable for reducing the manufacturing cost. The Suns-V_{OC} measurement is a Quasi-steady-state photoconductance (QSSPC) measurement [33] that can be used to estimate the V_{OC} of a cell. As this is not the real V_{OC}, rather estimated one, it is called the implied V_{OC} (or iV_{OC} in short). For a p-type wafer, we can utilize the relations hip between the carrier concentration and voltage to estimate iV_{OC} as following,

$$iV_{OC} = \left(\frac{kT}{q}\right) ln\left(\frac{\Delta n(0) \times [N_A + \Delta n(0)]}{n_i^2}\right)$$ (4.13)

Here, T is the temperature in Kelvin, k is the Boltzmann constant, q is the charge of an electron, n_i is the intrinsic carrier concentration of Si, $\Delta n(0)$ is the carrier concentration at the junction and N_A is the doping density of the substrate. Usually iV_{OC} is greater than the real V_{OC}, as iV_{OC} does not account for the recombination occurring in the metal-silicon interface.

Lifetime measurement is another very important characterization method to assess the quality of a wafer and cell. A common approach to measure the lifetime of a sample (as also in a Sinton Instrument), is to use the Eddy-current method. In this method, a coil is placed underneath the sample stage. After the sample (let's say, a wafer) is placed on the stage, it is illuminated with pulsed light. Because of the photogenerated excess carrier conductance of the sample changes, and the change is detected by the coil. The lifetime of the sample is then calculated using transient photoconductance and Quasi-steady-state photoconductance methods.

Spatial distribution of the parameters

The traditional characterization methods like I-V, Suns-VOC measurements etc. express the solar cell performance by global parameters. However, a solar cell is a large area device having spatial variation over its surface. These variations may arise because of numerous reasons. The presence of faults like cracks or scratches, shunts, break in the busbars or gridlines, recombination centers like crystalline defects or dislocation centers and delamination or degradation- all these may cause performance variation in a cell. It is therefore very important to take a close look at the spatial distribution of a particular parameter over the cell. The spatially resolved characterizations (or, imaging in other words) are very useful in numerous ways: First, it helps get a better understanding of the loss mechanisms and their root causes [89, 90]. Thus they work as a guideline for designing experiments as an effort to increase the efficiency. Secondly, process variations negatively impact the overall device performance and hence needs to be addressed (Hossain 2018, Hossain 2019). These process variations clearly appear in the parameter images. Therefore, the spatially resolved characterizations suggest ways to reduce these variations. In fact, a study shows that utilization of these spatially resolved characterization methods may reduce the PV production cost at a great degree.

All the spatially resolved characterization methods discussed in this review are non-destructive in nature. However, these are active imaging techniques, meaning they require an excitation source to provide a response. The excitation energy can be either electricity (current or voltage), light, or heat. Some of them are used inline, the others cannot be used inline. However, all these metrology techniques provide useful information about the performance metrics of the solar cell and module.

53

Luminescence Based Imaging

Luminescence occurs when an electron in the conduction band makes a downward transition to the valence band and loses its energy in the form of light. Such a transition usually provides one photon, the wavelength of which depends on the difference between initial and final energy of that electron. An excitation source is required which sends the electron up to an initial position in the conduction band. When that electron comes back to the valence band (final position), it radiates light in the form of luminescence. The probability of the luminescence depends on a couple of important factors: temperature, intensity and frequency of the excitation source and quality of the material. If crystalline defects, dislocation centers, trap states, cracks or other forms of imperfections are present, some of the energy is also lost through non-radiative losses. Therefore, for a uniform incident light intensity, there are clear differences between the luminescence output from the good and bad regions on PV cells and modules. Finding physical defects and inline quality control is one of the main purposes of doing luminescence imaging. Some of them are used for initial inspections of wafers before making cells. However, taking images at different input conditions may provide advanced level performance metrics; e.g. spatial distribution of open-circuit voltage, short circuit current density, minority carrier lifetime, series resistance, efficiency etc. Luminescence based imaging can be classified into three categories: photoluminescence, electroluminescence, and biased photoluminescence imaging, based on their way of excitation. Be it of any type, the luminescence signal is captured by a camera which usually integrates over a broad range of wavelengths. So the resulting image is usually a single-channel grayscale image.

Photoluminescence Imaging

As the name implies, the excitation source for photoluminescence (PL) is light. Usually, laser light of sufficiently high photon energy is used to illuminate the sample. PL imaging is widely used

in industry [144]. When the photogenerated carriers radiatively recombine with their opposite counterparts, the spontaneously emitted energy appears as luminescence light. 808 nm laser is a typical example of the excitation source used in PL imaging of Si solar cells and modules. In such an arrangement, the PL signal is usually captured by CCD camera after passing through a 920 nm long-pass filter (Hossain 2019a). Regions with cell cracks, crystalline defects and dislocation centers look dark in PL images. The images at different conditions may give parameter images like V_{OC} image.

Voltage distribution on a finished solar cell can be calculated based on the correlation between luminescence intensity and local voltage. If the luminescence intensity is ϕ_{xy} at a position (x,y), then the local voltage on the same position is V_{xy} can be expressed as following,

$$V_{xy} = V_T ln \left(\frac{\phi_{xy} - B_{xy}L}{C_{xy}} \right) \tag{4.14}$$

Here V_T is the thermal voltage and C_{xy} is a calibration constant independent of electrical bias and illumination condition. Bxy is the background luminescence signal occurring due to the diffusion-limited carrier recombination [103, 5] and can be determined from the measurements at short circuit condition:

$$B_{xy} = \frac{\phi_{xy-SC}}{I_{L-SC}} \tag{4.15}$$

Here ϕ_{xy-SC} and I_{L-SC} are the photon flux and illumination intensity at short-circuit conditions. The calibration constant is calculated from open circuit PL image ϕ_{xy-low} captured at low illumination condition. The key assumption is, at sufficiently low illumination conditions, the lateral gradient of voltage distribution is negligible. The calibration constant C_{xy} is calculated from the

following expression:

$$C_{xy} = \left(\phi_{xy-low} - B_{xy-low} \right) exp \left[-\frac{V_{OC-low}}{V_T} \right] \tag{4.16}$$

Electroluminescence Imaging

Electroluminescence imaging is also a non destructive measurement method similar to PL. Electroluminescence (EL) occurs when electricity is applied to a solar cell and it acts like an LED [62]. As silicon is an indirect band gap semiconductor, the amount of radiative recombination is smaller than the non-radiative recombination. However, this small radiative recombination is sufficient for the detector (i.e., camera) to be detected. One notable difference between EL and PL imaging is, in EL imaging contacts have to be placed on the cell to drive current through it, which is not the case for PL imaging. Therefore, EL imaging us usually carried out on the finished cells and modules.

Current is used as a excitation source in the electroluminescence imaging. When current is applied to the cell through the metal contacts (basbars and gridlines), the lateral resistance due to the resistance of the contacts and cracks and defects on the cell affect the spreading of the current. If a crack is present, current cannot spread properly near the crack region. This impacts the luminescence coming out of that region. This is used to calculate the series resistance of the cell. Example of series resistance imaging based on this method can be found in these literatures: [81, 78, 97]. The total amount of EL emission depends on both the radiative recombination and the resistance.

Ohmic shunts can be also detected using EL imaging if they are somewhat strong [23]. EL imaging is relatively fast and takes about 1s to finish. It is very suitable for PV module imaging [119].
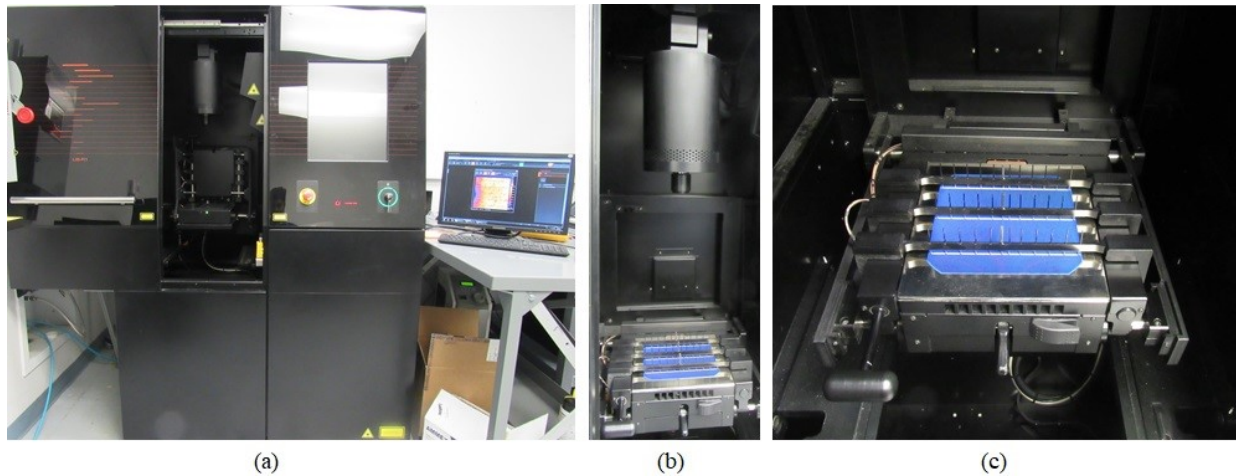
Figure 4.3: An instrument that can be used for PL, EL or biased PL imaging of silicon solar cell. (a) the whole instrument (b) zoomed-in view of the laser light source that is used in case of PL and biased PL imaging (c) zoomed in view of the chuck on which the solar cell is placed for imaging

Biased Photoluminescence

The biased photoluminescence is the combination of photoluminescence and electroluminescence imaging. Here, both light and electricity are used as an excitation source. The biased photoluminescence allows the control of the photogenerated carrier generation and/or recombination by the easily tunable electricity source. Applying different conditions on the measurement, biased PL can determine the spatial distribution of the series resistance, dark saturation current density, and open circuit voltage.

Unfortunately, biased PL is not suitable for the imaging of the PV module.

Thermography Based Imaging

This method is based on the emission of thermal radiation from the sample when it is heated up. The sample is heated up usually by the application of the current. It is an established technique to detect and quantify all kinds of shunts [21]. When current is driven to the sample, the shunt draws a big amount of the current. As a result it heats up more than its surrounding regions and thermal radiation from it is more. This is how the presence of a shunt is usually detected. The resolution of lock in thermography image is limited by the thermal diffusion length, Λ.

$$\Lambda = \sqrt{\frac{2\lambda}{2\pi f_{lock-in}\rho C_p}} \qquad (4.17)$$

where λ is the heat conductivity, ρ the mass density density, C_p the specific heat capacitance and flock-in the lock-in frequency.

Quantum Efficiency Imaging

Quantum efficiency (QE) is an wavelength dependent parameter which is very important in determining the cell performance. The J_{SC} of a cell can be calculated from it's QE characteristics. The external quantum efficiency (EQE) is the ration between the number of electron-hole pairs generated to the number of photons incident on the cell. The internal quantum efficiency (IQE) on the contrary is the ratio between the number of electron-hole pairs generated to the number of photons entering the cell.

If the EQE is measured at each of the points on a cell, that gives an image of EQE. That is exactly what the instrument in figure 4.4 does. It uses 40 LEDs that emit light of center wavelengths in the range 365 nm - 1280 nm. The light from the LEDs is collected by an integrated sphere that illumi-
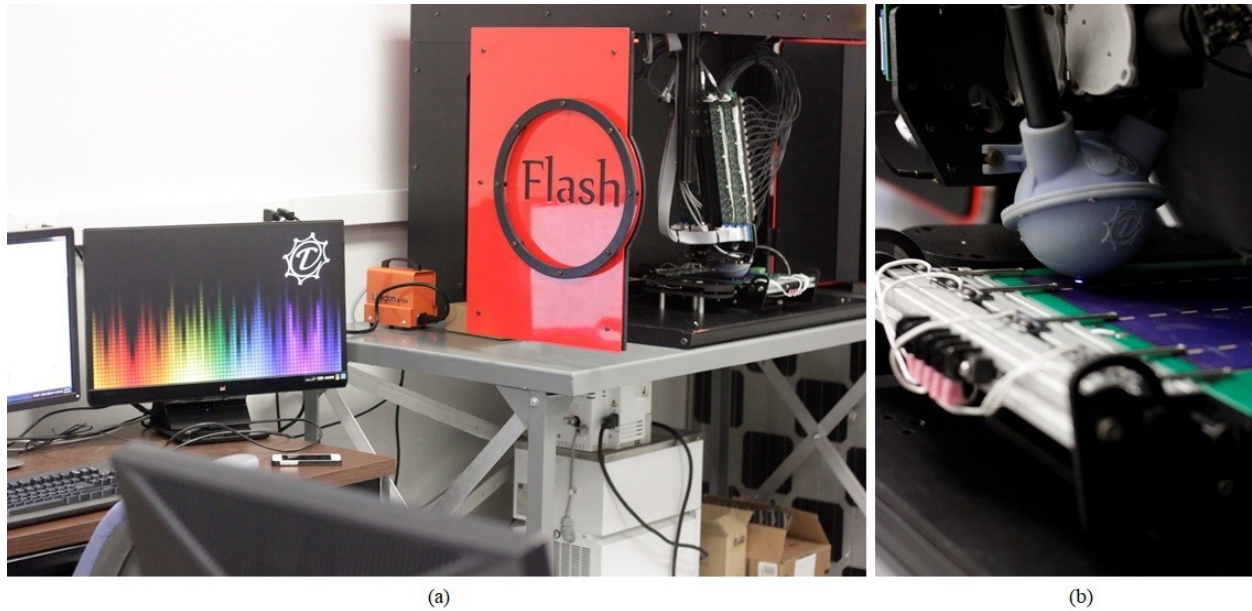
Figure 4.4: An instrument that can be used for quantum efficiency and reflectance imaging (a) the whole instrument (b) zoomed-in view of the light source with integrating sphere

nate a small spot on the sample. The LEDs turn ON and OFF at distinct frequencies. Therefore, when the total photocurrent generated is collected, Fourier transform is applied to it. Correlating the result with the ON-OFF frequency of the LEDs provides their individual contribution. The EQE is then calculated from it.

The tool is also capable of measuring the reflectance of the sample at a spot. Therefore, from EQE and the reflectance, it can later calculate the IQE.

In the measurement process, the EQE and reflectance are measured on each point on the sample, one by one. Combining all these gives an image of these parameters.

Comparison of Different Imaging Techniques

Table 4.1 summarises the key points of different spatially resolved characterization methods.

Table 4.1: Scope of Different Spatially Resolved Characterization Methods

Characterization Method(s)	Sample Type	Outcome	Limitation
Photoluminescence imaging	As cut wafer	Presence of cracks	No R_S map
	As cut wafer finished	Presence of crystalline defects	
	Solar cell or module	V_{OC} map	
	Finished solar cell		
Photoluminescence imaging + conductance coil	Passivated wafer	Lifetime map	No R_S map
Electroluminescence imaging	Finished solar cell, module	Broken gridlines	Separating R_S from J_0 is difficult
Biased photoluminescence	Finished solar cell	R_S map	Not suitable for modules

CHAPTER 5: LOSS MEASUREMENT: INCORPORATION OF SPATIALLY RESOLVED QUANTUM EFFICIENCY MEASUREMENT WITH LUMINESCENCE FOR ADVANCED PARAMETER IMAGING OF SOLAR CELLS

Abstract

The spatial distribution of device performance parameters of solar cells provides important insight into their operation, including the type and magnitude of conversion losses and potential areas of improvement. In most of the procedures used to create these parameter images, a uniform (i.e., global) short-circuit current density (J_{SC}) is usually assumed. However, J_{SC} is known to vary over the surface of a solar cell, especially in polycrystalline absorber materials like multicrystalline silicon. In this work, a high speed quantum efficiency measurement rastered over the surface of a solar cell is used to obtain images of J_{SC}. These J_{SC} images are then used to calculate images of series resistance, dark saturation current density, fill factor, and conversion efficiency. Comparisons are made between the images created with a global J_{SC} and with the spatially-resolved J_{SC}. Negligible variation is observed in the series resistance and dark saturation current density images, but a drastic change is observed in the efficiency images between these two methods.

Introduction

Traditional solar cell characterization techniques like illuminated current-voltage (I-V, J-V) and Suns-V_{OC} provide a single value (i.e., global) for the performance parameters of a solar cell, like the conversion efficiency (), short-circuit current density (J_{SC}), open-circuit voltage (V_{OC}), fill factor (FF), dark saturation current density (J_0), and series resistance (R_S). However, solar cells are large area devices that often have significant variation in these parameters over the surface of the entire device. Photoluminescence (PL) imaging is a method commonly used by the photovoltaics (PV) industry and RD community to determine the spatial distribution of these parameters. The speed and relative simplicity of the measurement make it applicable as both an off-line and in-line metrology technique.

There have been numerous efforts to obtain spatial distributions of the performance parameters from both PL and electoluminescence (EL) signals. Fuyuki et al. developed a way of determining the spatial distribution of minority carrier diffusion length from EL [61]. PL imaging with an electrical bias have been used to obtain images of R_S [156, 107]. Glatthaar et al. mathematically derived the spatial voltage distribution from the luminescence images of a silicon solar cell and two different models namely terminally connected diodes and interconnected diodes for determination of spatial maps of the physical parameters [66]. PL imaging has also been used to obtain images of efficiency [25, 147, 179] and the recombination occurring in the perimeter of the cell [60]. In all of the methods above, a global value of J_{SC} is assumed. It has been demonstrated that J_{SC} is not actually uniform, but instead varies spatially across the cell. The impact of this assumption on the resulting parameter images is not clear. Several authors have suggested that it may result in substantial inaccuracies [147, 100, 55, 179].

In this work, the impact of using a global J_{SC} value is investigated. We explore how this assumption influences the images obtained for efficiency, FF, J_0 , and R_S . The J_{SC} images used in this work

are obtained using a high-speed external quantum efficiency (EQE) and reflectance measurement system capable of rastering over the entire surface of solar cells, a technique introduced previously [174, 145]. Images of efficiency, FF, J_0 , and R_S are created using both the global J_{SC} and the spatially-resolved J_{SC}. Additionally, two different methods of determining the efficiency and FF are also compared: one relies on the PL image when the terminal voltage is set to the max-power voltage; the other relies on the generation of a J-V curve using the various parameters obtained and the Shockley diode equation. Finally, the approach presented here can be used to diagnose the root cause of defective areas within a solar cell by further analyzing the QE and reflectance images and decoupling losses based on position (i.e., front or rear side of the device) and mechanism (e.g., reflectance, parasitic absorption, recombination).

Methodology

The methodology presented in this work relies on the spatially-resolved EQE data as a direct measurement of the local J_{SC}, which is assumed to be equal to the local photogenerated current density (J_{ph}). PL images are then captured under various external bias and illumination conditions to generate images of local voltage. From there, images of cell performance parameters are obtained using the methods outlined in this section.

Local Photogenerated Current

The local photogenerated current J_{SC} is obtained at each point on the solar cell using the following equation [87, 145].

$$J_{SC} = e \int_{365nm}^{1200nm} \Phi_{inc}(\lambda) \, EQE(\lambda) \, d\lambda \qquad (5.1)$$

Here e, EQE and Φ_{inc} are the charge of an electron, external quantum efficiency and incident photon flux respectively. An AM1.5G solar spectrum from 365 nm to 1200 nm was considered for this calculation.

Local Voltage

The well-known correlation between luminescence intensity and local voltage of a semiconductor substrate or solar cell results in the following expression relating the luminescence intensity Φ_{xy} at a position (x,y) to the local voltage at that same position [62, 156].

$$\Phi_{xy} = C_{xy} \cdot \exp\left(\frac{V_{xy}}{V_T}\right) + \Phi_{offset} \tag{5.2}$$

Here, V_{xy} and V_T are the local junction voltage and thermal voltage respectively. C_{xy} is a calibration constant independent of both the electrical bias and the illumination conditions. The offset part of luminescence intensity Φ_{offset} emerges because of the diffusion limited (i.e., voltage-independent) carrier recombination [103, 5, 156]. It is proportional to the illumination intensity I_L and can be expressed as,

$$\Phi_{offset} = B_{xy} \cdot I_L \tag{5.3}$$

Here B_{xy} refers to the background luminescence signal. According to Glatthar's approximation [66], for a PL image taken at the same illumination condition I_L with the cell operating in the short-circuit condition, the resulting PL intensity becomes equal to the offset PL intensity, Φ_{offset} [99]. The background B_{xy} is calculated from this short-circuit PL image Φ_{offset}. Substituting Φ_{xy-SC} for Φ_{offset} and I_{L-SC} for I_L we can write,

$$B_{xy} = \frac{\Phi_{xy-SC}}{I_{L-SC}} \tag{5.4}$$

The calibration constant C_{xy} is determined from an open-circuit PL image Φ_{low}, taken with a sufficiently low illumination I_{low},

$$C_{xy} = \left[\Phi_{xy-low} - B_{xy} \cdot I_{low}\right] \cdot \exp\left(-\frac{V_{OC-low}}{V_T}\right) \tag{5.5}$$

Here, V_{OC-low} is the measured open-circuit voltage at the low illumination intensity I_{low}. The key assumption is that, at a sufficiently low illumination intensity, the lateral gradient of open-circuit voltage is negligible. The intensity regime considered to be 'sufficiently low' was investigated by Hoffler [99]. They observed that for 0.19 sun illumination, the maximum voltage difference over a multicrystalline silicon cell was only 5mV, concluding that 0.19 sun was sufficient for the calibration purpose. For this work, a conservative illumination intensity of 0.1 sun was used to capture the open-circuit PL image used in the calculation of C_{xy}. With C_{xy} and B_{xy}, the voltage distribution V_{xy} can be determined for any arbitrary PL image Φ_{xy} using the following relation,

$$V_{xy} = V_T \cdot \ln\left(\frac{\Phi_{xy} - B_{xy} \cdot I_L}{C_{xy}}\right) \tag{5.6}$$

Local Series Resistance and Dark Saturation Current Density

Images for R_{S-xy} and J_{0-xy} can be calculated using the terminal connected diode model shown in figure 5.1. In this model, a solar cell can be considered as a combination of parallel diodes which are connected to a common terminal through their individual series resistances. The figure comprises of three units (three parallel diodes) each having a distinct J_{ph-xy}, R_{S-xy}, J_{0-xy}. An infinite shunt resistance is typically assumed for analysis purposes. With V_{term} and n as the terminal voltage and the ideality factor of the diode, respectively, then this model results in the following equation,
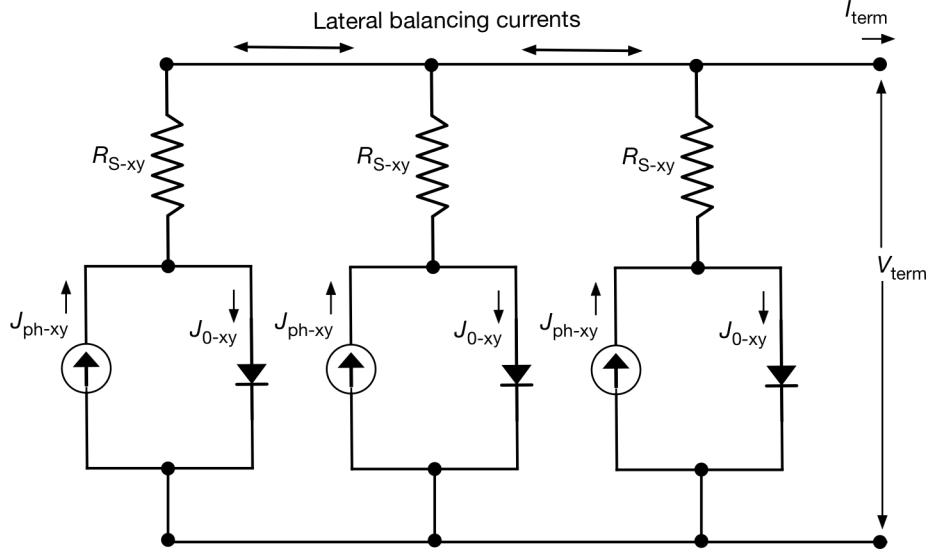
Figure 5.1: Illustration of the terminal connected diode model from [99]

$$V_{term} - V_{xy} = R_{S-xy} \left[J_{0-xy} \exp\left(\frac{V_{xy}}{nV_T}\right) - J_{ph-xy} \right] \qquad (5.7)$$

For the ideality factor, a global n can be assumed as an ideal diode (n = 1) [66, 99] or a variable n can be used [147]. A spatially-resolved ideality factor can also be used [179, 75]. In this work, we use a global n for simplicity and compare the cases where $n = 1$ and the more realistic case where n is not equal to 1. In previous works to date, a global J_{SC} was assumed for quantitative PL techniques. As mentioned previously, in this work a point-by-point J_{SC-xy} measurement is obtained, which we use as J_{ph-xy} in this analysis (i.e., $J_{SC-xy} = J_{ph-xy}$).

R_{S-xy} and J_{0-xy} are the two remaining unknowns in equation 5.7. Therefore two additional measurements with different terminal voltages, but the same illumination condition is required.

66

Local Efficiency using PL at V = V_{MPP}

To calculate the efficiency image of the cell, we need VMPP-xy and J_{MPP-xy} distribution over the cell. In this work, two methods of obtaining these distributions were investigated. The first method relies on obtaining V_{MPP-xy} and J_{MPP-xy} from an additional PL image. To achieve this, an additional biased PL measurement was done at global V_{MPP} value of the cell at 1 sun condition (which comes from the illuminated I-V measurement). Plugging it into equation 6 provides a V_{MPP-xy} distribution of the cell. Then J_{MPP-xy} is obtained from the single diode model J-V curve [147, 148].

$$J_{MPP-xy} = J_{SC-xy} - J_{0-xy} \left[e^{\frac{V_{MPP-xy}}{n_{xy}V_T}} - 1 \right] \tag{5.8}$$

The efficiency image can be calculated using,

$$Eff_{xy} = \frac{P_{out-xy}}{P_{in}} = \frac{V_{MPP-xy} \cdot J_{MPP-xy}}{1000\ Wm^{-2}} \tag{5.9}$$

Here $P_{in} = 1000\ Wm^{-2}$ is the input power density used in our experiment as the standard test condition. Noticeably the spatial distribution of the J_{SC} (i.e. J_{SC-xy}) is used in the equation 5.9 as opposed to the previous works that used a uniform J_{SC} [148].

Local Efficiency and Fill Factor using J − V Curve Fit

To provide additional insights into the impact of a spatially resolved current density, a method using locally generated $J - V$ curves to calculate efficiency was also explored. The method is similar to the approach introduced by Breitenstein [24, 22]. In their approach, dark lock-in thermography is used to generate key parameter maps including J_{01} and J_{02} and a 2-diode model is used to model each individual pixel. In this work, PL imaging is used to generate parameter maps for R_S and J_0 and EQE data is used to generate J_{SC} maps. The key difference here is the use of a single diode

equation where the ideality factor can be adjusted. Since we have the local value of J_{SC}, J_0 and R_S, we can plug these into the diode equation,

$$J_{xy} = J_{SC-xy} - J_{0-xy} \left[\exp \left(\frac{V_{xy} + R_{S-xy} \cdot J_{xy}}{nV_T} \right) - 1 \right] \qquad (5.10)$$

V_{MPP-xy} and J_{MPP-xy} are obtained by finding the maximum power point of the $J - V$ curve in equation 5.10. Then the local efficiency images can be calculated using equation 5.9.

The FF_{xy} image can be obtained from V_{MPP-xy} and J_{MPP-xy} using,

$$FF_{xy} = \frac{V_{MPP-xy} \cdot J_{MPP-xy}}{V_{OC-xy} \cdot J_{SC-xy}} \qquad (5.11)$$

Here V_{OC-xy} is the spatially resolved open circuit voltage distribution over the cell. To compare the two methods of efficiency calculation, the first method requires an $I - V$ measurement and PL measurement at 'global MPP', whereas the second method requires two additional biased PL images from which it determines the voltage and current density images at 'local MPP', other variables being the same. The second method requires more computational power as it requires an independent determination of the $J - V$ curve for each pixel in the image.

Experimental Details

An industrial multicrystalline Si Al-BSF solar cell was used in this work, featuring a silicon nitride (SiNx) antireflection coating, isotropic texturing, screen-printed contacts, and an overall area of 243 cm^2. A multicrystalline cell was chosen due to the larger spatial variation in J_{SC} and J_0 compared to monocrystalline solar cells. A Tau Science FlashQE system was used to measure the external quantum efficiency (EQE) and reflectance (R) over the surface of the cell. This system uses individually controlled LEDs featuring 41 distinct wavelengths (λ) between 365 nm and 1280

nm. These LEDs act as the spectrally-resolved light source and have an illuminated spot size of approximately 3mm. The system has electronics to measure the current at each wavelength for EQE(λ) and an integrating sphere with photodetectors to measure R(λ). A full-spectrum EQE(λ)) and R(λ)) measurement is performed simultaneously in one second. This measurement system was programmed to raster over the entire surface of the solar cell to create a 97 x 97 image of EQE(λ) and R(λ) [145, 89]. The resulting 97 x 97 J_{SC-xy} image was then converted into a 960 x 960 image using a linear interpolation. This interpolation was performed to achieve the same number of matrix elements in both the J_{SC-xy} images and the PL images. The mean J_{SC} (i.e., averaged over the entire surface of the cell) of the original 97 x 97 image and the interpolated 960 x 960 image are equal ($J_{SC} = 32.2\ mA/cm^2$). Performing interpolation on a low-resolution image is not unusual; the linear interpolation was used previously on current density images using the LBIC method [129, 55]. Once the J_{SC-xy} image was obtained, it was then used to calculate images of J_0, R_S, FF, and efficiency.

Illuminated $I - V$ measurements were performed with a BT Imaging LIS-R1 system with an 808 nm laser as the light source. First, to determine the one sun condition, global J_{SC} measurements were performed on the cell and the photon flux was varied until the global J_{SC} measured matches the spatially averaged J_{SC} obtained from the QE measurement. For the cell used in this study, a photon flux of $3.06x10^{17}\ cm^{-2}s^{-1}$ and $3.06x1016\ cm^{-2}s^{-1}$ were considered as the 1 sun and 0.1 suns respectively. The global cell parameters were obtained for the cell using the 1 sun illuminated $I - V$ curve from the LIS-R1 system (Table 1). The cell showed an overall efficiency of 15.40%, with J_{SC}=32.2 mA/cm^2 and V_{OC}=0.612 V. The global value for R_S was obtained using Suns-V_{OC} and illuminated $I - V$ curves following the method in [150]. The global J_0 and n were obtained via curve fitting with the software tool described in [141, 154] which are $3.39x10^{-10}\ A/cm^2$ and 1.3 respectively.

The LIS-R1 system was also used for the PL imaging. It features an 808 nm laser, 920 nm long-

pass filter, and 1-megapixel silicon CCD camera. The LIS-R1 system also features a test chuck and power supply to electrically bias solar cells during the imaging process. Two biased PL images were taken at 1 sun for the calculation of J_{SC-xy} and J_{0-xy}. A PL image at 0.1 suns with the device at open-circuit (J = 0) was taken and a 1 sun image with the device at short-circuit (V = 0) were taken for the calculation of the background (equation 4) and the 1 sun V_{OC-xy} image. An additional biased PL image was taken at 1 sun with the device held at the MPP ($V = V_{MPP}$) to obtain efficiency images for one of the methods explored.

Table 5.1: Global values of the cell parameters calculated from illuminated $I - V$ and Suns-V_{OC} measurement

Parameter	Value
Efficiency	15.4%
J_{SC}	32.2 mA/cm^2
V_{OC}	0.612 V
FF	0.78
R_S	0.2 Ω-cm^2
Ideality factor	1.3
J_{0-xy}	3.39 x 10^{-10} A/cm^2

Results and Discussion

Current and Voltage Images

The 97 x 97 J_{SC} image obtained from the spatially-resolved EQE data and equation 1 is shown in Fig. 2(a). To be able to use both the J_{SC-xy} and V_{OC-xy} images together in the same equation for further analysis, the matrix size has to be the same for both parameters. To increase the matrix size of the J_{SC-xy} image, a spatial linear interpolation was used, as shown in figure 5.2(b). Both the original and interpolated J_{SC-xy} images and their histograms appear very similar and have equivalent spatial averages (32.2 mA/cm2). This spatial average includes the busbar regions of

70
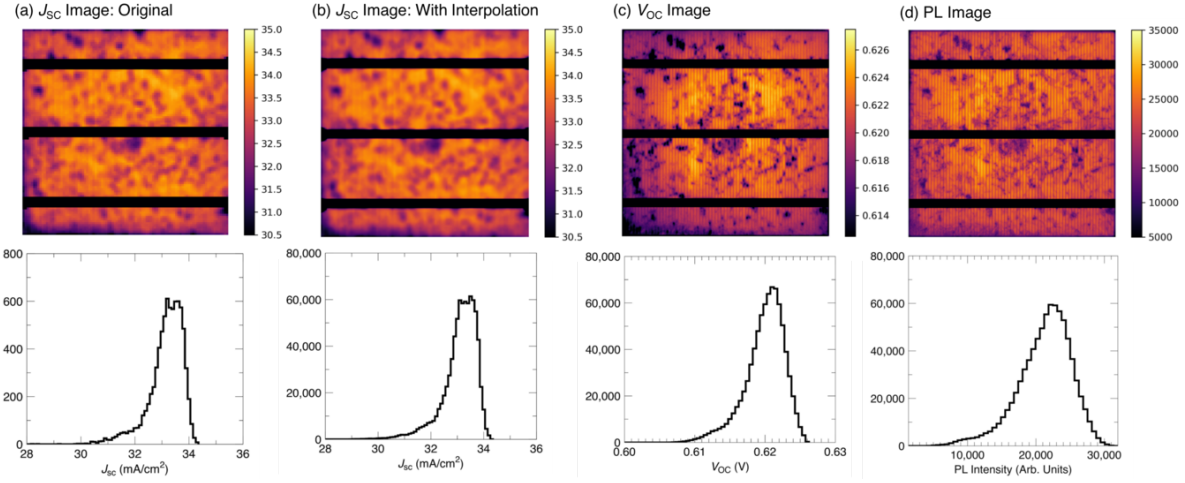
Figure 5.2: Images of J_{SC}, V_{OC}, and the uncalibrated PL signal and their histograms: (a) Original J_{SC} image of size 97 x 97 pixels; (b) interpolated J_{SC} images 960 x 960 pixels; (c)V_{OC} image; and (c) uncalibrated PL image.

the cells and is equal to the global J_{SC} shown in table 5.1. Since little information can be gained from the busbar region, this region is excluded for the analysis presented in this work. The global current density excluding the busbar regions (from global IV curve) is 33.1 mA/cm^2, which is close to the mode of the J_{SC-xy} histogram. Noticeably, the shape of the histogram is not a symmetrical Gaussian curve but is skewed, featuring a tail on the lower end of the histogram arising from the presence of the J_{SC} loss mechanisms.

Figure 5.2(c) shows the V_{OC} image and histogram of the cell calculated using the necessary PL images and equation (6). The uncalibrated PL image taken at one sun and at open-circuit is shown in figure 5.2(d). Looking at all of the images in figure 5.2, it's clear that the presence of the grain boundaries and dislocations affects the PL signal, the local voltage, and the local current. The patterns are noticeably similar for the J_{SC} and V_{OC} images, with dark regions showing up in both. This is due to the known reciprocity between luminescence and quantum efficiency of a solar cell [112, 113, 114, 138]. Locations with strong PL emission also have strong QE response (i.e. higher

local current and voltage). The spatial average of V_{OC} distribution is 0.62 V, which lies as the mode of the V_{OC} histogram, similar to J_{SC}.

Series Resistance and Saturation Current Density Images

Series resistance (R_S) and dark saturation current density (J_0) are two important parameters of a solar cell which influence the shape of the $I-V$ curve. The terminal connected diode model in equation 5.7 allows the determination of R_S and J_0 maps from two biased PL images. Figure 5.3 presents four images of R_S and four images of J_0 for the same cell, where the images were created using different inputs for J_{SC-xy} (i.e., global J_{SC} versus J_{SC-xy}) and for the global ideality factor (ideal diode case, n = 1 versus actual case, n = 1.3). Unlike the V_{OC} and J_{SC} images, the R_S and J_0 images are very different from each other. The dislocations and high recombination crystal grains seen in the J_0 images are not evident in R_S images, as expected. The vertically aligned rectangular features with high resistance seen in the R_S images, denoted by dashed green rectangles in the top left image of figure 5.3(a), are the well known sign of broken gridlines at the front of the cell [156].

Comparing the histograms for R_S, the increase in the ideality factor results in a slightly higher mode of about 0.1 Ω-cm^2 for R_S and minor broadening of the distribution. The shape of the R_S distribution is rather symmetrical, lacking the skew observed in the distributions of J_{SC} and V_{OC} (figure 5.2). The difference between the assumption of a global J_{SC} and spatially-resolved J_{SC-xy} makes virtually no difference for both ideality factors. This suggests that the use of a global J_{SC} is a safe assumption when creating R_S images.

The J_0 images in figure 5.3(b) illustrate the distribution of recombination losses across the solar cell. Crystallographic defects like dislocation clusters and recombination active grain boundaries, as well as regions featuring higher concentrations of deleterious impurities (e.g., Fe) are the most common causes of the local regions with high J_0. The shape of the J_0 distribution shown in the
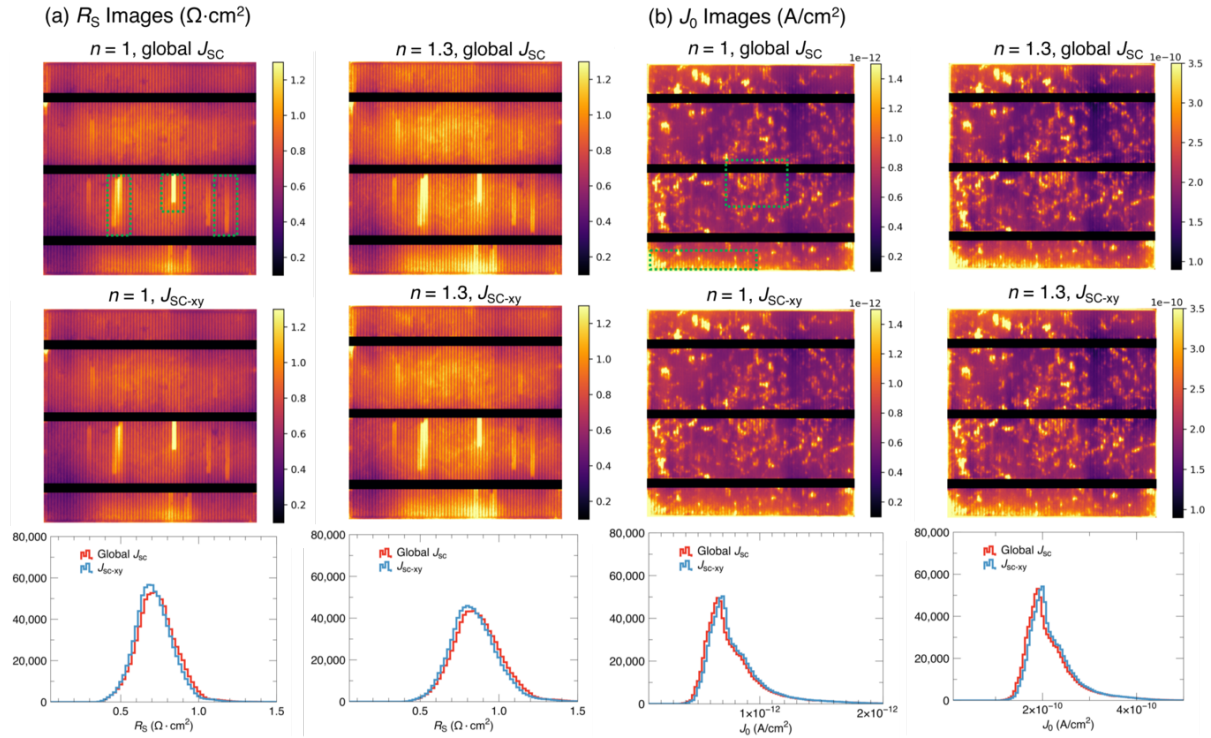
Figure 5.3: (a) Series resistance images and histograms. (b) Dark saturation current density images and histograms

histograms is skewed like the V_{OC} and J_{SC} distribution from figure 5.2. In the case of J_0 though, the tail is on the higher end of the distribution. This makes sense as the regions with a high J_0 would be expected to have a low V_{OC} and low J_{SC}. J_0 is on the order of 10^{-12} A/cm^2 for the ideal diode assumption of n = 1, and as expected, it is much higher for the n = 1.3 case (10^{-10} A/cm^2). There is no perceivable change in the J_0 images after incorporation of the spatially-resolved J_{SC-xy} rather than a global J_{SC}. As in the case of RS, this suggests global J_{SC} is a safe assumption for calculating the local J_0. In all four of the J_0 images, there is no sign of the R_S defects like the vertical rectangles caused by broken gridlines. This indicates that all of the assumptions here successfully decouple the resistive losses from the recombination losses.
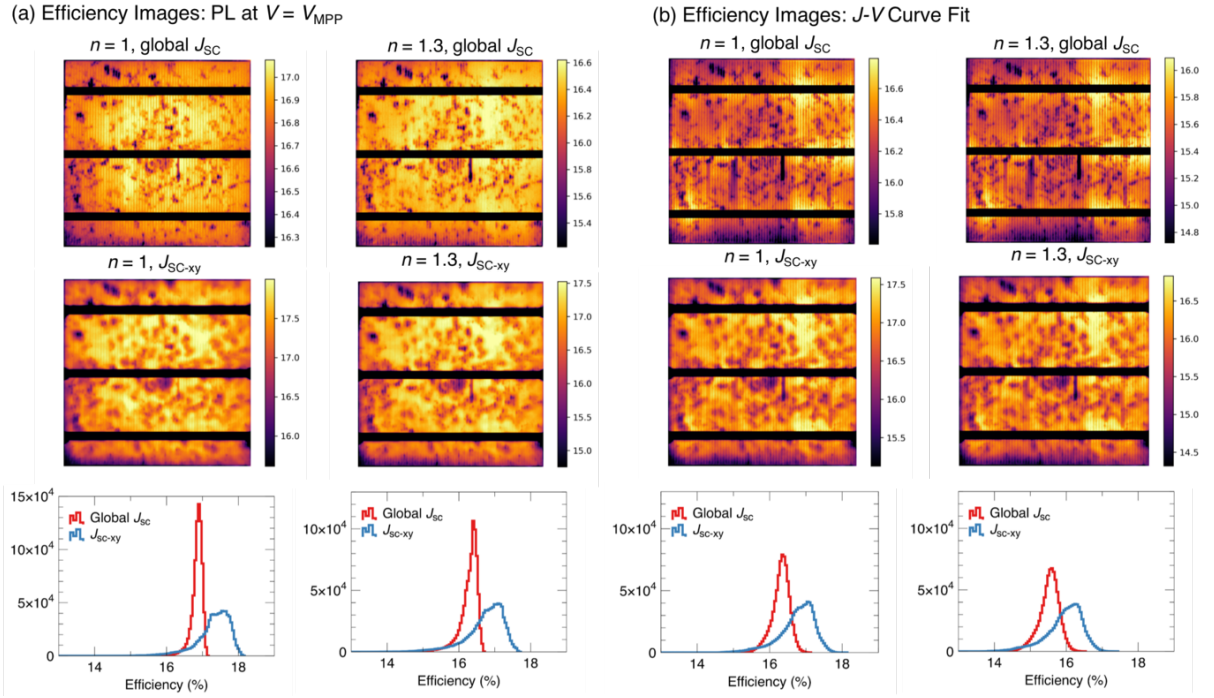
Figure 5.4: Efficiency images and histograms using: (a) the PL image at a bias voltage of $V = V_{MPP}$; and (b) the $J - V$ curve fitting method.

Efficiency and Fill Factor Images

Figure 5.4 presents the efficiency images for both methods discussed previously. The colorbars for all images in this figure are scaled independently using the 1st percentile and 99th percentile as the minimum and maximum, respectively, excluding busbars. This is done to aid in the visual comparison. The incorporation of the spatial current density has a significant impact on the derived efficiency images. There is an increase in the contrast between the good and bad regions of the device. The histograms clearly describe this impact, as the distribution of efficiency has both shifted and widened with the incorporation of J_{SC-xy}. When an ideal diode is considered (i.e., n = 1), the mean increased from 16.8% to 17.5% and when the actual global ideality factor of 1.3 is used, the mean increased from 16.4% to 17.1%. The efficiency images are largely influenced

74
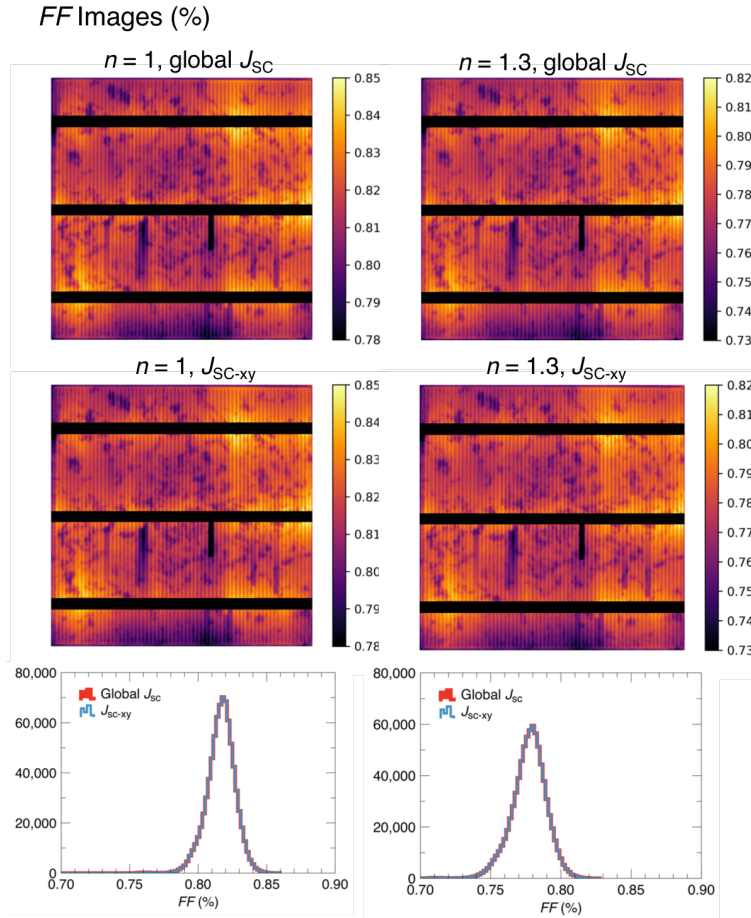
Figure 5.5: Fill factor images and histograms.

by recombination losses including the sites associated with dislocations and grain boundaries. It is worth mentioning here that we did not separate the edge recombination from the total recombinationin in the device for simplicity; edge recombination can lead to reduced efficiency value of a cell [60]. Series resistance related defects appear to have only a minor influence on the local efficiency, although these regions are more pronounced in the $J-V$ curve fit method. For both methods, the resulting efficiency images including J_{SC-xy} have remarkably similar distributions.

Although it is not directly related to optoelectronic properties, the fill factor is useful in perfor-

mance evaluation of a solar cell. It dictates the shape of the $I - V$ curve. A spatial map of fill factor could account for the relative difference of performance over the surface of a cell. The fill factor images in figure 5.5 are affected by both the series resistance and the dark saturation current density. Increasing the ideality factor from 1 to 1.3 lead to a decrease in the mean fill factor from 0.82 to 0.78. For both cases, incorporation of spatial current density does not change the fill factor at all. Fill factor is a ratio between the maximum power of the $I - V$ curve and the maximum power attainable if there was no loss present.

Loss Analysis using Quantum Efficiency

The images of EQE and R used to create the J_{SC-xy} input parameter in this work can also be used for loss analysis of the solar cell. This is particularly useful when trying to attribute optical and recombination losses to a particular layer or interface within the device. The details of this approach were described in prior work [145, 12], but here we provide a brief description for the sake of information. The internal quantum efficiency (IQE) at a point over the cell can be calculated from the measured value of EQE and R at that point,

$$IQE(\lambda) = \frac{EQE(\lambda)}{1 - R - f_{eff}} \tag{5.12}$$

Here f_{eff} is the effective optical shaded fraction within the measurement light-spot, occurring due to the presence of the gridlines. Now according to the model proposed by Fischer et al., IQE can be expressed in terms of the effective diffusion length L_{eff}, absorption length of silicon (L_a) and an scaling factor (k) as following,

$$IQE(\lambda) = \frac{1}{k} \exp\left(-\frac{W_d}{L_a(\lambda)}\right) \frac{1}{1 + \frac{L_a(\lambda)}{L_{eff}}} \tag{5.13}$$

Here W_d is the thickness of a hypothetical dead layer which accounts for the parts of the emitter which do not contribute to the photogenerated current because of recombination occurring. L_a is used from the literature and IQE from equation 13. Running a simple iterative process starting with the reasonable guess for the rest of the parameters provides the the value of k, L_{eff} and W_d. Here, the slope and intercept of the $\ln\left(IQE \cdot \left(1 + \frac{L_a}{L_{eff}}\right)\right)$ vs. $\frac{1}{L_a}$ plot at any wavelength provides the values for Wd and k respectively at that wavelength. These values are then used for plotting $\frac{1}{IQE}\exp\left(\frac{W_d}{L_a}\right)$ vs. L_a graph which then provides the values for L_{eff} and W_d.

Once the L_{eff} and W_d values become available, they can be used for calculating the losses in emitter. The total loss in emitter can be divided into two discrete wavelength regimes: (I) 365 nm - 500 nm, where the dead layer approximation is inadequate and (II) 500 nm - 1280 nm, where the dead layer approximation is reasonable. With this, the IQE loss in emitter can be expressed as,

$$IQE_{loss, emi, I} = 1 - IQE\left(\lambda\right) \cdot \left(1 - \frac{L_a\left(\lambda\right)}{L_{eff}}\right) \tag{5.14}$$

$$IQE_{loss, emi, II} = 1 - \exp\left(-\frac{W_d}{L_a\left(\lambda\right)}\right) \tag{5.15}$$

Now the total current loss in emitter J_{loss-e} can be calculated from the these IQE loss values. The rest of the parasitic loss is then attributed to the loss in the base (J_{loss-b}). Fig 5.6 shows results of such analysis including maps of the L_{eff}, J_{loss-e} and J_{loss-b} and compares this with what is seen in the PL image. Regions associated with a high density of dislocations are highlighted in green and are associated with lower effective diffusion lengths and higher current loss in the base of the device. The same regions also showed high magnitude in the J_0 image (5.3) and low magnitude in the J_{SC} (figure 5.2(a)) and V_{OC} (5.2(c)) images. The current loss in the base is significantly larger than the current loss in the emitter. Although the impact is minor, the spatial variation of the dopant concentration in the emitter, with a higher dopant concentration near the edges of the device, can be identified in figure 5.6(b). This pattern is not present in any of the parameter maps
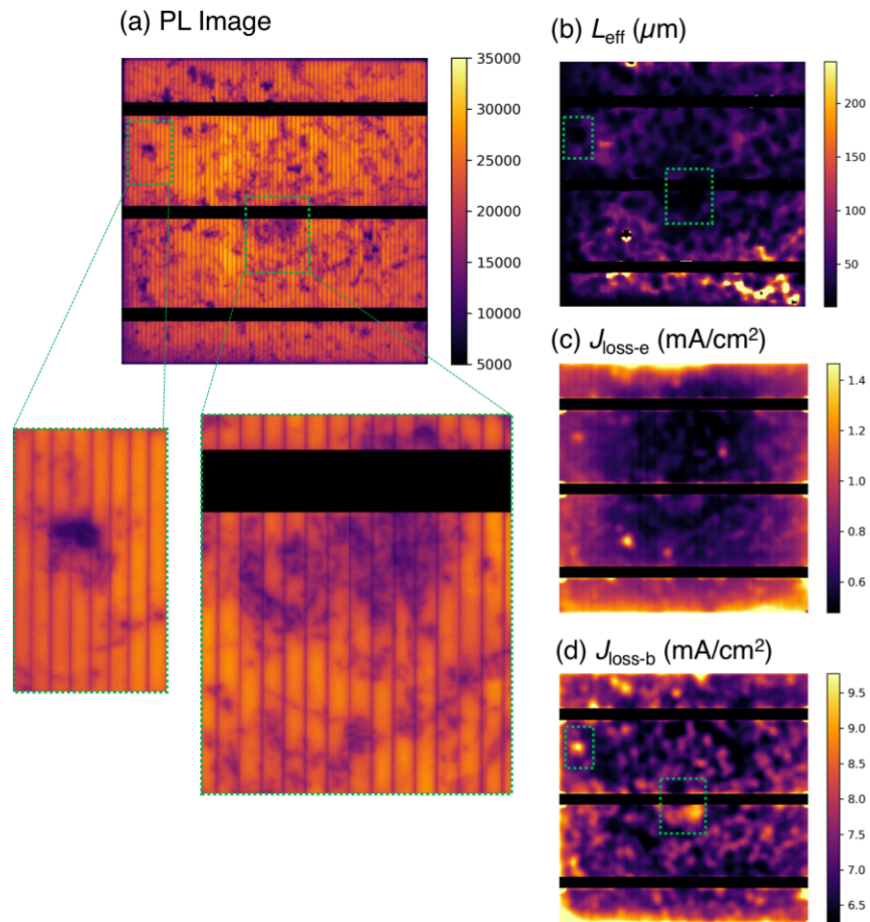
Figure 5.6: The result of loss analysis. (a) PL image (b) effective diffusion length (c) emitter loss (d) bulk and rear loss due to parasitic absorption.

derived from PL images alone. The combination of both spatially resolved PL and QE provides a complete picture of where the losses are occurring within the device and the impact they have on overall performance.

Conclusion

In this work, a method of using the local photogenerated current as an input to create images of solar cell parameters (e.g., efficiency) is presented. Various methods of extracting cell parameters images using photoluminescence were carried out on the same multicrystalline silicon Al-BSF solar cell with an emphasis on any changes that occur when assuming a uniform global J_{SC} across the entire cell versus a local J_{SC-xy} obtained using spatially-resolved quantum efficiency measurements. The application of a local J_{SC-xy} had a negligible influence on the extraction of R_S, J_0, and fill factor, indicating the use of a global J_{SC} is likely a valid assumption for these parameters. In stark contrast, the use of a local J_{SC-xy} had a large influence on the extraction of local cell efficiency, increasing the mode of the local efficiency histogram and broadening the distribution. Additionally, this method has the benefit of using the spatially-resolved quantum efficiency and reflectance data for loss analysis when evaluating areas with particular poor performance (e.g., high J0, low efficiency). This can be used to identify the root cause of manufacturing defects and to evaluate how spatial variance in parameters like the effective diffusion length, current loss in the emitter, current loss in the base, front surface reflectance losses, and escape reflectance.

Acknowledgements

CHAPTER 6: LOSS MEASUREMENT: A COMPREHENSIVE METHODOLOGY TO EVALUATE LOSSES AND PROCESS VARIATIONS IN SILICON SOLAR CELL MANUFACTURING

Part of this chapter was published in **M. J. Hossain**, G. Gregory, H. Patel, S. Guo, E. J. Schneller, A. M. Gabor, Z. Yang, A. L.Blum, and K. O. Davis. 2018 IEEE 7th World Conference on Photovoltaic Energy Conversion (WCPEC), pages 2214–2218, 2018 [89] and **M. J. Hossain**, G. Gregory, E. J. Schneller, A. M. Gabor, A. L. Blum, Z. Yang, D. Sulas,S. Johnston, and K. O. Davis. IEEE Journal of Photovoltaics, 9(5):1350–1359, 2019 [90].

Novel, high-throughput metrology methods are used in this work for detailed performance loss analysis of approximately 400 industrial crystalline silicon solar cells, all coming from the same production line. The characterization sequence combines traditional global cell measurements (e.g., current-voltage, Suns-V_{OC}) with camera-based cell imaging of voltage distribution and power dissipation from photoluminescence and lock-in thermography, respectively. Spatial variations in current collection are visualized using a high-speed external quantum efficiency and reflectance measurement technique. A non-destructive transfer length method (TLM) measurement technique is also implemented, featuring circular TLM structures hidden within the busbars of the cells. The variance of individual loss parameters and their impact on cell performance are quantified for this large group of cells. Based on correlations performed across parameters, recombination losses in the bulk and rear surface of the cell are shown to be the primary limiting factor for the cell efficiency. The nature of these distributions and correlations provide important insights about loss mechanisms in industrial solar cells, helping to prioritize efforts for optimizing the performance of the production line. Additionally, many of the parameters extracted from these techniques can be tied back to incoming material quality issues (e.g., poor bulk carrier lifetime, nonuniform wafer

doping) and to individual unit processes (e.g., texturing, phosphorus diffusion, silicon nitride deposition, metallization), allowing the data to be used directly for process control in manufacturing. All of the datasets are made available for download.

Introduction

Ensuring quality and predictability of manufacturing processes is a crucial part of manufacturing photovoltaic (PV) cells with good performance and low cost. Unlike integrated circuit (IC) and light emitting diode (LED) industries, which keep redundant components to compensate for the defective components, the performance of a PV system is affected by any defective cell present [11, 94]. For a series-connected string or sub-string of PV cells, the total photogenerated current of the string/sub-string is limited by the cell with the lowest current. Therefore, minimizing the variance of the solar cell performance parameters is always desired. These variances occur as a result of the different loss mechanisms present in the cell and the variations in the manufacturing processes [89]. Smaller process variations amongst cells can even potentially benefit the long-term reliability and durability of PV modules [123]. There are numerous methods to detect these process variations in-line [37, 158]. Some examples include measuring wafer thickness and its variation using capacitance based techniques [79], identification of crystallographic defects and cracks using photoluminescence (PL) imaging [80, 38], and the measurement of the bulk lifetime using microwave-detected photoconductance decay [143] or using quasi-steady-state photoconductance [152]. These types of mid-stream measurements are very valuable, but the insights obtained from them can be limited, especially if the wafer has an unpassivated surface or hasn't yet been metallized [79].

Many characterization and analysis options are available to evaluate a finished solar cell. Illuminated current-voltage (*I-V*) measurements, or *J-V* if using current density, at standard test con-

81

dition (AM 1.5G solar spectrum, 1000 W/m^2 illumination and 25ngerman°C temperature) allows determination of important cell parameters like efficiency, short-circuit current density (J_{SC}), open-circuit voltage (V_{OC}), and fill factor (FF) and is used to bin cells based on these parameters [56]. This is perhaps the only measurement method performed on every silicon solar cell produced everywhere in the world. The Suns-V_{OC} measurement [110] is another basic method which provides information about recombination losses, the presence of shunts in the cell, and can be used to accurately measure series resistance (R_S) when coupled with an illuminated I-V measurement. This method has long been performed as an off-line technique and is used in-line by some solar cell manufacturers. External quantum efficiency and reflectance (EQE + R) measurements are another common measurement technique used to analyze J_{SC} losses in solar cells and identify the source of those losses (e.g., emitter, bulk, rear) [12]. This method is commonly used off-line, but not in-line, due to the amount of time it takes to perform the measurement. High-speed EQE measurement options that can perform this measurement in less than one second are now available though, enabling this technique to be potentially used in-line [175]. To determine the contact resistivity and sheet resistance, transfer length method (TLM) measurements can be used [146, 72, 124]. This is normally done using a destructive process, wherein the cell are laser scribed and cleaved. Non-destructive techniques using circular TLM (cTLM) hidden within the busbars of the solar cells are now available that allow this technique to be used in-line [70]. In addition to these methods that provide the global performance parameters of cells, open-circuit PL imaging can be used to obtain spatially-resolved images of V_{OC}, and biased PL imaging can be used to create images of R_S, dark saturation current density (J_0), and efficiency [156, 66, 179, 147, 92]. Spatially-resolved EQE measurements, coupled with reflectance spectroscopy, provide a way of creating J_{SC} images and images of the J_{SC} loss due to individual loss mechanisms [145].

In this work, five different measurement techniques were carried out on approximately 400 industrial crystalline silicon (c-Si) solar cells, all from the same production line, and will present a

comprehensive performance loss analysis on this statistically relevant group of cells. The five measurement techniques include: (1) illuminated *I-V* at standard test conditions; (2) Suns-V_{OC}; (3) PL imaging; (4) high-speed quantum efficiency and reflectance spectroscopy; and (5) non-destructive transfer length method (TLM) measurements [70]. Spatially resolved loss analysis was also carried out for three individual cells i.e. a good cell, a moderate cell and a poorly performing cell. It decouples different current loss mechanisms and attributes these to a number of defect types present in the cells. This work represents a more detailed enhancement of a previous proceedings publication [89]. Additions to this manuscript include additional correlation results between device parameters, shown in Figure 6.5(d), V_{OC} and DLIT (dark lock-in thermography) images of three individual cells (Figure 6.6), a comparison of different imaging techniques for precisely locating shunts and other defects (Figure 6.7), and loss analysis for individual cells. The totality of this work creates a complete picture of losses and process variations in industrial silicon solar cells, and these datasets are available for public download for other researchers to perform their own statistical analysis and data mining [48, 46, 47, 57, 166]

Experimental Details and Analysis Techniques

The c-Si solar cells used in this work are 243cm^2 multicrystalline silicon cells featuring five busbars, as in the proceedings paper [**?**]. These are industry standard Al-BSF (aluminum back surface field) cells, featuring isotropic texturing, a SiN_x anti-reflection coating (ARC), phosphorus-doped n^+ emitter on the front, screen-printed Ag front contacts, and a full area screen-printed Al rear contact that forms the p^+ BSF upon firing. The only difference in these cells compared to commercial cells are the cTLM structures hidden within the busbars, which don't influence the cell processing or performance (Figure 6.1).

Illuminated *I-V* curve measurements under standard test conditions and Suns-V_{OC} measurements
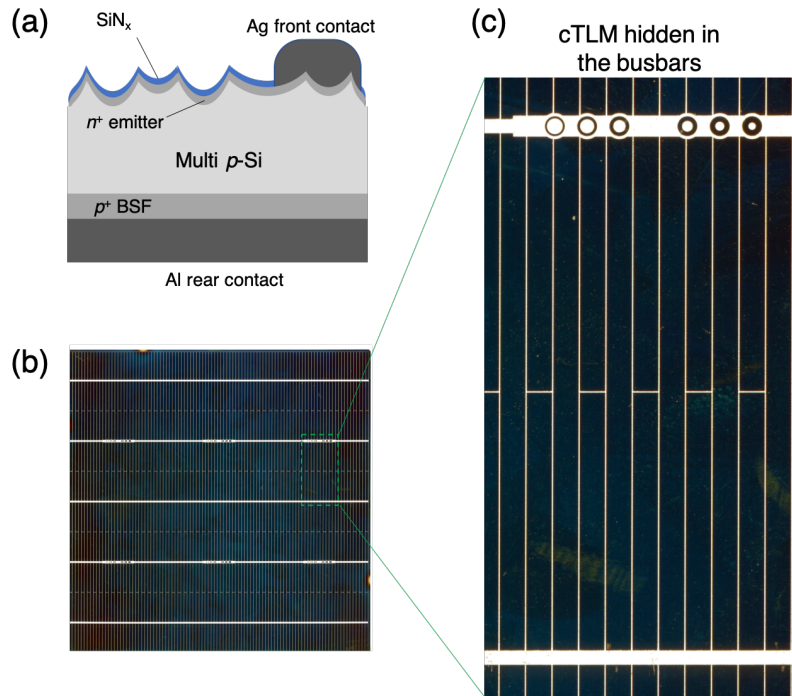
Figure 6.1: (a) Illustration of the multi Al-BSF cell architecture. (b) Scanned image of the cells used in this study and (c) a zoomed in image of the cTLM structures hidden within the busbars of the cells.

were performed using a Sinton Instruments FCT-750 in-line cell tester. The FCT-750 is a production cell tester capable of measuring cells at line speeds of 3,600 cells per hour [89]. This cell tester is unique in that it reports conventional cell test parameters (e.g., I_{SC}, V_{OC}, R_S, R_{SH}, power, efficiency, fill factor) and supplements these parameters with advanced Suns-V_{OC} analysis and substrate doping measurement. The Suns-V_{OC} analysis allows for a true R_S measurement, pseudo *I-V* parameter measurement without the effects of R_S, and carrier lifetime data.

Open-circuit PL images were obtained with a BT Imaging *LIS-R1* system, an off-line R&D tool. PL imaging was carried out at two injection levels, 0.1 suns and 1 sun, to obtain the spatial distribution of V_{OC} over the cells. The integration time was chosen in such a way that the output PL

count is high enough to efficiently suppress the noise. In this work 10s and 1s were the integration time for 0.1 suns and 1 sun PL measurement respectively. The laser in *LIS-R1* illuminates the sample with 808 nm light [89]. The emitted PL spectrum is captured by a 1-megapixel silicon CCD camera after getting filtered by a 920 nm long pass filter. In this measurement $3x10^{17}$ cm^{-2} s^{-1} and $3x10^{16}$ cm^{-2} s^{-1} photon flux were assumed for 1 sun and 0.1 sun, respectively, and were determined based on changing the photon flux until the global J_{SC} of the cell under laser illumination matches the J_{SC} determined from the EQE data. The experiment was carried out at room temperature. A spatial open-circuit voltage image V_{xy} is obtained from the PL intensity image (I_{Hxy}) using the following equation [89, 66].

$$V_{xy} = V_T \cdot \ln\left(\frac{I_{Hxy} - B_{xy} \cdot I_H}{C_{xy}}\right) \tag{6.1}$$

Here V_T is the thermal voltage. I_H is the illumination intensity at which the PL image I_{Hxy} was taken. B_{xy} is a called a background calibration constant which accounts for the diffusion limited carriers. It is generally derived from an additional short-circuit current image. However, since B_{xy} is negligible in comparison to I_{Hxy}, it has been ignored for simplicity. C_{xy} is a calibration constant which can be expressed as:

$$C_{xy} = I_{Lxy} \cdot \exp\left(-\frac{V_{OC}}{V_T}\right) \tag{6.2}$$

Here I_{Lxy} is another open-circuit PL image at a lower illumination intensity (0.1 sun for this work). V_{OC} is the measured open-circuit voltage of the entire cell.

The high-speed spatially resolved EQE and reflectance measurements were performed with a customized Tau Science *FlashQE* system. The *FlashQE* system is an LED based EQE measurement system that utilizes unique modulation frequencies for each LED to enable full spectrum measurements in approximately one second. The LED's are focused onto a 4 mm spot size and measurements are performed as the light beam is moved across the cell with an automated *x-y* gantry. An integrating sphere is used to simultaneously measure reflectance at each location. In this case, the
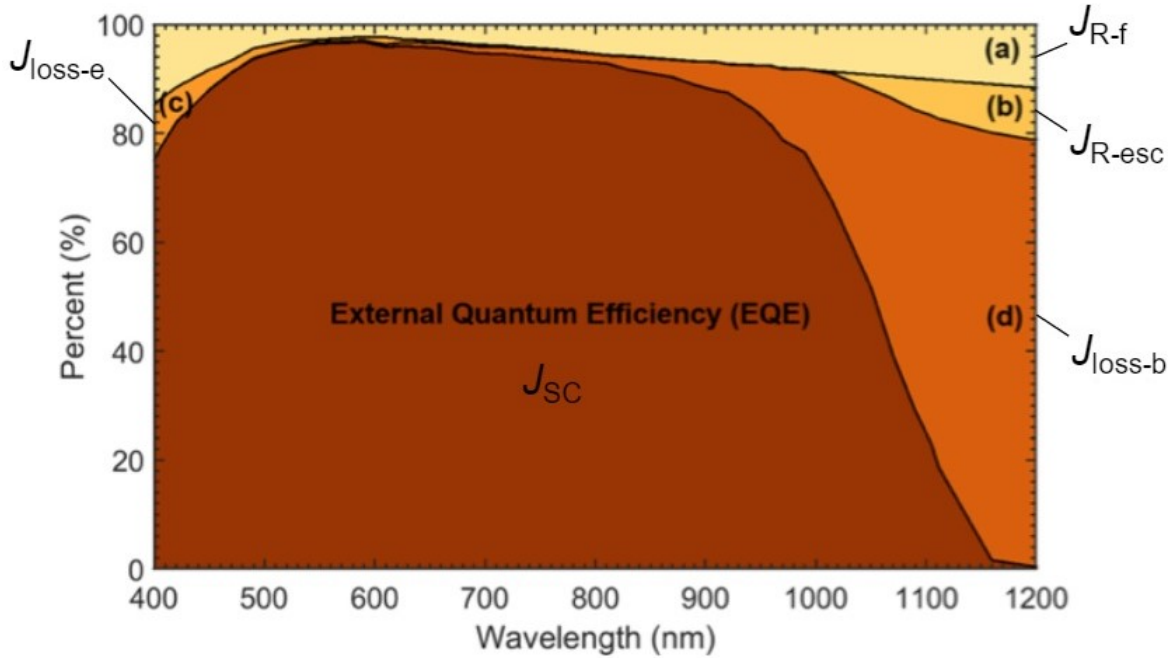
Figure 6.2: EQE and reflectance spectrum highlighting various J_{SC} losses (a) front surface reflectance ($J_{R\text{-}f}$), (b) escape reflectance ($J_{R\text{-}esc}$), (c) emitter loss ($J_{loss\text{-}e}$), and (d) bulk and rear surface loss ($J_{loss\text{-}b}$)

EQE and reflectance were measured on a 10x10 grid for each cell (*i.e.*, 100 points on each cell, equally spaced). Measurement at each of these points takes approximately 1 second [89]. The measurement locations were set to avoid the busbars and had the same amount of physical shading fraction from the metalization for all the measurements in a cell.

Different loss components of the short-circuit current density (J_{SC}) were extracted using the method outlined in [145], including: (a) front surface reflectance ($J_{R\text{-}f}$); (b) escape reflectance ($J_{R\text{-}esc}$) ; (c) parasitic optical absorption at the front (e.g., silver paste, anti-reflection coating) and recombination loss in the emitter ($J_{loss\text{-}e}$); and (d) recombination loss in the bulk and rear, or base, and parasitic absorption in the rear metal ($J_{loss\text{-}b}$), as depicted in figure 6.2.

Since the spot size is larger than the gridline spacing, it is not possible to measure only the active area of the cell. To account for this, the shading fraction due to the cell metallization is intentionally kept consistent for each measurement. Following the same method outlined in previous work [145], the reflectance and EQE data was adjusted to represent only the active area of the device as depicted in figure 6.2. Figure 6.2 shows that approximately 5% of the incident light gets reflected from the cell's front surface. As light enters into the cell, short wavelengths are efficiently absorbed, while a significant portion of the longer wavelength light may pass through the cell. The longer wavelength light may reflect from the rear side metallization and some of this light escapes the cell. This light is referred to as escape reflectance. Since escape reflectance occurs only in the longer wavelengths, the total reflection (sum of front and escape reflectance) increases rapidly after certain point in longer wavelength region (approximately 1020 nm in this study). The difference between total and front reflection provides escape reflectance. Absorption in the antireflection coating is assumed to be negligible, so the internal quantum efficiency (IQE) is calculated from the measured value of EQE, reflectance (R) and effective shading fraction of the gridlines (f_{eff}) [89],

$$IQE(\lambda) = \frac{EQE(\lambda)}{1 - R - f_{eff}} \tag{6.3}$$

In this work, 5% shading loss was calculated depending on the size of the light spot, the pitch and the width of the gridlines. Apart from the losses due to reflection and shading, additional losses also occur in the bulk, emitter and the rear surface of the cell due to parasitic absorption and nonradiative recombination at the defects, dislocations, grain boundaries, and poorly passivated surface regions. The emitter loss can be approximated using the model proposed by Fischer *et al.* [12] that can effectively replicate the impact of carrier generation and carrier collection within the emitter. Using this model, it becomes possible to separate the contribution of current loss that occurs from light absorbed within the emitter, from current loss occurring within the base of the cell. This approach was validated in previous work [145] and is represented by the following

87

equation;

$$IQE\left(\lambda\right) = \frac{1}{k}\exp\left(-\frac{W_d}{L_a\left(\lambda\right)}\right)\frac{1}{1+\frac{L_a(\lambda)}{L_{eff}}} \tag{6.4}$$

Here, L_{eff} is the effective diffusion length in the base, W_d is a hypothetical dead layer thickness, L_a is the absorption length, and k is a scaling factor which is independent of wavelength but depends on the experimental conditions. In addition to separating emitter vs. base loss components, this approach also leads to two valuable performance metrics; W_d and L_{eff}. L_{eff} is the base contribution to the effective diffusion length, that excludes any influence from the emitter or front surface of the device. W_d is a model parameter that does not represent any physical dimension within the device, but correlates to the recombination occurring within the diffused emitter and front surface of the device. Recombination due to the emitter dopant concentration is assumed to be the dominant factor driving this metric, as the front surface is effectively passivated with the SiN_X ARC.

Once the area above the EQE curve is assigned to one of the four loss mechanism shown in figure 6.2, an effective J_{sc} loss is calculated using the spectrally dependent mechanism and the standard AM 1.5 solar spectrum as the incident photon flux and the following equation[145];

$$J_{sc} = e\int_{365\ nm}^{1280\ nm} EQE\left(\lambda\right)\phi_{in}\left(\lambda\right)\ d\lambda \tag{6.5}$$

Here, e is the charge of an electron. The limits of integration are taken from 365 nm to 1280 nm based on the LED's within the *FlashQE* system that best approximated the typical absorption range of silicon solar cells.

The non-destructive cTLM measurements were performed using a BrightSpot Automation *ContactSpot-PRO* system, capable of three second takt times. The contact resistivity (ρ_c) and emitter sheet resistance (R_{sheet}) were extracted from the cTLM measurements using the technique in [70]. The ρ_c

and R_{sheet} of c-Si solar cells are traditionally measured using TLM measurements, wherein the test structures are created by isolating strips of a cell (e.g., laser scribe then cleave) or by fabricating special test structures within a wafer. The former can be applied to industrial cells, but is destructive, and the latter is non-destructive, but can't be used on industrial cells. The non-destructive technique used in this work relies on hiding circular TLM (cTLM) structures within the busbars of the cells and therefore doesn't result in any additional shading of the cell, so it can be used on finished solar cells [89]. The implementation of these structures within the busbars of solar cells has little to no impact on the solderability of the interconnects.

Dark lock-in thermography (DLIT) measurements were performed to spatially map power dissipation in selected cells. These were carried out by pulsing a 500 mV forward bias through the cells in a square wave at 2Hz and measuring the synchronized thermal emission signal with a cooled FLIR InSb infrared camera.

Table 6.1 lists all the parameters determined based on the characterization methods described above. The notations used here will be used throughout the following sections.

Results and Discussion

Losses and Process Variations from Cell to Cell

Illuminated *I-V*, Suns-V_{OC}, PL, high speed EQE + *R* (10 x 10 spots), and cTLM measurements were all carried out for the approximately 400 finished solar cells coming from the same production line. Doing all these measurements for a high volume cell group has provided an unique opportunity to investigate the causes behind losses in solar cells and the relationships among different performance parameters. Histograms of some of the various parameters determined from this combination of measurements are shown in figure 6.3. The efficiency, J_{SC}, V_{OC}, and FF of the

89

Table 6.1: Parameter Overview

Measured Parameters	Symbol	Name of the Measurement
Short circuit current	I_{SC}	Illuminated I-V
Open circuit voltage	V_{OC}	Illuminated I-V
Global short circuit current density	J_{SC}	Illuminated I-V
Global series resistance	R_S	Illuminated I-V, Suns-V_{OC}
Dark saturation current density (ideal)	J_{01}	Suns-V_{OC}
Dark saturation current density (non-ideal)	J_{02}	Suns-V_{OC}
Effective carrier lifetime	τ_{eff}	Suns-V_{OC}
Bulk resistivity	ρ_{bulk}	Suns-V_{OC}
Sheet resistance	R_{sheet}	cTLM
Contact resistivity	ρ_c	cTLM
Spatially resolved voltage	V_{xy}	PL imaging
Spatially resolved effective diffusion length	L_{eff}	FlashQE
Spatially resolved current density	J_{SC-xy}	FlashQE
Spatially resolved current loss in emitter	J_{loss-e}	FlashQE
Spatially resolved current loss due to front reflectance	J_{R-f}	FlashQE
Spatially resolved current loss due to escape reflectance	J_{R-esc}	FlashQE
Spatially resolved current loss in the bulk & rear side	J_{loss-b}	FlashQE

cells were obtained from illuminated I-V measurements. Suns-V_{OC} measurements provided the effective carrier lifetime (τ_{eff}), R_S, and the dark saturation current densities, J_{01} and J_{02}. The EQE and R measurement allowed the calculation of current loss due to the front reflectance (J_{R-f}), escape reflectance (J_{R-esc}), and losses in the emitter (J_{loss-e}) and base and rear side of the cell (J_{loss-b}). The PL measurements provided the images of open-circuit voltage (V_{xy}), and the cTLM measurements provided the sheet resistance (R_{sheet}) and contact resistivity (ρ_c).

The distributions of the parameters can help quantify variance due to both incoming materials (e.g., wafer quality) and specific unit processes (e.g., texturing, phosphorus diffusion, SiN_x deposition, metallization), further providing insights into what loss mechanisms limit cell performance. The results can help prioritize efforts to optimize performance of the production line and be used to actively control unit processes. For example, histograms of the loss parameters determined from the
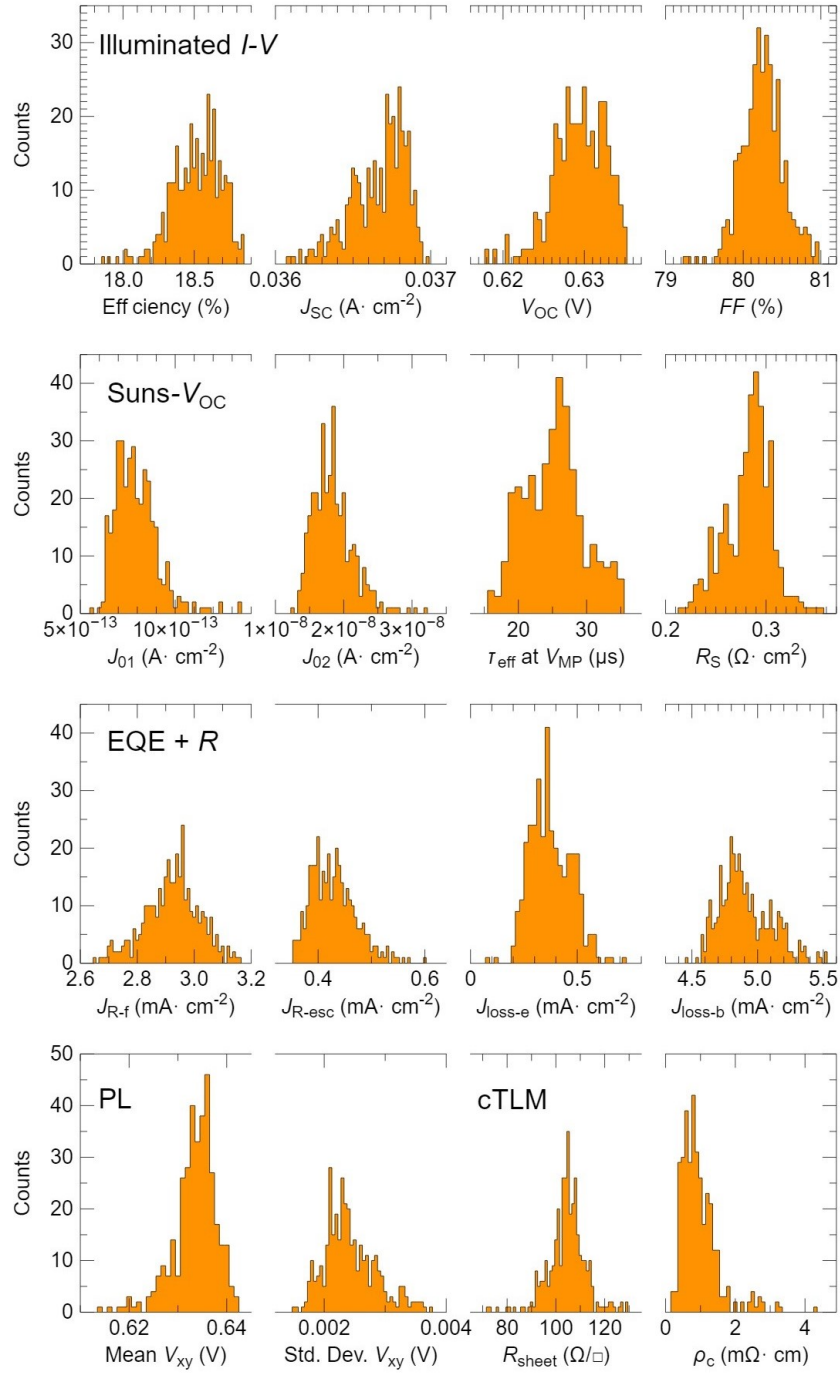
Figure 6.3: Histograms of the various parameters calculated from the illuminated *I-V*, Suns-V_{OC}, PL, high speed EQE + *R*, and cTLM measurements. Note, R_S is determined from the difference between the *I-V* and Suns-V_{OC} curves.

EQE + R data show that loss in the bulk/rear of the cell (i.e., $J_{\text{loss-b}}$) is the primary limiting factor for J_{SC}, followed by front surface reflectance (i.e., $J_{\text{R-f}}$). Regarding the shape of the histograms, a skewed Gaussian distribution is observed for efficiency, J_{SC}, V_{OC}, J_{01}, J_{02}, $_{\text{R-esc}}$, $J_{\text{loss-b}}$, V_{xy}, and ρ_c. In all cases, the tail of the histrogram for these parameters is located on the side representing poor performance (e.g., low values of V_{OC}, high values of J_{01}). The histograms of FF, τ_{eff}, R_{S}, $J_{\text{loss-e}}$, and R_{sheet} appear to have a normal Gaussian distribution.

In a practical sense, efficiency is the most important parameter of a solar cell. In figure 6.4, the efficiency values from the *I-V* measurements were compared with parameters obtained from Suns-V_{OC}, cTLM, PL and *FlashQE* measurements for the whole group of cells. A few outliers were excluded from this analysis, including broken cells and cells with severe shunting issues. Figure 6.4(a) shows a strong linear relationship between efficiency and J_{01}, which represents the dark saturation current density of the diode with a unity ideality factor. A significantly weaker relationship is found between decreasing efficiency and J_{02} loss, the dark saturation current density with an ideality factor of two that is commonly attributed to recombination within the depletion region. The steeper slope and stronger correlation between efficiency and J_{01} points to the fact that quality of the bulk and the surface passivation has the strongest impact on efficiency for these cells. An overall increasing trend of the efficiency was also shown to very weakly correlate with increase in R_{S}. This is because R_{S} for these cells is driven primarily by doping in the emitter and, to a lesser extent, the background doping concentration in the bulk of the wafer. Higher doping levels reduce the R_{S} losses, but they increase the nonradiative recombination and therefore J_{01}. Since J_{01} has a much stronger influence on efficiency than R_{S}, the result is positive correlation between R_{S} and efficiency.

Interestingly, figure 6.4(b) shows that efficiency is positively correlated with average J_{sc} and negatively correlated with the spatial standard deviation of J_{SC}. In monocrystalline silicon Al-BSF cells, rear surface recombination is almost always the limiting the factor. For multicrystalline sil-
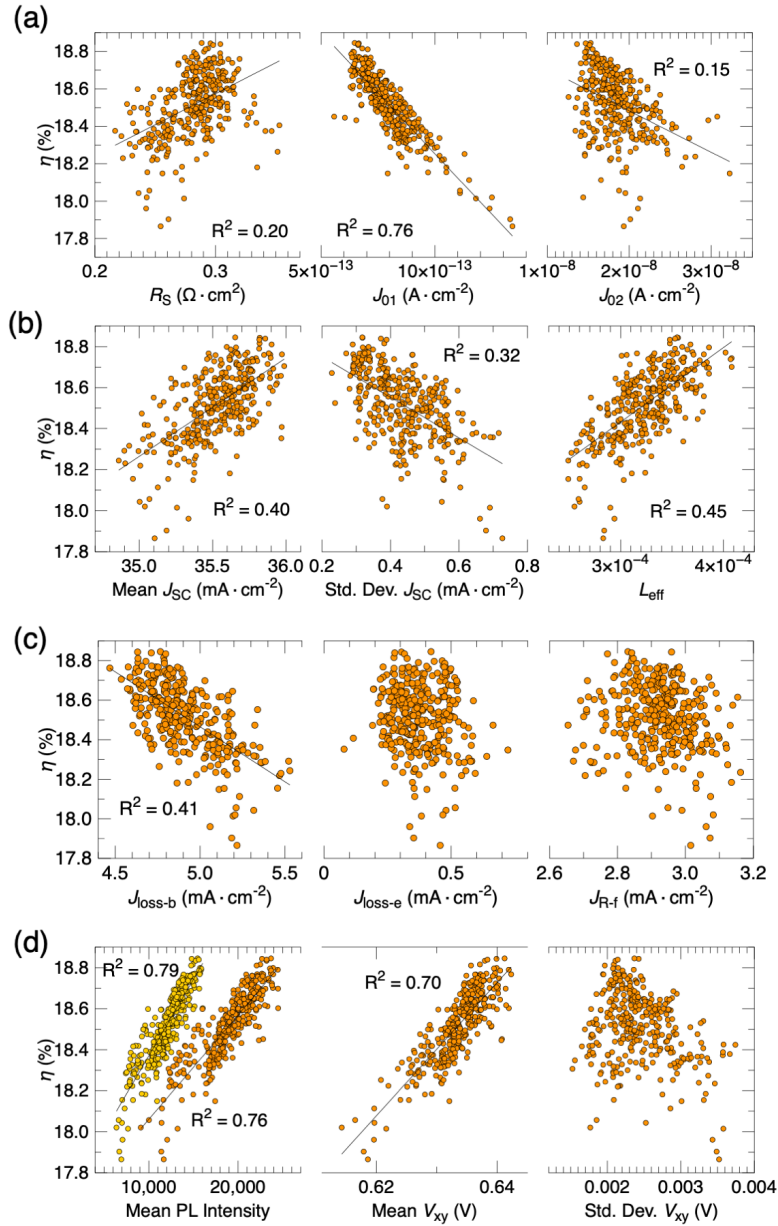
Figure 6.4: Correlations between the cell efficiency and various parameters, including: (a) R_S, J_{01}, and J_{02} measured using I-V and Suns-V_{OC}; (b) the mean J_{SC}, within-cell standard deviation of J_{SC}, and L_{eff} measured with EQE + R; (c) J_{loss-b}, J_{loss-e}, and J_{R-f}; and (d) the mean PL intensity at 0.1 sun (yellow) and 1 sun (orange), mean V_{xy}, and within-wafer standard deviation of V_{xy} measured using PL imaging. A few outliers are excluded, i.e., broken cells, cells with cracks and severe shunts.

93

icon Al-BSF cells, like the ones measured in this work, either the bulk carrier lifetime or rear surface recombination can limit cell performance. The bulk carrier lifetime normally varies more over the surface of the cell than rear surface recombination, which is why the crystal structure is observed so clearly in PL and V_{OC} images. Cells with a large spatial variation in bulk wafer quality result in a large spatial standard deviation of J_{SC}, and because of the negative correlation between efficiency and the spatial standard deviation of J_{SC}, the bulk wafer quality appears to limit the cell performance in some cases. The role of the bulk wafer quality and/or rear surface recombination is further confirmed by the correlation between efficiency and the the effective diffusion length of the base (i.e., L_{eff}) derived from the EQE data, as well as the correlation between efficiency and J_{loss-b} shown in figure 6.4(c). Again, it is hard to separate the influence of the wafer bulk carrier lifetime from rear surface recombination since L_{eff} and J_{loss-b} include both recombination mechanisms. No such correlations are observed between J_{loss-e} or the reflectance losses shown in figure 6.4(c).

Figure 6.4(d) shows a significantly stronger correlation between cell efficiency and V_{xy} obtained from PL than that of J_{SC}. The strong correlation of efficiency with V_{xy} makes sense due to the strong relationships between J_{01}, V_{OC}, and efficiency. Again, for these cells efficiency is limited by recombination in the bulk and rear, and cells with high bulk/rear recombination will have a high J_{01}, low V_{OC}, and therefore a low V_{xy}.

Another method of analyzing the data is to evaluate correlations between the numerous parameters measured with these different techniques. For example, figure 6.5(a) shows which region of the device is limiting the overall τ_{eff} of the cells. Here, the current loss in the bulk and rear of the cell (i.e., J_{loss-b}) correlate to τ_{eff}, whereas the losses in the emitter (i.e., J_{loss-e}) do not. Additionally, L_{eff} has a strong correlation to τ_{eff}, further indicating that that recombination in the bulk and rear of the cell is limiting τ_{eff} and not recombination in the emitter. This makes sense considering these are multi Al-BSF cells, which are known to have both a low bulk carrier lifetime and high recombination at the rear surface since the entire rear side has a metal/semiconductor interface.

In figure 6.5(b), Suns-V_{OC} and cTLM measurements are used to separate three components of R_S, including R_{sheet} (from cTLM), ρ_b (from Suns-V_{OC}), and ρ_c (from cTLM). The strength of the correlations indicates that the R_{sheet} of the emitter has the strongest influence on the overall R_S, followed by the ρ_b of the wafer next. The ρ_c of these specific cells is too low to significantly affect the overall R_S. Despite the fact that R_S isn't the limiting factor for cell efficiency, in solar cell manufacturing, tracking and limiting all losses throughout cell manufacturing is critical to increase the overall efficiency of the production line. Again, these parameters can be used to control individual processes, like phosphorus diffusion (R_{sheet}) and contact firing (ρ_c) or track variations in the doping of the incoming wafers (ρ_b), allowing a manufacturing production team to minimize the overall R_S and when things go wrong in production, allows them to quickly diagnose and fix the problem.

A correlation between J_{loss-e} and the emitter R_{sheet} is observed in figure 6.5(c). Another similar correlation is noticed between R_{sheet} and dead layer thickness (i.e., W_d). The dead layer thickness is a model parameter that correlates with the dopant concentration in the emitter of the cell [12]. Both J_{loss-e} and dead layer thickness were derived from the *FlashQE* data and account for losses in the emitter, whereas R_{sheet} was measured using cTLM with the *ContactSpot-PRO*. The current losses from the emitter and R_{sheet} are both heavily dependent on the level of doping within the emitter, however they influence the overall cell efficiency in opposite directions. From a recombination loss perspective, less doping within the emitter will result in less nonradiative recombination and a smaller J_{loss-e}. However, less doping results in a higher R_{sheet}, adding resistive losses as electrons travel laterally within the emitter to the front contacts of the cell. By measuring these recombination and resistive parameters independently, the phosphorus doping profile can optimized to minimize both the recombination and resistive losses due to the emitter.

Another interesting correlation observed in this dataset in figure 6.5(d) is a relatively strong correlation between the J_{02} value measured by Suns-V_{OC}, which is a measure of the non-ideal recombi-
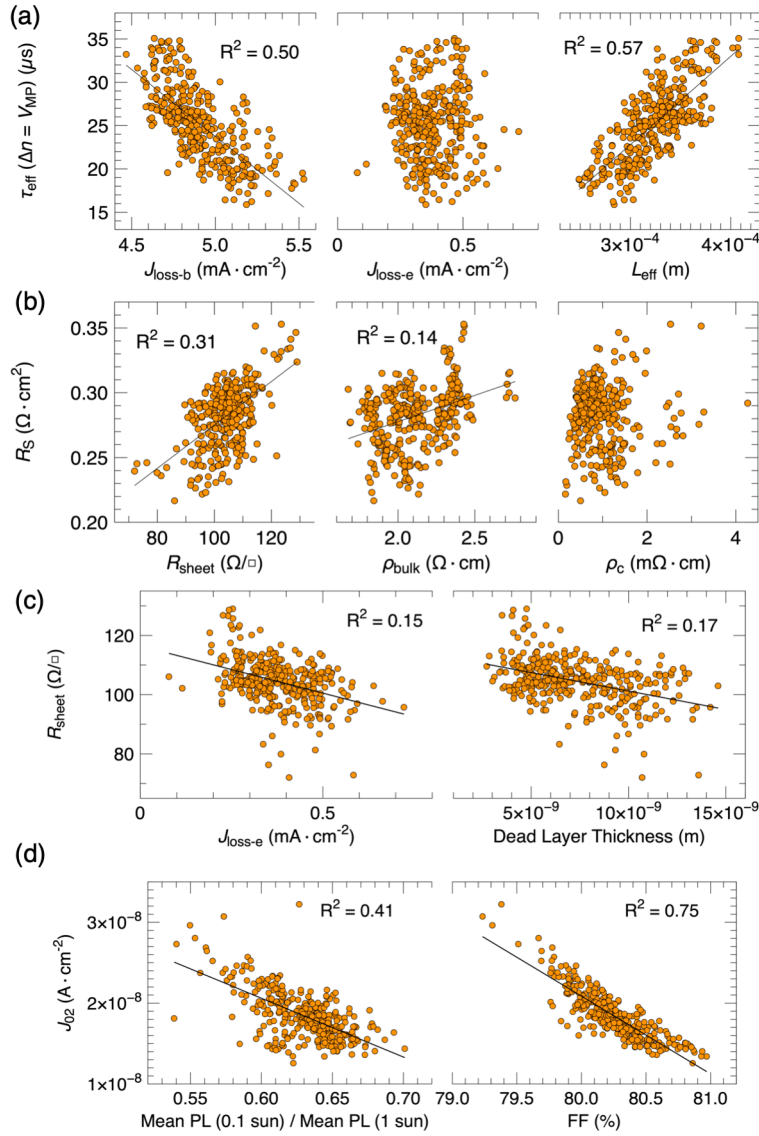
Figure 6.5: (a) Correlations between τ_{eff} at V_{MP}, determined from Suns-V_{OC}, and $J_{\mathrm{loss\text{-}b}}$, $J_{\mathrm{loss\text{-}e}}$, and L_{eff}, all determined from the EQE data. (b) Correlations between R_{S}, determined from the difference in the *I-V* and Suns-V_{OC} curves, and R_{sheet} (cTLM), ρ_{b} (Suns-V_{OC}), and ρ_{c} (cTLM). (c) Correlations between R_{sheet}, determined from cTLM, and both $J_{\mathrm{loss\text{-}e}}$ and the dead layer thickness, both determined from the EQE data. (d) Correlation between J_{02} (Suns-V_{OC}) and the ratio of the mean PL intensities at low irradiance (0.1 sun) divided by the mean PL at high irradiance (1 sun), as well as the correlation between J_{02} (Suns-V_{OC}) and *FF* (illuminated *I-V*). A few outliers are excluded, i.e., broken cells, cells with cracks and severe shunts.

nation of the cell ($n = 2$), and the ratio of the mean PL intensity at low irradiance (0.1 sun) and high irradiance (1 sun). Non-ideal recombination can be observed on wafers and cells when the effective carrier lifetime, and therefore the excess carrier density, shows a strong injection dependence. Since the PL intensity is dependent on excess carrier density, a simple ratio between PL at low and high irradiance levels can be used as a metric for this non-ideal recombination. This non-ideal recombination can be due to recombination in the depletion region (e.g., edge recombination [53], recombination at grain boundaries or dislocations [20]) and poor field effect passivation at the silicon surface [9], all of which are dependent on the manufacturing materials and processes used to produce the cells. The influence of this non-ideal recombination on the actual solar cell performance is observed in figure 6.5(d) with the very strong correlation between J_{02} and *FF*.

Spatially-Resolved Losses for Individual Cells

Table 6.2 lists the performance parameters of three different cells, a good cell, a moderate cell, and a poorly performing cell. The good cell (18.7%) has higher current and voltage than the other two, though the fill factor is slightly lower than of the moderate cell. The moderate cell with 17.9% efficiency has both lower current and voltage than the higher efficiency cell. Surprisingly, the poorly performing cell (16.4% efficiency) has higher current and voltage than the moderate cell, with a significantly lower FF being the main reason for efficiency loss. In the case of this specific cell, the drop in FF is due to the presence of a severe shunt.

Table 6.2: Measured performance parameters of the three cells shown in figure 6.6

Efficiency (%)	J_{SC} (mA/cm^2)	V_{OC} (V)	FF (%)	J_{SC-xy} (mA/cm^2)	J_{R-f} (mA/cm^2)	J_{R-esc} (mA/cm^2)	J_{loss-e} (mA/cm^2)	J_{loss-b} (mA/cm^2)	J_{01} (fA/cm^2)	J_{02} (nA/cm^2)	R_S (mΩ)	ρ_{bulk} (Ω.cm)
18.70	36.91	0.633	80.05	35.98	2.98	0.41	0.22	4.53	680	18.3	1.307	2.39
17.91	36.05	0.618	80.32	35.05	3.02	0.40	0.49	5.21	1170	22.1	0.957	2.18
16.37	36.29	0.619	72.82	24.08	2.85	0.43	4.66	13.05	868	38.0	-0.3	2.23

In order to investigate how spatial variations in cell defects correlate to the overall cell efficiencies
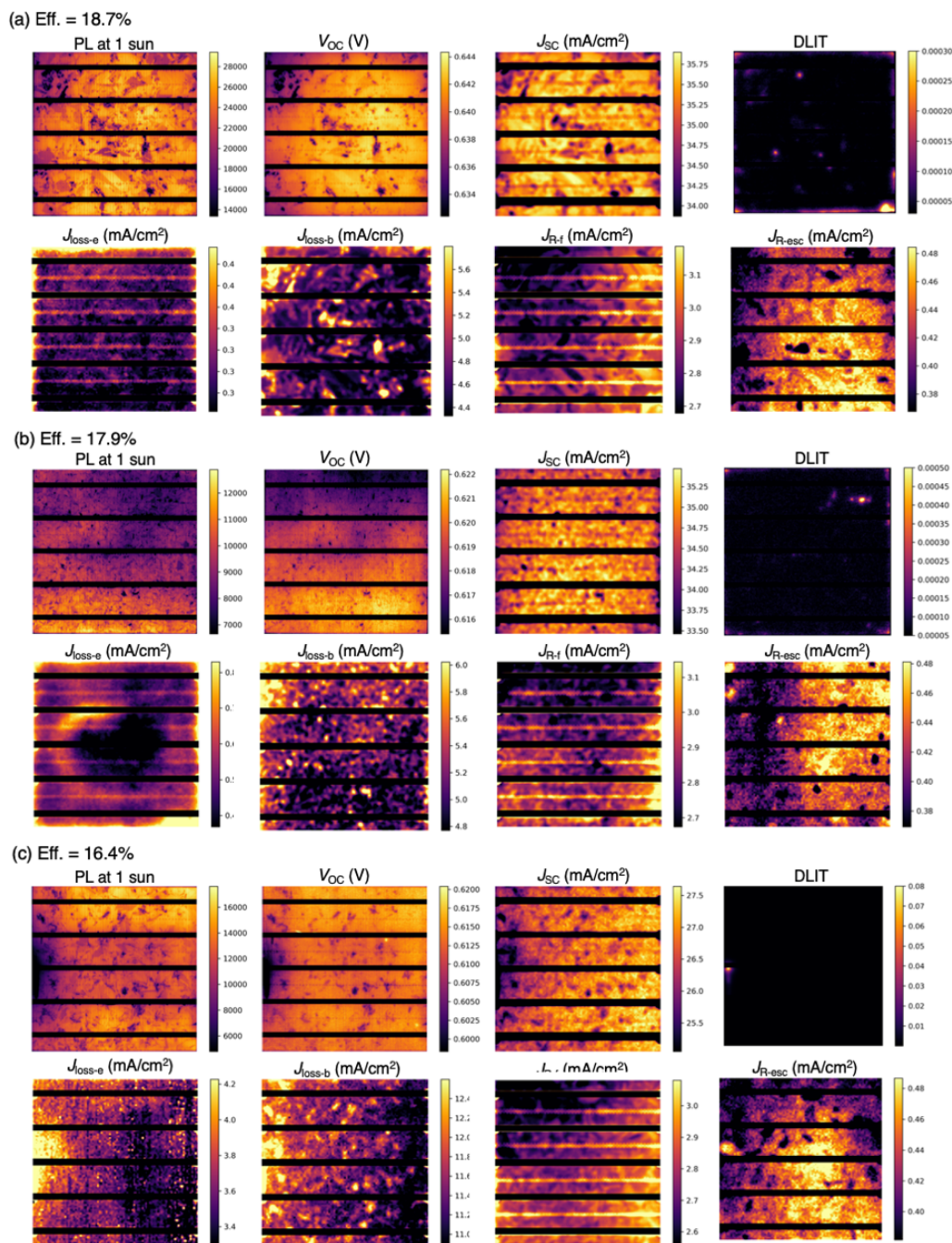
Figure 6.6: PL, spatially-resolved V_{OC}, spatially-resolved J_{SC}, DLIT (at 500 mV, 2Hz) and current loss analysis images (obtained from point by point *EQE+R* measurement) of three different cells, a good cell (18.4%), a moderate cell (17.9%), and a poorly performing cell (16.4%). Note, the scales of the images are different for better contrast.

for the cells listed in table 6.2, high resolution EQE and R measurements (97 x 97 point measurement), PL imaging, and dark lock-in thermography (DLIT) [25] were performed. Figure 6.6 shows the resulting images of the uncalibrated PL signal, V_{OC} (from PL), J_{SC} (from EQE), and the total power dissipation (from DLIT). For all three cells, the PL, V_{OC}, and J_{SC} images show similar patterns due to the known reciprocity between cell efficiency and radiative recombination [137]. The DLIT images show lossy regions as bright instead of dark, as the camera detects heat generation (i.e., dissipated power) in regions acting as current sinks through either shunting or enhanced carrier recombination. DLIT can also pick heat dissipated due to resistive losses in the cell.

The poorly performing cell has a dark region near the left edge in all the images (bright in DLIT), which likely indicates a strong shunt in this region. The discrepancy between the current density from I-V measurements (36.3 mA/cm^2) and the average current density from QE measurement (24.1 mA/cm^2) in table 6.2 occurred because of the shunt. The QE measurement is performed point-by-point and at lower illumination intensities than the illuminated I-V measurement performed at STC. In the locations featuring the shunt, almost all the photogenerated current funnels through shunting. The neighbouring locations may also be affected because whenever those locations generate some current, part of it leaks to the shunt through the gridlines. The presence of a shunt is not reflected so much in the J_{SC} value coming from the I-V measurement, although it is observed in the slope of the I-V and pseudo I-V curves near short-circuit. The reason it does not affect J_{SC} as much in the I-V measurement is that when illuminating the whole cell at a time and taking only one measurement, the shunt saturates, preventing further leaking.

Further image processing was carried out to find the exact location of the shunt. Figure 6.7 depicts a zoomed in view of the shunt location in the poorly performing cell, coming from different imaging methods. The images suggest that the shunt is actually under a gridline near the busbar, where the DLIT image provides the most accurate location of the shunt. A possible reason for this shunt is, at the time of screen printing, the silver paste may have etched through the p-n junction and touched

99

Eff. = 16.4%: Open-Circuit PL at 1 sun

Inverse PL   Inverse V_{OC} Inverse J_{SC} DLIT
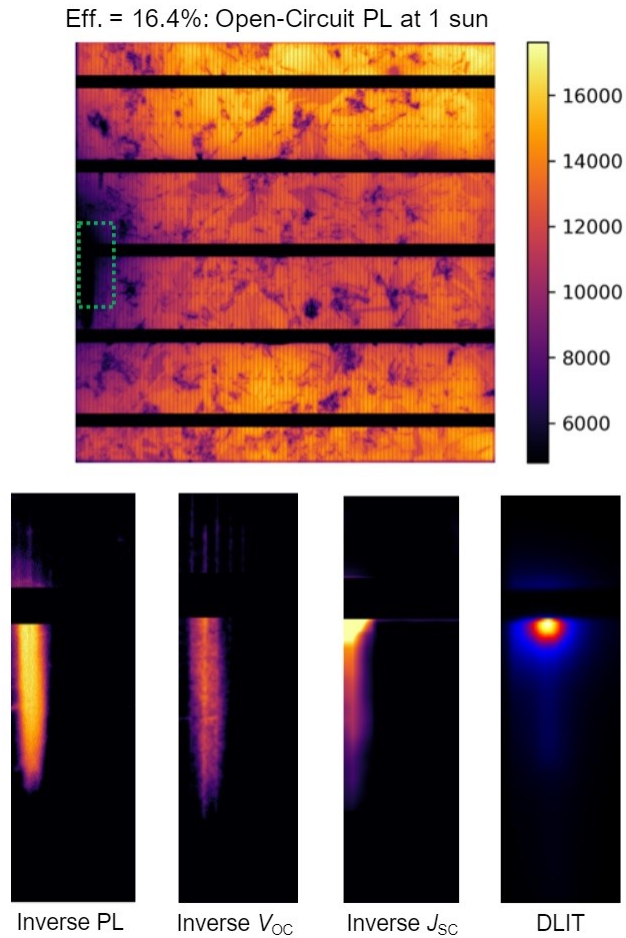
Figure 6.7: A view of the severe shunt for the poorly performing cell (16.4%), including the in PL, V_{OC}, J_{SC} and DLIT images.

the base. Although the presence of a shunt immensely deteriorated the performance of the cell, it occurred only for this one, out of the 400 cells investigated.

Current loss analysis was also carried out using the high-resolution EQE and R data for the three cells. These images in figure 6.6 provide an idea of the current loss distribution over the surface of the cell. The scale on the current loss images shows that most of the losses occur in the bulk of the cell which is related to the crystalline quality of the cell. Looking at the $J_{\text{loss-e}}$ images, we

notice that this type of loss is more pronounced in the edges and corners of the cells, which likely occurred because of the higher levels of doping in these regions and therefore higher nonradiative recombination.

Horizontal lines with high loss values are noticed in the middle of two busbars both in the $J_{\text{loss-e}}$ and $J_{\text{R-f}}$ images. These are the regions where the metallic gridlines are connected, visible in figure 6.1(c). Since they have more shading fraction than other regions, they show up in the $J_{\text{R-f}}$ images. It is well known that the front metal contacts cause high recombination compared to the SiN_x passivated regions, so it makes sense that these regions would also suffer from higher levels of recombination at the front of the cell. Although the shunt appeared in the emitter and base loss images, it is absent in the front and escape-reflectance images.

Conclusion

In this work, a comprehensive series of measurements was performed on approximately 400 cells, including illuminated I-V, Suns-V_{OC}, quantum efficiency, reflectance spectroscopy, PL imaging, and non-destructive TLM. The distributions of a wide variety of parameters was presented, and correlations between parameters were explored. Multiple methods confirm that these cells are limited by recombination losses in the bulk and at the rear surface of the cells, including the strong negative correlation between cell efficiency (I-V) and J_{01} (Suns-V_{OC}) and $J_{\text{loss-b}}$ (*FlashQE*), and strong positive correlation between efficiency and τ_{eff} (Suns-V_{OC}) and L_{eff} (*FlashQE*). Although R_S (Suns-V_{OC}) is not the limiting factor in these cells, the resistive losses can still be tracked individually, and in this case R_S is primarily influenced by R_{sheet} (cTLM) of the emitter, followed by the bulk resistivity of the wafer (Suns-V_{OC}). No correlation is found between R_S and ρ_c (cTLM); it's too low for these cells. Interesting relationships were observed across the various techniques. There is a strong correlation between mean J_{SC} (*FlashQE*), mean PL intensity (PL), and cell efficiency, which is ex-

pected considering these cells are limited by bulk and rear recombination. The τ_{eff} (Suns-V_{OC}) is strongly correlated with $J_{\text{loss-b}}$ and L_{eff} (*FlashQE*), but shows no correlation with $J_{\text{loss-e}}$ (*FlashQE*). The $J_{\text{loss-e}}$ is correlated with R_{sheet} (cTLM), which confirms that heavier doping will both result in higher recombination losses within the emitter and a lower R_{sheet}.

A subset of additional measurements was performed on three individual cells with varying levels of performance (i.e., good, moderate, bad), including spatially-resolved quantum efficiency and reflectance measurements and dark lock-in thermography. From these measurements, the location and severity of a shunt were identified as the primary factor limiting the efficiency of the poorly performing cell. These high-resolution imaging techniques can be very useful to gain more insight into the root case of defective cells taken from a production line.

Access to the loss parameters obtained from these measurements was shown to provide useful insight into mechanisms driving device performance in terms of optical, resistive and recombination losses. This approach could be used for process control in a manufacturing environment, where specific defects can be identified, classified, and their impact quantified. Additionally, many of these parameters can be tied back to incoming material quality issues (e.g., poor bulk carrier lifetime, nonuniform wafer doping) or to individual unit processes (e.g., texturing, phosphorus diffusion, silicon nitride deposition, metallization), allowing the data to be used directly for process control in manufacturing or to prioritize cell efficiency optimization efforts.

CHAPTER 7: LOSS MITIGATION: SELF-ASSEMBLED MULTIFUNCTIONAL NANOSTRUCTURES FOR SURFACE PASSIVATION AND PHOTON MANAGEMENT IN SILICON PHOTOVOLTAICS

This work reports the fabrication and characterization of multifunctional, nanostructured passivation layers formed using a self-assembly process that provide both surface passivation and improved light trapping in crystalline silicon photovoltaic (PV) cells. Scalable block copolymer self-assembly and vapor phase infiltration processes are used to form arrays of aluminum oxide nanostructures (Al_2O_3) on crystalline silicon without substrate etching. The Al_2O_3 nanostructures are characterized using scanning electron microscopy (SEM), transmission electron microscopy (TEM), and spectroscopic ellipsometry. Injection-level dependent photoconductance measurements are used to determine the effective carrier lifetime of the samples to confirm the nanostructures successfully passivate the Si surface. Finite element method simulations and reflectance measurement show that the nanostructures increase the internal rear reflectance of the PV cell by suppressing the parasitic optical losses in the metal contact. An optimized morphology of the structures is identified for their potential use in PV cells as multifunctional materials providing surface passivation, photon management, and carrier transport pathways.

Introduction

With silicon solar cell efficiency values approaching their theoretical limit, the elimination of remaining energy conversion losses becomes more challenging. Energy conversion losses [89, 90] commonly take the form of either optical losses (e.g., reflection, parasitic optical absorption, quantum defect) or electrical losses (e.g., carrier recombination losses, carrier selectivity losses, resistive losses). A persistent obstacle to this goal is the fact that many approaches that help lower one form of loss tend to increase another. Metal contact grids are required to deliver current to the external circuit with minimal voltage drop, limiting the resistive losses of solar cells. However, having metal in direct contact with silicon leads to increased recombination loss, and when the metal grid is placed on the front of the cell it blocks light from getting into the absorber (i.e., front reflection loss). Also, when placed on the rear side of the cell, it causes parasitic optical loss [36, 85, 84, 178]. The current record holding silicon solar cell (26.7% efficient under standard test conditions) uses a passivating, carrier-selective contact structure to limit recombination and an all rear contacted configuration to avoid the optical shading of the front contact grid [171]. However, this cell architecture is very complex to manufacture, and it is unclear if it will gain significant market share.

Currently, passivated emitter and rear contact (PERC) cells [15, 68, 14] are the primary type of photovoltaic (PV) cell manufactured around the world [136]. These cells feature dielectric thin films covering most of the front and rear surfaces, along with local metal contacts (i.e., partially covering the surface) to extract carriers and deliver current to the external circuit. These dielectric thin films are multifunctional, in that they both passivate the surfaces and help lower optical losses. On the front side of the cell, the thin film(s) act as single or multi-layer antireflection coatings (ARC) [7]; on the rear side of the cell, the thin film(s) help increase the internal rear reflectance, thereby assisting light trapping for photons with energies near the band edge (i.e., 900-1280 nm)

[127]. Together, the mitigation of surface recombination and optical losses help maximize both the short-circuit current density (J_{SC}) and the open-circuit voltage (V_{OC}) of c-Si PV cells [111]. Since the dielectric films are insulating, local contacts are required to extract charge carriers. For the rear contacts of PERC cells, these are formed using laser ablation to remove the dielectric and then screen-printing Al contacts to form a local aluminum-silicon (Al-Si) alloy back surface field (BSF) [135, 120]. This approach of forming local contacts has several limitations. Firstly, it damages the silicon surface. With an Al contact that can be fired at a high temperature, this issue is somewhat avoided by the formation of a local Al-BSF. However, this is not compatible with other contact materials, including various passivating, carrier-selective contact technologies under development [125, 164]. Another issue is the fact that the combination of laser ablation and screen-printing leads to a typical contact pitch (i.e., distance between contacts) on the order of mm. This introduces spreading resistance as carriers must travel further through the base of the wafer which in turn requires higher levels of doping in the wafer.

Alternative approaches to forming passivated surfaces with nanoscale local contacts have been demonstrated, but these approaches typically rely on random processes that limit the ability to engineer their optical and electrical properties. One such example was implemented using blistering in aluminum oxide (Al_2O_3) passivation layers produced by atomic layer deposition (ALD) [162]; blistering occurs through the gaseous desorption in the Al_2O_3 layer upon thermal treatments above a critical temperature. Another example is the POLO (polycrystalline silicon on oxide) process developed recently, which relies on the breakdown of the oxide layer at very high temperatures. In this process polycrystalline Si (poly-Si) penetrates the passivating oxide layer, resulting in the formation of randomly distributed pinhole contacts [73, 130, 58, 50]. In this work, we fabricate the ordered arrays of Al_2O_3 nanostructures with various shapes (lamellae, nanoholes, nanopillars) using the self-assembly of diblock copolymers without any lithography or substrate etching. The patterns and the sizes of the nanostructures can be controlled by chemical composition of the ma-

terials, spin coating speed and annealing temperature in the synthesis process [41, 34].

The simultaneous need for high-quality passivation, low optical loss, and small spreading resistance suggests that optimal cell performance may be achieved using a densely spaced array of local metal contacts, surrounded by passivating dielectric material. In order to achieve such high-density metal contacts without the need for high resolution lithography, here we utilize a combination of self-assembly, atomic layer deposition, and metal thermal evaporation to fabricate nanostructured metal-dielectric networks that function simultaneously as a metallic contact, a high-quality optical reflector, and a passivating surface. These structures also exhibit great potential for engineering carrier transport properties.

Formation of Nanostructured Passivation Layers using Self-Assembly

The PV research community has developed numerous passivation materials [18], but only a few have been adopted by industry. Hydrogenated amorphous silicon nitride (SiN_x or a-SiN_x:H) is one such material that provides surface passivation [6, 8, 40] and can act as an excellent ARC. Thermally grown silicon oxide (SiO_2) has also been used for many years, more so in research environments than in industry. More recently, Al_2O_3 has emerged as a preferred passivation material for solar cells [40, 82, 83, 96] for several reasons. Firstly, Al_2O_3 was shown to provide very low interface defect density and excellent field-effect passivation by negative fixed charge [45]. Secondly, high-quality and ultrathin Al_2O_3 can be easily fabricated using atomic layer deposition (ALD) today. Thirdly, it demonstrates very good stability during processing [40] and can be used to passivate both the front and the rear side of the cell [160].

Ordered arrays of Al_2O_3 nanostructures with various shapes (lamellae, nanoholes, nanopillars) are fabricated using the self-assembly of diblock copolymers without any lithography or substrate
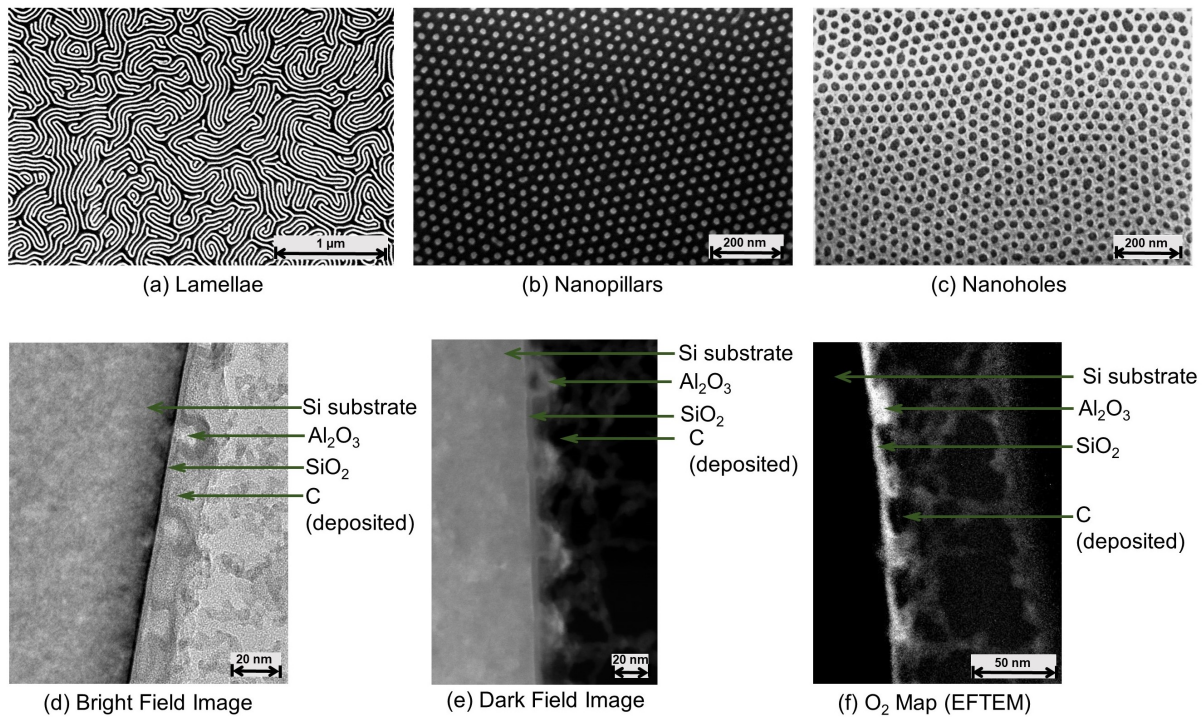
Figure 7.1: (a)-(c): Scanning electron microscopy image of three different nanostructures (the white regions are Al_2O_3) grown using block copolymer self assembly assisted atomic layer deposition. (d)-(f): Transmission electron microscopy images (cross-section) of the Al_2O_3 lamellae nanostructure grown on Si substrate. The sample was carbon coated to protect it from damage at the time of imaging (d) Bright field image (e) Dark field image (f) O_2 map using energy filtered transmission electron microscopy.

etching. This process relies on the selective vapor phase infiltration of precursors into one of the polymer blocks during the Al_2O_3 ALD process (details in the Experimental Section). Scanning electron microscopy (SEM), transmission electron microscopy (TEM) and spectroscopic ellipsometry measurements were carried out to characterize the morphology of these structures. The SEM images of the nanostructures are shown in Figure 7.1(a)-(c). The width of the lamellae (Figure 7.1(a)) was found to be approximately 15 nm. Both the Al_2O_3 nanopillars (Figure 7.1(b)) and nanoholes (Figure 7.1(c)) self-assemble with hexagonal ordering. The diameter of the pillars and their center to center distance were 16 nm and 36 nm respectively. Similarly, the diameter of the

holes and their center to center distance were 17 nm and 38 nm respectively. The area fractions of Al_2O_3 in the lamellae, nanopillar and nanohole patterns are 48%, 28% and 67% respectively.

TEM imaging was conducted at the Al_2O_3 nanostructure and Si interface. Figure 7.1(d)-(f) illustrates the bright field image, dark field image and the EFTEM (energy-filtered TEM) image of the interface where Si is on the left side. A periodic structure indicative of the cross-section of different lamellae is readily apparent. The width of the lamellae is found to be approximately 20 nm which matches with the value from SEM images; the height is approximately 10 nm. The right side of the images is carbon which is deposited to protect the sample from damage at the time of imaging.

Ellipsometry was also conducted to complement the morphological characterization by SEM and TEM. To fit the measured data with the material model, Bruggeman approximation and the area fraction obtained from SEM are used. The presence of an SiO_2 layer was also assumed. The height of the structures were recorded for the best fit cases. The SiO_2 layer thickness was approximately 2.8 nm for all the samples. The height of the lamellae, pillar and hole structures, as obtained from the fit were approximately 9.2, 10.7 and 13.0 nm, respectively. The morphological data of all the structures are summarized in Table 7.1.

The Al_2O_3 nanostructured passivation layers were formed on both sides of a Si wafer. Then, photoconductance-based effective carrier lifetime measurements were carried out to assess the surface passivation quality achieved with each of these structures. For an unpassivated sample, the lifetime value was below the measurement threshold (5 μs). Table 7.1 lists the lifetime obtained with the nanostructures. In the cases of surface passivation with lamellae, nanopillars and nanoholes, the lifetime values were 115, 119, and 147 μs respectively. The corresponding dark saturation current density (J_0) values are also listed in Table 7.1.

Table 7.1: Morphology of the Nanostructures and Their Surface Passivation Properties

Nanostructure	Al_2O_3 area fraction[a]	Al_2O_3 height (nm)[b]	Lifetime (μs)[c]	J_0 (A/cm^2)[c]
Lamellae	48%	9.2±0.06	115	$2.55x10^{-12}$
Nanopillars	28%	10.7±0.01	119	$2.18x10^{-12}$
Nanoholes	67%	13.0±0.01	147	$1.73x10^{-12}$

[a]SEM image, [b]ellipsometer measurement (with effective medium approx.), [c]photoconductance measurement

Photon Management

Silicon is an indirect bandgap material and it cannot absorb all the incident photons using practical cell thicknesses, especially when the wavelengths approach the band edge. This motivates the use of an efficient photon management technique on the rear side to provide the cell with additional opportunities to absorb photons, thus increasing the overall J_{SC}. A rear side with a high internal reflectance is needed to provide the cell with additional chance(s) for absorption. In the presence of a thick rear metal contact, the transmission is zero; therefore what fraction of the photons incident to the rear side are reflected back to silicon is dictated by the absorption loss in the metal. Unfortunately, a significant portion of these incident photons are lost through parasitic absorption loss in the metal [36, 86], even for a high conductivity metal like silver [86, 117, 77]. A dielectric layer between silicon and the metal resolves this problem by reducing the number of long wavelength photons reaching the metal [77, 126, 91]. Thus a rear passivation scheme may also improve the rear side internal reflectance of a cell [86].

In this work, we investigate the potential of the Al_2O_3 passivating nanostructures for photon management when applied to the rear side of a silicon solar cell. A 100 nm thick Ni film is grown on the nanostructured passivation layers, the film representing a nanoscale contact structure shown in Figure 7.2(a). The front side of all the samples are the same, so their total reflectance is correlated
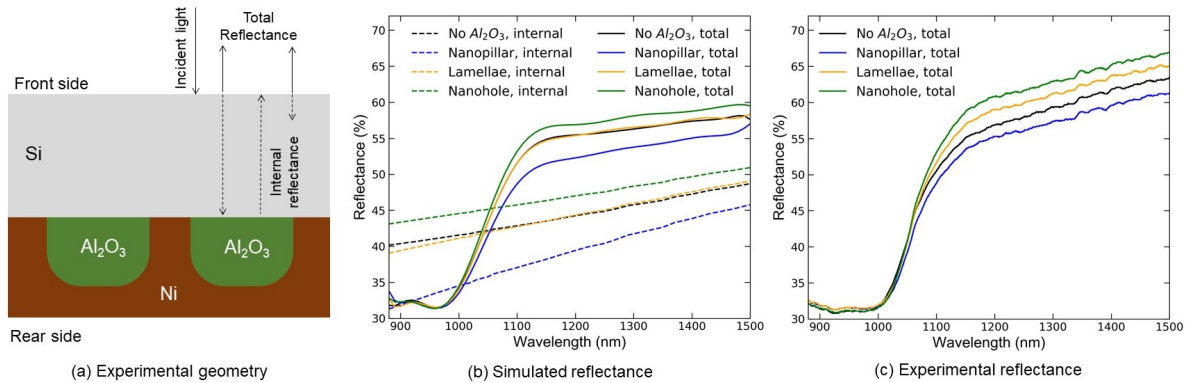
Figure 7.2: Optical behavior of the nanostructured passivation layers at normal incidence of light (a) experimental setup to measure the total reflectance as a function of the variation in the rear side structure, the front side of all the samples being the same (b) simulated results; the internal reflectance was calculated using the finite element method simulation of the rear side and then it was used for calculating the total reflectance using ray tracing simulation of the wafer (c) experimental validation: measured total reflectance.

to the rear internal reflectance. Figure 7.2 illustrates the experimental geometry for reflectance measurement and shows both the simulated and experimental results. For the simulation, the rear internal reflectance was first calculated using frequency domain finite-element method (FEM) simulation by CST Microwave Studio software. The results were then included in ray tracing simulations of the total reflectance using SunSolve [1]. The experimental results clearly follow the same trend as the simulated results; Higher Al_2O_3 area fraction gives higher reflectance. The sample with nanoholes has the highest Al_2O_3 area fraction (67%) among all the nanostructures, so it shows the highest total reflectance. The bare Si shows comparable reflectance as the lamellae structure and more than the nanopillars. This is due to higher light absorption in the Ni-Al_2O_3 effective medium formed by the contacts at lower Al_2O_3 area fractions. However, as the Al_2O_3 area fraction increases, the complex refractive index of that effective medium becomes more and more similar to the full area Al_2O_3 layer, which opposes light reaching into Ni; the reflectance increases as a result. The simulated reflectance of the wafer with and without lamellae Al_2O_3 are comparable, but the experimental results are different. This could be because, the Ni in the FEM

110
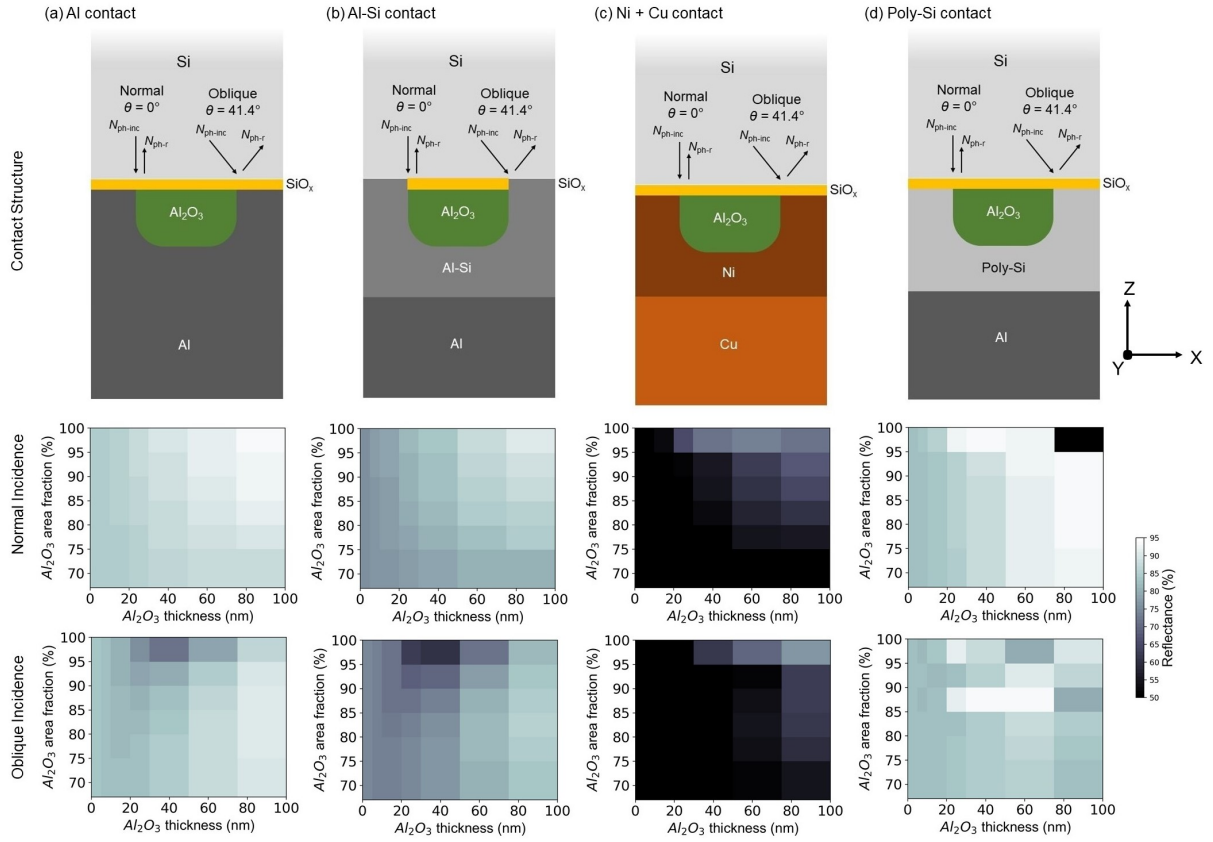
Figure 7.3: Different rear side contact structures featuring the self-assembled nanohole structures and their corresponding rear internal reflectance as a function of passivation area fraction and the nanostructure thickness (calculated for unpolarized light of 1,000 nm wavelength). Both normal and oblique incidence angles of light at the rear surface are considered based on how different front side surface morphologies (e.g., random pyramids, subwavelength black Si) redirect light into the Si absorber.

simulation was more absorptive than the actual Ni used in the experiment. The difference it made was more evident in case of 100% Ni coating (wafer without lamellae or any nanostructure), than 33% Ni coating (wafer with lamellae). The fact that all the simulated reflectance is lower than the corresponding experimental reflectance supports this point. It should also be noted here that because the nanostructures are subwavelength in size, area fraction has more of an impact on the optical properties of these materials than the shape.

The opening in these nanostructured passivation layers facilitates nanoscale contact formation for current collection, and because this is an additive manufacturing process that does not require ablation or etching, it is broadly applicable to virtually any contacting scheme . In this study, we considered four possible contact structures, as illustrated in Figure 7.3: (a) Al; (b) Al-Si; (c) Ni-Cu; and (d) poly-Si. A SiO_2 layer of 2 nm, that formed during processing is assumed in all the contact structures. FEM simulation was conducted to calculate the internal back reflectance corresponding to each of these contact structures for varying thickness (0-100 nm) and area fraction (67%-100%) of Al_2O_3.

In a Si solar cell with subwavelength black Si front side or a tandem cell featuring Si bottom cell, the non-absorbed light comes to the rear side at normal incidence. However, most of the commercial solar cells have a typical random pyramid structure on the front side to enhance light trapping. In such a cell, 76.4% of the non-absorbed light comes to the rear side at an angle of 41.4°, the rest being incident at other angles including the normal direction [118, 36, 88]. Acknowledging the fact that most of the literature describe reflectance characteristics for normal incidence, we divide our study into two parts: normal incidence (popular case) and oblique incidence (41.4°, the dominant case). Keeping in mind that sunlight is randomly polarized, we still calculate the internal reflectance at first for TE and TM sources separately, to clearly understand the influence of different factors involved. Also, considering the typical cell thickness of about 170 μm, most of the shorter wavelength photons get absorbed before they reach the rear side of the cell. Therefore, we consider only longer wavelength photons.

Al is a very common contact material that can be applied to a wide range of Si PV cells [59, 109, 121, 115, 26]. Figure 7.3 (a) demonstrates the average reflectance in terms of nanostructure thickness and passivation area fraction, calculated for 1,000 nm wavelength. For the Al contact, the normal incidence demonstrates the expected trend i.e. increasing Al_2O_3 area fraction and thickness increases the reflectance. However, the reflectance is minimized at oblique incidence for

a thickness around 25 nm, with 95% area passivated. This is attributable to the TM polarization contribution (50% of the incident light), in which increasing the Al_2O_3 thickness initially reduces the reflectance, then increases it, as illustrated in the Supporting Information (SI) section (Figure 7.7); the arrangement here is similar to prism coupling in the Otto geometry [16], where optimum coupling occurs at a certain thickness of the dielectric between the medium of incidence (Si in our case) and the metal. Overall, a thickness and area passivation fraction greater than 85 nm and 95%, respectively, ensure a high reflectance (>90%) from the rear side of the cell.

Figure 7.4 shows the electric field distribution (complex amplitude |E|, including all field components) across the Al contact (67% area passivated) TM polarization cases: (a) normal incidence, 10 nm thickness (b) oblique incidence, 10 nm thickness (c) normal incidence, 50 nm thickness (d) oblique incidence, 50 nm thickness, calculated for 1000 nm wavelength and all shown on the same scale (max |E|=$6x10^8$ V/m, and min |E|=0 V/m). The TE cases are less interesting and are not shown in the figure since there are no surface normal incident fields for any angle, so the fields near the contact are similar to the TM normal incidence case. There is a notable difference between 7.4(a) and 7.4(c): larger fields at the top of the patterned layer, and the position of the interference maximum (horizontal bright band) is closer to the surface in (c) with the patterned layer acting similar to a magnetic mirror (i.e. large field at the surface of the reflector). That suggests we'll get more dissipation i.e. lower reflectance for the thick-film case, for TM polarization. Also, The lack of a dark horizontal band in (b) and (d) is because loosely speaking, the reflection flips the horizontal component of the field, but not the vertical component. As a result, for inclined illumination the position of destructive interference for E_x and E_z shows up at different heights, preventing the formation of a deep interference minimum. For normal incidence illumination there's no reflected E_z, so there's a well-defined height for destructive interference in the standing wave.

Other contact types were also investigated. An Al-Si alloy is included in Figure 7.3(b) based on its use for both full area Al-BSF cells and at the local contacts of PERC cells [134]. The Al-Si

113
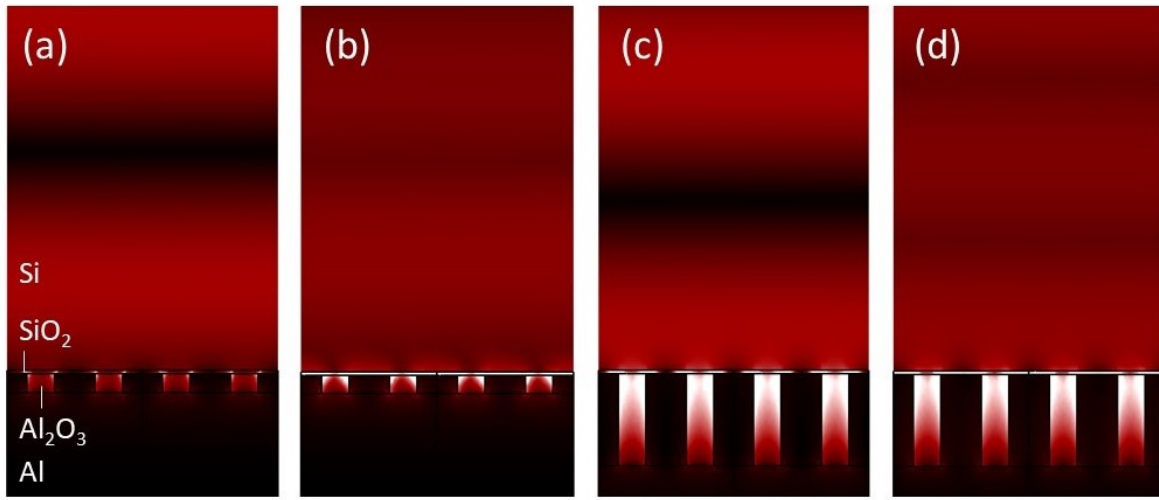
Figure 7.4: Electric field distribution (complex magnitude |E|) in Al contact (67% area passivated) in the rear side of a Si solar cell for two different Al_2O_3 nanostructure thickness, and two angles of incidence, calculated for 1,000 nm wavelength and TM polarization (a) normal incidence, 10 nm thickness (b) oblique incidence, 10 nm thickness (c) normal incidence, 50 nm thickness (d) oblique incidence, 50 nm thickness.

contact demonstrates similar characteristics as the Al contact, but with lower overall reflectance. Ni is another metal of interest; though it is a very lossy metal, it is a common seed layer used when plating Cu [139]. Ni also has a relatively high work function and does not oxidize as readily as Al, so has been used to contact hole-selective materials [71]. The Ni contact in Figure 7.3(c) also shows that increasing passivation area fraction and thickness increases internal reflectance. Finally, poly-Si (Figure 7.3(d)) is considered because poly-Si passivating contacts have gained significant traction within the PV industry due to their ability to dramatically limit contact recombination [51, 52, 169, 42, 74, 28, 105]. The poly-Si exhibits complicated reflectance characteristics unlike the other 3 contacts studied, including a region with low reflectance at high film thicknesses and passivation area fractions. This is due to the emergence of waveguiding effects as Al_2O_3 thickness is increased, as discussed in the SI section (Figure 7.6).

Simulations were carried out using SunSolve to quantify the gain in J_{SC} due to photon management properties of the contacts featuring the nanostructured passivation layer. A random pyramid textured front side with a 75 nm SiN_x ARC and a 170 µm thick Si solar cell was assumed here. For Al contact, the reflectance of the unpassivated surface is around 83% at oblique incidence (dominant case). This gives a J_{SC} of around 38.6 mA/cm^2 (Figure 7.8 in SI section). For any passivated area fraction greater than 67% and Al_2O_3 thickness greater than 80 nm, the internal reflectance climbs above 97% which gives a J_{SC} of around 39.5 mA/cm^2, a gain of 0.9 mA/cm^2. For a lower cell thickness, for example 50 µm, this gain could be around 1.0 mA/cm^2. For the Ni-Cu contact, the reflectance of an unpassivated surface is very low, about 41%. Using a 100 nm thick nanostructured passivation layer with 97% area coverage shows 83% reflectance, which gives a gain of 2.9 and 2.1 mA/cm^2 over the unpassivated surface for 50 µm and 170 µm cell thicknesses, respectively. These values show the potential of our nanostructured passivation layers for improving the J_{SC} of a cell substantially.

Charge Carrier Transport

In most PV cells, photogenerated carriers (electrons and holes) are collected both at the front and rear side of the cell. For passivated surface with partial contacts (e.g., PERC), the carriers have to travel a lateral distance before they can be collected (Figure 7.5(a)), leading to spreading resistance (R_{sb}). The first PERC cells had contact area fractions of about 1% with a contact pitch of 1 mm [15, 68, 14]. In recent years, the contact pitches of PERC cells have ranged from 1 µm to 1 mm with typical contact fractions of 1.5-5% [29, 30]. By forming nanoscale contacts, our nanostructured passivation layer can minimize the distances required for lateral carrier transport.

Figure 7.5(b) shows the R_{sb} versus passivation area fraction calculated using the analytical 2D carrier transport model outlined in [65] and [64]. A bulk resistivity of 1 Ω-cm was assumed for
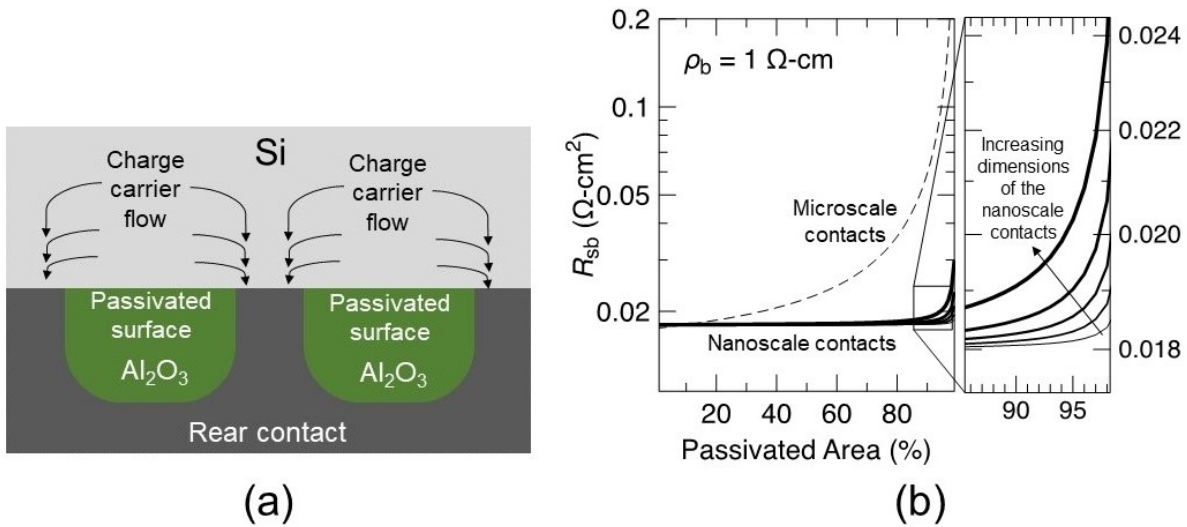
Figure 7.5: Charge carrier transport characteristics in nanostructured contacts (a) Charge carrier transport mechanism in the rear side of a silicon solar cell featuring nanoscale passivated contacts (b) Spreading resistance, R_{sb} in the bulk of the wafer for different contact diameters, nanoscale: 20, 50, 100, 200, 500 nm, and microscale: 50 μm.

this study. For microscale contacts, representative of current PERC cells, the R_{sb} climbs rapidly as we increase passivation area fraction; for 50 μm contact diameter the R_{sb} value reaches around 0.25 Ω-cm^2 at 98% passivated area fraction. In contrast, R_{sb} is far less sensitive to the passivated area fraction for nanoscale contacts: Nanoscale contacts with diameters ranging from 20 to 500 nm achieve more than an order-of-magnitude reduction in R_{sb} (≈ 0.02 Ω-cm^2) compared to microscale contacts for 98% area passivation. These calculations highlight the great potential our nanostructured passivation layer holds for a new generation of partially rear contacted cells.

Conclusion

Multifunctional, nanostructured passivation layers were fabricated in this work using a block copolymer self-assembly method resulting in three different shapes with different Al$_2$O$_3$ area frac-

116

tions: a lamellae structure (48% Al_2O_3 area fraction); nanopillars (28%); and nanoholes (67%). This approach is an additive manufacturing process that does not require etching or laser ablation. Optoelectronic and optical measurements of these structures demonstrate that both surface passivation and improved photon management can be achieved for Si PV cells. Effective carrier lifetimes in the range of 115-147 µs are obtained on Si wafers with the nanostructured passivation layers, compared to less than 5 µs for unpassivated Si wafers. The highest lifetimes are achieved with the nanoholes, since they feature the largest Al_2O_3 area fraction (67%). There is still room to improve the passivation performance in the future by further increasing the Al_2O_3 area fraction and/or modifying the infiltration process to produce hydrogen rich Al_2O_3 [69].

Thicker Al_2O_3 structures with a larger area fraction yield a higher rear internal reflectance and are therefore better equipped to minimize optical losses. This is confirmed both by optical simulations and experimental reflectance measurements, wherein the nanoholes yield the highest internal rear reflectance. Simulations using the experimentally validated model were carried out on four types of contacts: Al; an Al-Si alloy; Ni-Cu; and poly-Si. These simulations confirm that, thicker Al_2O_3 structures with a larger coverage area provide the largest increase in the rear internal reflectance. Various scenarios predict potential increases in the J_{SC} of $\approx$0.9-1.0 mA/cm^2 for Al rear contacts on Si PV cells with 170 µm and 50 µm thick absorbers, respectively, and show increases of 2.1-2.9 mA/cm^2 for Ni-Cu rear contacts.

Future work will aim at the integration of these nanostructures into Si PV cells. Ultimately, the ability to engineer the structure of passivation layers at the nanoscale using scalable self-assembly processes offers the potential to significantly reduce the optical, recombination, and resistivity losses of not only Si PV cells, but other types of PV cells and optoelectronic devices [161].

Experimental Procedure

Fabrication: Block copolymer self-assembly-assisted oxide nanostructure formation

Self-assembled block copolymer (BCP) Al$_2$O$_3$ nanostructures were synthesized on both sides of p-type silicon float zone (FZ) wafers, with a ≈2 nm native SiO$_2$ on it. The thickness and the base resistivity of the wafer were 300 µm and 85-115 Ω-cm respectively.

Materials

A hydroxyl-terminated polystyrene-poly(methyl methacrylate) (PS-*r*-PMMA-OH) random copolymer [60 mol % styrene, determined by ^{13}C NMR, M$_n$ = 9.2 kg/mol, PDI = 1.35 (determined by gel permeation chromatography relative to PS standards)]13 was obtained as a sample from Dow chemical already dissolved in propylene glycol monomethyl ether acetate (PGMEA) and diluted with additional PGMEA to a 1% (w/w) concentration before use. Lamellae-forming 75 kg/mol polystyrene-*block*-poly(methyl methacrylate) (PS-*b*-PMMA; (M$_n$ = 38-37 kg/mol; PDI = 1.08), PMMA cylinder-forming 67 kg/mol PS-*b*-PMMA (M$_n$ = 46.1-21 kg/mol; PDI = 1.09) and PS cylinder-forming 71 kg/mol PS-*b*-PMMA (M$_n$ = 20-51 kg/mol; PDI = 1.07) BCPs were purchased from Polymer Source and used as received. Upon self-assembly, these BCPs form morphologies corresponding to lamellae, nanopillar and nanohole structures, respectively. For film casting, all BCPs were dissolved in toluene at a concentration of 1% (w/w).

BCP Thin Film Self-Assembly

The BCP assembly process was conducted according to previously described methods [41]. Briefly, to promote vertical domain orientation, substrates were grafted with the PS-*r*-PMMA-OH) random

copolymer, which minimizes preferential substrate wetting between the two blocks. First, a random copolymer films were spin-casted onto the substrates at 1500 rpm for 30s. Polymer grafting to the substrates was achieved by baking on a hot plate for 5 minutes at 250°C under continuous N_2 gas purging using a Wenesco hot plate. The excess ungrafted random copolymer was then removed by spin-rinsing the sample with PGMEA at 3000 rpm for 30 s. BCP was then spin-coated at a speed of 3000 rpm and thermally annealed for 5 minutes at 250°C under continuous N_2 gas purging to achieve self-assembly.

Formation of oxide nanostructures

The Al_2O_3 nanostructures were synthesized by vapor phase infiltration approach described previously [106, 131]. Briefly, vapor phase infiltration was performed using four cycles of exposure to trimethylaluminum and water vapor (100 s each) at 85°C in a commercial atomic layer deposition tool (Cambridge Ultratech Savannah S100) with a base pressure of <3 Torr. The chemical selectivity of Al_2O_3 deposition for PMMA moieties means that it is deposited almost exclusively within the PMMA domains. After infiltration, the polymer template was removed by O_2 plasma ashing (March Plasma CS1701F, 100 mTorr, 20 W, 300 s) to reveal alumina replicas of the self-assembled PMMA domain structure.

Metal deposition

To form the contacts, 100 nm thick Ni was deposited on the samples using a Temescal FC-2000 evaporation system.

119

Characterization

Lifetime measurements using photoconductance coil

The samples were annealed at 400°C for 15 minutes to activate the passivation. As a note, the optimal annealing temperature is 350-450°C [39]. The quasi-steady state photoconductance method (Sinton WCT-120) was then used for the measurement of effective carrier lifetime at the excess carrier concentration (Δn) of 10^{15} cm^{-3}.

Scanning electron microscopy (SEM)

A Hitachi 4800 SEM was used for SEM imaging on the samples. It provided the 2D morphology of the nanostructures.

Transmission electron microscopy

The samples were coated with carbon to protect it from any damage from the focused ion beam. STEM was used for TEM images and FTEM for the elemental maps (O_2, SiO_2, Si, Al).

Ellipsometry

A Woollam M2000 Spectroscopic Ellipsometer was used to estimate the area fraction of Al_2O_3 and thickness utilizing an effective medium approximation. The measurement was carried out from 240 nm to 1685 nm wavelength at five different angles of incidence: 50°, 55°, 60°, 65°, and 70°. The acquisition time was 20 s which ensured a very high signal to noise ratio. The acquired data was fitted into optical model to estimate the area fraction using CompleteEASE software.

Reflectance measurement

A reflectance probe based measurement system from StellarNet is used for measuring specular reflectance. The system features a halogen lamp, and Si (shorter wavelength) and InGaAs (longer wavelength) detectors. An aluminum based mirror was used for calibration purpose and the measured data is processed using the actual reflectance data of the mirror found in the data-sheet.

Acknowledgments

Supporting Information: Self-Assembled Multifunctional Nanostructures for Surface Passivation and Photon Management in Si Photovoltaic Cells

Internal reflectance calculation using finite element method simulations for four different contact structures

Figure 7.6 illustrates the internal reflectance characteristics of the the contacts featuring Al_2O_3 nanohole structures. For Al contact, TE polarization (both normal and oblique incidence) shows increase in reflectance with increasing Al_2O_3 thickness. This is because thickening the Al_2O_3 layer inhibits the photons reaching Al, thus reducing the parasitic absorption loss in it and increasing the internal reflectance. Covering more area on the metal surface with Al_2O_3 enhances this effect.
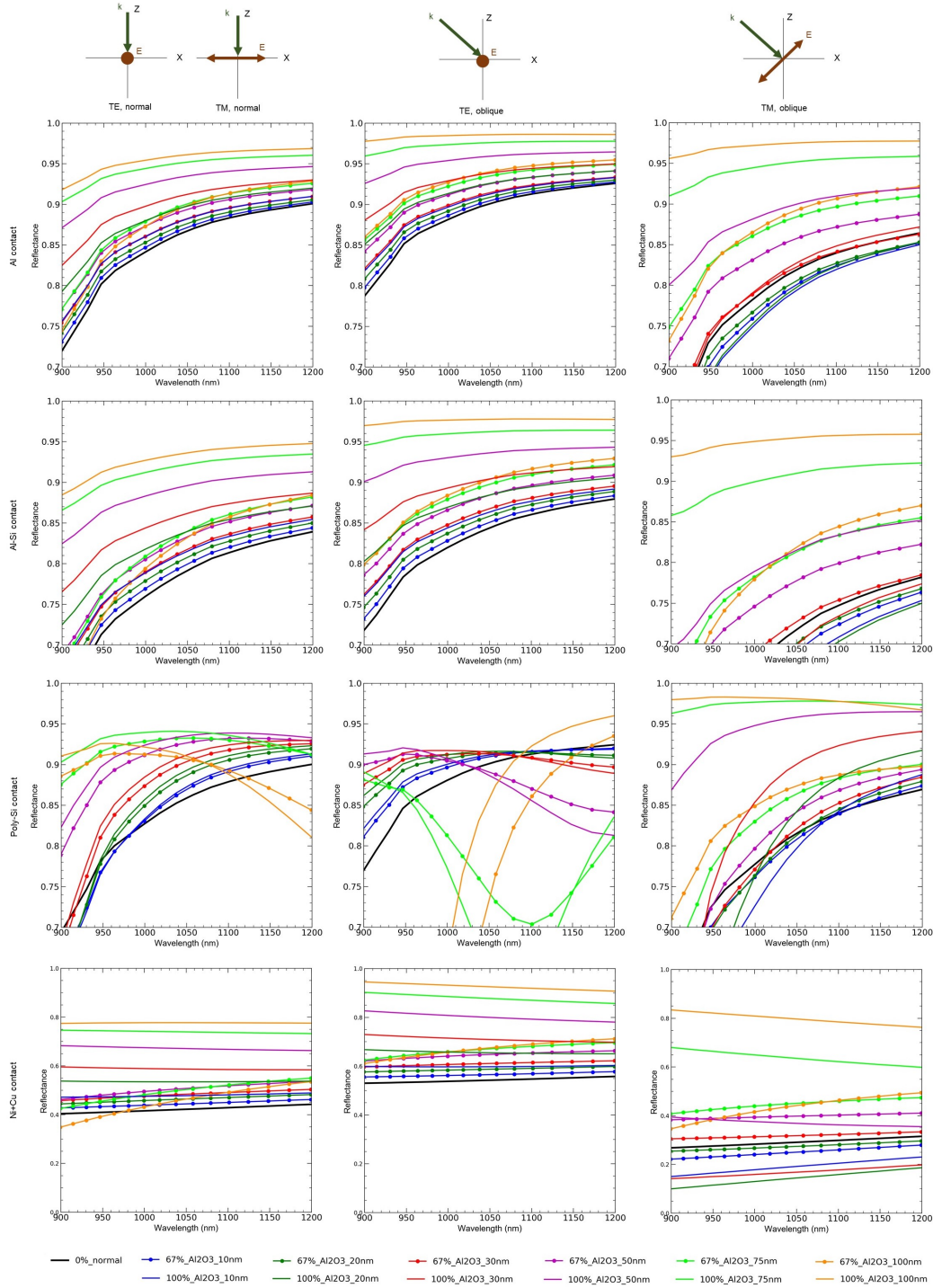
Figure 7.6: Internal reflectance characteristics of four nanostructured contacts used at the rear side of a silicon solar cell: (a) Al; (b) Al-Si; (c) poly-Si; and (d) Ni-Cu. Both TE and TM polarization, and normal and oblique incidence are considered in this study.

Therefore we see that the nanostructured contacts (67% area passivated in this case) show lower reflectance than a full area (100% area passivated) passivated contact. Also, we notice that any passivated area fraction and any thickness gives higher reflectance than no passivation. Following the law of Fresnel reflection, the oblique incidence provides higher reflectance than the normal incidence.

The nanostructured contacts are orderly distributed and sub-wavelength in size. Therefore, the electric field oscillation in case of normal incidence of light experiences the same set of materials for both TE and TM polarization. As a result, the internal reflectance for TM-normal incidence is equal to that of the TE-normal incidence. The TM oblique incidence shows an interesting property. Putting a thin layer of Al_2O_3 (around 5-10 nm) drops the reflectance for the full area passivation, the nanostructured contact following the same trend. Increasing the thickness beyond that increases the reflectance monotonically. The reason of the initial drop in reflectance is not related to the contact morphology, rather to the material properties of the materials involved in the interface. To confirm it, the Fresnel reflection from a stack of Si, Al_2O_3 and Al layers is calculated for 1,000 nm wavelength. As illustrated in Figure 7.7, the TM-oblique incidence shows a drop in reflectance initially then it keeps growing with Al_2O_3 thickness. The arrangement here is similar to the prism coupling in Otto geometry [16], the resonance of which occurs at certain thickness of the dielectric between the medium of incidence (Si in our case) and the metal.

The Al-Si contact shows similar reflectance trends as the Al contact in Figure 7.6. Because the complex refractive index (i.e., n, k values) difference between Si and Al-Si is less than that of Si and Al, the reflectance from Al-Si contact is lower than that of Al contact. One important note here, although the Al-Si contact shows lower reflectance than the Al contact, it provides some surface passivation in addition to working as a better contact structure in terms of charge transport.

The next contact structure in the Figure 7.6 is poly-Si contact. In this case, putting a thin Al_2O_3

123
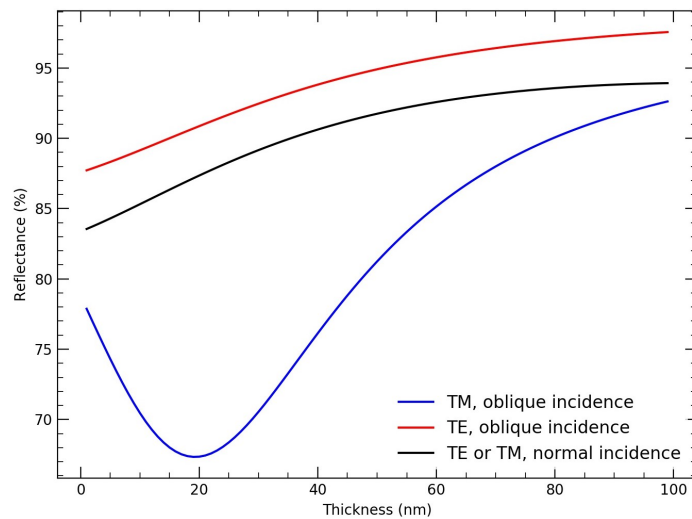
Figure 7.7: Reflectance of a full area Si-Al$_2$O$_3$ contact for different polarization and angle of incidence, calculated for 1,000 nm wavelength using Fresnel equation. TM oblique incidence shows different behavior than the other three cases i.e. the reflectance drops initially with thickness, then increases.

does help the reflectance. However, once the thickness grows beyond 50nm, it creates a waveguide like scenario between Al$_2$O$_3$ and *Al*. Because of this, for higher thickness the reflectance does not stay in a high value for a wider wavelength range. The TM polarization in this case shows more stable reflectance curve than the TE polarization. This is because, to support a waveguide mode, TM polarization requires a thicker waveguide than TE polarization. The improvement in reflectance going from 67% to 100% area passivation was not huge, although it increases to some extent.

The last contact structure in this study is the Ni+Cu contact. It is well known that Ni is a lossy metal. It's great that covering Ni with Al$_2$O$_3$ shows increased internal reflectance, the trend being similar to Al and Al-Si contact i.e., thicker and higher area passivation provides higher internal reflectance.
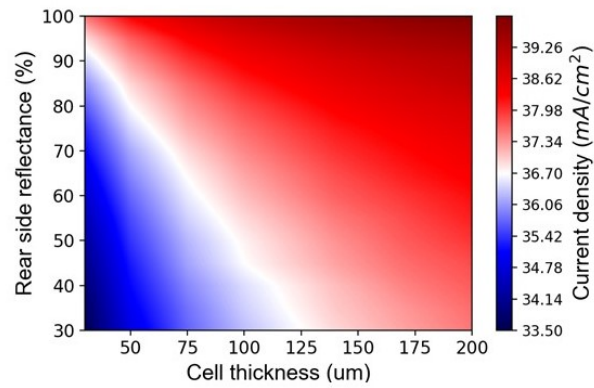
Figure 7.8: Dependence of short-circuit current density on cell thickness and internal reflectance, assuming a random pyramid texture with a 75 nm thick SiN_x anti-reflection coating in the front side of a silicon solar cell.

Influence of cell thickness and rear side reflectance on short-circuit current density

Figure 7.8 demonstrates the J_{SC} contour plot. We observe that the J_{SC} is positively correlated with rear side internal reflectance and cell thickness.

CHAPTER 8: CONCLUSION AND FUTURE WORK

New methods of measurement and mitigation of optical, recombination and resistive losses are introduced in this work. Chapter 1-4 introduced the current trends and challenges in silicon photovoltaics, physics of solar cells, solar cell fabrication methods and issues related to the manufacturing imperfections, and solar cell and module measurement methods.

Chapter 5 presented a new and more accurate method of calculating spatial distribution of solar cell performance parameters. The method relies on the incorporation of short-circuit current density image derived from the quantum efficiency scanning with luminescence images captured at different bias conditions. This method shows that using the global cell J_{SC} with luminescence does not provide an accurate representation of the parameter distribution over the cell. The method developed is excellent for cell parameters; however, as it requires biased photo-luminescence measurement, it is not ideal for module imaging. Future work may therefore take the approach using electroluminescence characteristics only.

Chapter 6 presented a comprehensive methodology to evaluate losses and process variation in silicon solar cell manufacturing. This methodology could be used for process control in a manufacturing environment, where specific defects can be identified, classified, and their impact quantified. Additionally, many of these parameters can be tied back to incoming material quality issues (e.g., poor bulk carrier lifetime, nonuniform wafer doping) or to individual unit processes (e.g., texturing, phosphorus diffusion, silicon nitride deposition, metallization), allowing the data to be used directly for process control in manufacturing or to prioritize cell efficiency optimization efforts. When it provides important insights using one to one correlations among different parameters, further understanding could be derived using a multivariate approach of correlations.

Chapter 7 presents self-assembled nanostructures that mitigate the optical, recombination and re-

sistive losses occuring in silicon solar cells. Using these nanostructures for surface passivation and/or rear side optics in a solar cell is not something found in the literature. In this regard, it is a completely new work. Although they are shown to work in silicon solar cells, they can potentially be used in other optoelectronic devices like light emitting diode, photodetector and sensors. Importantly, at present the nanostructures are sub-wavelength in size, forfeiting the potential advantage of diffraction and scattering in increasing the J_{SC} further. From an optical perspective, ideal nanostructured passivation layers would display feature sizes approaching ≈250 nm. Fortunately, achieving these dimensions using block copolymers is potentially feasible now as a result of recent advances in the self-assembly of ultrahigh molecular weight block copolymer thin films. To summarize, we need to develop a self-assembly based fabrication process that would provide a larger yet nanoscale feature size, still maintaining a passivation area of around 95%. Such a structure would optimize the solar cell performance in terms of surface passivation quality, photon management, carrier transport, and efficiency as a result.

APPENDIX A: COPYRIGHT PERMISSION ELSEVIER
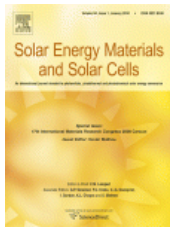
Incorporation of spatially-resolved current density measurements with photoluminescence for advanced parameter imaging of solar cells

Author: Mohammad Jobayer Hossain,Eric J. Schneller,Mengjie Li,Kristopher O. Davis

Publication: Solar Energy Materials and Solar Cells

Publisher: Elsevier

Date: 1 September 2019

Journal Author Rights

BACK   CLOSE WINDOW

APPENDIX B: COPYRIGHT PERMISSION IEEE

A Comprehensive Methodology to Evaluate Losses and Process Variations in Silicon Solar Cell Manufacturing

Author: Mohammad Jobayer Hossain

Publication: IEEE Journal of Photovoltaics

Publisher: IEEE

Date: Sept. 2019

Copyright © 2019, IEEE

Thesis / Dissertation Reuse

The IEEE does not require individuals working on a thesis to obtain a formal reuse license, however, you may print out this statement to be used as a permission grant:

Requirements to be followed when using any portion (e.g., figure, graph, table, or textual material) of an IEEE copyrighted paper in a thesis:

1) In the case of textual material (e.g., using short quotes or referring to the work within these papers) users must give full credit to the original source (author, paper, publication) followed by the IEEE copyright line © 2011 IEEE.
2) In the case of illustrations or tabular material, we require that the copyright line © [Year of original publication] IEEE appear prominently with each reprinted figure and/or table.
3) If a substantial portion of the original paper is to be used, and if you are not the senior author, also obtain the senior author's approval.

Requirements to be followed when using an entire IEEE copyrighted paper in a thesis:

1) The following IEEE copyright/ credit notice should be placed prominently in the references: © [year of original publication] IEEE. Reprinted, with permission, from [author names, paper title, IEEE publication title, and month/year of publication]
2) Only the accepted version of an IEEE copyrighted paper can be used when posting the paper or your thesis on-line.
3) In placing the thesis on the author's university website, please display the following message in a prominent place on the website: In reference to IEEE copyrighted material which is used with permission in this thesis, the IEEE does not endorse any of [university/educational entity's name goes here]'s products or services. Internal or personal use of this material is permitted. If interested in reprinting/republishing IEEE copyrighted material for advertising or promotional purposes or for creating new collective works for resale or redistribution, please go to http://www.ieee.org/publications_standards/publications/rights/rights_link.html to learn how to obtain a License from RightsLink.

If applicable, University Microfilms and/or ProQuest Library, or the Archives of Canada may supply single copies of the dissertation.

BACK   CLOSE WINDOW

LIST OF REFERENCES

[1] Pv lighthouse: Sunsolve.

[2] World energy balances: Data and statistics, 2018.

[3] Fact sheet: President biden sets 2030 greenhouse gas pollution reduction target aimed at creating good-paying union jobs and securing u.s. leadership on clean energy technologies, April 2021.

[4] Solar power market size, share and covid-19 impact analysis, by technology (solar photovoltaic) and concentrated solar power, by application and regional forecast, 2021-2028, 2021.

[5] M. D. Abbott, R. A. Bardos, T. Trupke, K. C. Fisher, and E. Pink. The effect of diffusion-limited lifetime on implied current voltage curves based on photoluminescence data. *Journal of Applied Physics*, 102(4):044502, 2007.

[6] Armin G. Aberle. Surface Passivation of Crystalline Silicon Solar Cells: A Review. *Progress in Photovoltaics: Research and Applications*, 8:473–487, 2000.

[7] Armin G Aberle. Overview on sin surface passivation of crystalline silicon solar cells. *Solar Energy Materials and Solar Cells*, 65(1):239–248, 2001. PVSEC 11 Part I.

[8] Armin G. Aberle. Overview on SiN surface passivation of crystalline silicon solar cells. *Solar Energy Materials and Solar Cells*, 65:239–248, 2001.

[9] Armin G. Aberle, Stephen J. Robinson, Aihua Wang, Jianhua Zhao, Stuart R. Wenham, and Martin A. Green. High-efficiency silicon solar cells: Full factor limitations and non-ideal diode behaviour due to voltage-dependent rear surface recombination velocity. *Progress in Photovoltaics: Research and Applications*, 1(2):133–143, 1993.

[10] International Energy Agency. *Solar Energy Perspectives*. 2011.

[11] G. F. Alapatt, Rajendra Singh, and Kelvin F. Poole. Fundamental issues in manufacturing photovoltaic modules beyond the current generation of materials. *Advances in Optoelectronics*, 2012:1–10, 2012.

[12] Pietro P. Altermatt, Jens Müller, and B. Fischer. A simple emitter model for quantum efficiency curves and extracting the emitter saturation current. 2013.

[13] R. Biswas, J. Bhattacharya, B. Lewis, N. Chakravarty, and V. Dalal. Enhanced nanocrystalline silicon solar cell with a photonic crystal back-reflector. *Solar Energy Materials and Solar Cells*, 94(12):2337 – 2342, 2010.

[14] Andrew Blakers. Development of the perc solar cell. *IEEE Journal of Photovoltaics*, 9(3):629–635, 2019.

[15] Andrew W Blakers, Aihua Wang, Adele M Milne, Jianhua Zhao, and Martin A Green. 22.8% efficient silicon solar cell. *Applied Physics Letters*, 55(13):1363–1365, 1989.

[16] Yu. P. Bliokh, R. Vander, S. G. Lipson, and J. Felsteiner. Visualization of the complex refractive index of a conductor by frustrated total internal reflection. *Applied Physics Letters*, 89(2):021908, 2006.

[17] Freddy Boey, B V R Chowdari, and Subbu S Venkatraman. *50 Years of Materials Science in Singapore*. WORLD SCIENTIFIC, 2016.

[18] Ruy S. Bonilla, Bram Hoex, Phillip Hamer, and Peter R. Wilshaw. Dielectric surface passivation for silicon solar cells: A review: Dielectric surface passivation for silicon solar cells. *physica status solidi (a)*, 214(7):1700293, July 2017.

[19] BP. *Statistical Review of World Energy 2021*. 2021.

[20] O Breitenstein, J Bauer, PP Altermatt, and K. Ramspeck. Influence of defects on solar cell characteristics. *Solid State Phenomena*, pages 1–10, 2009.

[21] O. Breitenstein, J. P. Rakotoniaina, and M. H. Al Rifai. Quantitative evaluation of shunts in solar cells by lock-in thermography. *Progress in Photovoltaics: Research and Applications*, 11(8):515–526, 2003.

[22] Otwin Breitenstein. Local efficiency analysis of solar cells based on lock-in thermography. *Solar Energy Materials and Solar Cells*, 107:381–389, 2012.

[23] Otwin Breitenstein, Jan Bauer, Thorsten Trupke, and Robert A. Bardos. On the detection of shunts in silicon solar cells by photo- and electroluminescence imaging. *Progress in Photovoltaics: Research and Applications*, 16(4):325–330, 2008.

[24] Otwin Breitenstein and Max Planck. Local analysis of the efficiency of solar cells based on dark lock-in thermography imaging. 2012.

[25] Otwin Breitenstein, Chao Shen, Henner Kampwerth, and Martin A. Green. Comparison of dlit- and pl-based local solar cell efficiency analysis. *Energy Procedia*, 38:2–12, 2013. Proceedings of the 3rd International Conference on Crystalline Silicon Photovoltaics (SiliconPV 2013).

[26] Jonathan L. Bryan, Joe V. Carpenter III, Zhengshan J. Yu, Ashling (Mehdi) Leilaeioun, Jianwei Shi, William Weigand, Kathryn C. Fisher, and Zachary C. Holman. Aluminum–silicon interdiffusion in silicon heterojunction solar cells with a-Si:H(i)/a-Si:H(n/p)/Al rear contacts. *Journal of Physics D: Applied Physics*, 54(13):134002, February 2021. Publisher: IOP Publishing.

[27] Nathan L. Chang, Anita Ho-Baillie, Stuart Wenham, Michael Woodhouse, Rhett Evans, Budi Tjahjono, Fred Qi, Chee Mun Chong, and Renate J. Egan. A techno-economic anal-

ysis method for guiding research and investment directions for c-si photovoltaics and its application to al-bsf, perc, ldse and advanced hydrogenation. *Sustainable Energy Fuels*, 2:1007–1019, 2018.

[28] Yifeng Chen, Daming Chen, Chengfa Liu, Zigang Wang, Yang Zou, Yu He, Yao Wang, Ling Yuan, Jian Gong, Wenjie Lin, Xueling Zhang, Yang Yang, Hui Shen, Zhiqiang Feng, Pietro P. Altermatt, and Pierre J. Verlinden. Mass production of industrial tunnel oxide passivated contacts (i-TOPCon) silicon solar cells with average efficiency over 23% and modules over 345 W. *Progress in Photovoltaics: Research and Applications*, 27(10):827–834, 2019.

[29] Jih-Sheng Chiu, Yi-Man Zhao, Sam Zhang, and Dong-Sing Wuu. The role of laser ablated backside contact pattern in efficiency improvement of mono crystalline silicon perc solar cells. *Solar Energy*, 196:462–467, 2020.

[30] Jae Myeong Choi, Beomsic Jung, Jong-Keuk Park, Won Mok Kim, Doh-Kwon Lee, Jeung-hyun Jeong, Taek Sung Lee, Jea-Young Choi, Byeong-Kwon Ju, and Inho Kim. Modified laser-fired contact process for efficient perc solar cells. *Progress in Photovoltaics: Research and Applications*, 27(12):1092–1103, 2019.

[31] Eric W. Cochran, Carlos J. Garcia-Cervera, and Glenn H. Fredrickson. Stability of the gyroid phase in diblock copolymers at strong segregation. *Macromolecules*, 39:2449–2451, 2006.

[32] Andres Cuevas and Di Yan. Misconceptions and misnomers in solar cells. *IEEE Journal of Photovoltaics*, 3(2):916–923, 2013.

[33] Andrés Cuevas and Ronald A. Sinton. Prediction of the open-circuit voltage of solar cells from the steady-state photoconductance. *Progress in Photovoltaics: Research and Applications*, 5(2):79–90, 1997.

[34] Cian Cummins, Ross Lundy, James J. Walsh, Virginie Ponsinet, Guillaume Fleury, and Michael A. Morris. Enabling future nanomanufacturing through block copolymer self-assembly: A review. *Nano Today*, 35:100936, 2020.

[35] Sonali Das, Mohammad Jobayer Hossain, Siu-Fung Leung, Anya Lenox, Yeonwoong Jung, Kristopher Davis, Jr-Hau He, and Tania Roy. A leaf-inspired photon management scheme using optically tuned bilayer nanoparticles for ultra-thin and highly efficient photovoltaic devices. *Nano Energy*, 58:47–56, 2019.

[36] Kristopher O Davis, Kaiyun Jiang, Carsten Demberger, Heiko Zunft, Helge Haverkamp, Dirk Habermann, and Winston V Schoenfeld. Investigation of the internal back reflectance of rear-side dielectric stacks for c-si solar cells. *IEEE Journal of Photovoltaics*, 3(2):641–648, 2013.

[37] Kristopher O. Davis, Marianne P. Rodgers, Giuseppe Scardera, R. Paul Brooker, Hubert Seigneur, Nahid Mohajeri, Neelkanth G. Dhere, John Wohlgemuth, Eric Schneller, Narendra Shiradkar, Andrew C. Rudack, and Winston V. Schoenfeld. Manufacturing metrology for c-si module reliability and durability part ii: Cell manufacturing. *Renewable and Sustainable Energy Reviews*, 59:225–252, 2016.

[38] Matthias Demant, Stefan Rein, Jonas Haunschild, Theresa Strauch, Hannes Höffler, Juliane Broisch, Sven Wasmer, Kirsten Sunder, Oliver Anspach, and Thomas Brox. Inline quality rating of multi-crystalline wafers based on photoluminescence images. *Progress in Photovoltaics: Research and Applications*, 24(12):1533–1546, 2016.

[39] G Dingemans, R Seguin, P Engelhart, MCM van de Sanden, and WMM Kessels. Silicon surface passivation by ultrathin al2o3 films synthesized by thermal and plasma atomic layer deposition. *physica status solidi (RRL)–Rapid Research Letters*, 4(1-2):10–12, 2010.

[40] Gijs Dingemans and WMM Kessels. Status and prospects of al2o3-based surface passivation schemes for silicon solar cells. *Journal of Vacuum Science & Technology A: Vacuum, Surfaces, and Films*, 30(4):040802, 2012.

[41] Gregory S. Doerk and Kevin G. Yager. Rapid ordering in "wet brush" block copolymer/homopolymer ternary blends. *ACS Nano*, 11(12):12326–12336, 2017. PMID: 29195046.

[42] Shubham Duttagupta, Naomi Nandakumar, Pradeep Padhamnath, Jamaal Kitz Buatis, Rolf Stangl, and Armin G. Aberle. monoPoly™ cells: Large-area crystalline silicon solar cells with fire-through screen printed contact to doped polysilicon surfaces. *Solar Energy Materials and Solar Cells*, 187:76–81, December 2018.

[43] Abasifreke Ebong and Nian Chen. Metallization of crystalline silicon solar cells: A review. In *High Capacity Optical Networks and Emerging/Enabling Technologies*, pages 102–109, 2012.

[44] James Ellsmoor. Renewable energy is now the cheapest option - even without subsidies, Jun 2019.

[45] Mehmet Eray Erkan, Vardaan Chawla, and Michael A. Scarpulla. Reduced defect density at the cztsse/cds interface by atomic layer deposition of al2o3. *Journal of Applied Physics*, 119(19):194504, 2016.

[46] Rhett Evans and Matthew Boreland. A multivariate approach to utilizing mid-sequence process control data. In *2015 IEEE 42nd Photovoltaic Specialist Conference (PVSC)*, pages 1–5, 2015.

[47] Rhett Evans and Matthew Boreland. Multivariate data analytics in pv manufacturing—four case studies using manufacturing datasets. *IEEE Journal of Photovoltaics*, 8(1):38–47, 2018.

[48] Rhett Evans, Jonathon Dore, Erik Van Voorthuysen, Jingbing Zhu, and Martin A. Green. Data mining photovoltaic cell manufacturing data. In *2014 IEEE 40th Photovoltaic Specialist Conference (PVSC)*, pages 2699–2704, 2014.

[49] David Feldman, Vignesh Ramasamy, Ran Fu, Ashwin Ramdas, Jal Desai, and Robert Margolis. U.s. solar photovoltaic system cost benchmark: Q1 2020. 2021.

[50] F. Feldmann, G. Nogay, J. Polzin, B. Steinhauser, A. Richter, A. Fell, C. Schmiga, M. Hermle, and S. W. Glunz. A Study on the Charge Carrier Transport of Passivating Contacts. *IEEE Journal of Photovoltaics*, 8(6):1503–1509, November 2018.

[51] Frank Feldmann, Martin Bivour, Christian Reichel, Martin Hermle, and Stefan W. Glunz. Passivated rear contacts for high-efficiency n-type Si solar cells providing high interface passivation quality and excellent transport characteristics. *Solar Energy Materials and Solar Cells*, 120:270–274, January 2014.

[52] Frank Feldmann, Martin Bivour, Christian Reichel, Heiko Steinkemper, Martin Hermle, and Stefan W Glunz. Tunnel oxide passivated contacts as an alternative to partial rear contacts. *Solar Energy Materials and Solar Cells*, 131:46–50, December 2014.

[53] Andreas Fell, Jonas Schön, Matthias Müller, Nico Wöhrle, Martin C. Schubert, and Stefan W. Glunz. Modeling edge recombination in silicon solar cells. *IEEE Journal of Photovoltaics*, 8(2):428–434, 2018.

[54] T. Fellmeth, S. Mack, J. Bartsch, D. Erath, U. Jäger, R. Preu, F. Clement, and D. Biro. 20.1 percent efficient silicon solar cell with aluminum back surface field. *IEEE Electron Device Letters*, 32(8):1101–1103, 2011.

[55] Fabian Fertig, Milan Padilla, Otwin Breitenstein, Hannes Höffler, Ino Geisemeyer, Martin C. Schubert, and Stefan Rein. Short-circuit current density imaging methods for silicon solar cells. *Energy Procedia*, 77:43–56, 2015. 5th International Conference on Silicon Photovoltaics, SiliconPV 2015.

[56] H. Field and A.M. Gabor. Cell binning method analysis to minimize mismatch losses and performance variation in si-based modules. In *Conference Record of the Twenty-Ninth IEEE Photovoltaic Specialists Conference, 2002.*, pages 418–421, 2002.

[57] G. Fischer, M. Müller, H. Wagner, S. Steingrube, and P.P. Altermatt. A combined statistical and tcad model as a method for understanding and reducing variations in multicrystalline si solar cell production. *Energy Procedia*, 27:203–207, 2012. Proceedings of the 2nd International Conference on Crystalline Silicon Photovoltaics SiliconPV 2012.

[58] N. Folchert, M. Rienäcker, A. A. Yeo, B. Min, R. Peibst, and R. Brendel. Temperature-dependent contact resistance of carrier selective Poly-Si on oxide junctions. *Solar Energy Materials and Solar Cells*, 185:425–430, October 2018.

[59] K. C. Fong, T. C. Kho, A. Fell, E. Franklin, N. Zin, A. W. Blakers, K. R. McIntosh, T. Ratcliff, M. Stocks, J. Bullock, and E. Wang. Contact Resistivity of Evaporated Al Contacts for Silicon Solar Cells. *IEEE Journal of Photovoltaics*, 2015.

[60] Kean Chern Fong, Milan Padilla, Andreas Fell, Evan Franklin, Keith R. McIntosh, Teng Choon Kho, Andrew W. Blakers, Yona Nebel-Jacobsen, and Sachin R. Surve. Perimeter recombination characterization by luminescence imaging. *IEEE Journal of Photovoltaics*, 6(1):244–251, 2016.

[61] T. Fuyuki, H. Kondo, Y. Kaji, T. Yamazaki, Y. Takahashi, and Y. Uraoka. One shot mapping of minority carrier diffusion length in polycrystalline silicon solar cells using electroluminescence. In *Conference Record of the Thirty-first IEEE Photovoltaic Specialists Conference, 2005.*, pages 1343–1345, 2005.

[62] Takashi Fuyuki, Hayato Kondo, Tsutomu Yamazaki, Yu Takahashi, and Yukiharu Uraoka. Photographic surveying of minority carrier diffusion length in polycrystalline silicon solar cells by electroluminescence. *Applied Physics Letters*, 86(26):262108, 2005.

[63] Grant P. Garner, Paulina Rincon Delgadillo, Roel Gronheid, Paul F. Nealey, and Juan J. de Pablo. Design of surface patterns with optimized thermodynamic driving forces for the directed self-assembly of block copolymers in lithographic applications. *Mol. Syst. Des. Eng.*, 2:567–580, 2017.

[64] S. Gatz, T. Dullweber, and R. Brendel. Evaluation of series resistance losses in screen-printed solar cells with local rear contacts. *IEEE Journal of Photovoltaics*, 1(1):37–42, 2011.

[65] Boris Gelmont and Michael Shur. Spreading resistance of a round ohmic contact. *Solid-State Electronics*, 36(2):143 – 146, 1993.

[66] M. Glatthaar, J. Haunschild, R. Zeidler, M. Demant, J. Greulich, B. Michl, W. Warta, S. Rein, and R. Preu. Evaluating luminescence based voltage images of silicon solar cells. *Journal of Applied Physics*, 108(1):014501, 2010.

[67] M A Green. Solar cells: operating principles, technology, and system applications. 1 1982.

[68] Martin A Green, Andrew W Blakers, Jianhua Zhao, Adele M Milne, Aihua Wang, and Ximing Dai. Characterization of 23-percent efficient silicon solar cells. *IEEE Transactions on Electron Devices*, 37(2):331–336, 1990.

[69] Geoffrey Gregory, Corbin Feit, Zhengning Gao, Parag Banerjee, Titel Jurca, and Kristopher O. Davis. Improving the passivation of molybdenum oxide hole-selective contacts with 1nm hydrogenated aluminum oxide films for silicon solar cells. *physica status solidi (a)*, 217(15):2000093, 2020.

[70] Geoffrey Gregory, Andrew M. Gabor, Andrew Anselmo, Rob Janoch, Zhihao Yang, and Kristopher O. Davis. Non-destructive contact resistivity measurements on solar cells using the circular transmission line method. In *2017 IEEE 44th Photovoltaic Specialist Conference (PVSC)*, pages 74–78, 2017.

[71] Geoffrey Gregory, Christoph Luderer, Haider Ali, Tamil S. Sakthivel, Titel Jurca, Martin Bivour, Sudipta Seal, and Kristopher O. Davis. Spatial Atomic Layer Deposition of Molybdenum Oxide for Industrial Solar Cells. *Advanced Materials Interfaces*, 7(22):2000895, 2020. _eprint: https://onlinelibrary.wiley.com/doi/pdf/10.1002/admi.202000895.

[72] Siyu Guo, Geoffrey Gregory, Andrew M. Gabor, Winston V. Schoenfeld, and Kristopher O. Davis. Detailed investigation of tlm contact resistance measurements on crystalline silicon solar cells. *Solar Energy*, 151:163–172, 2017.

[73] Felix Haase, Christina Hollemann, Sören Schäfer, Agnes Merkle, Michael Rienäcker, Jan Krügener, Rolf Brendel, and Robby Peibst. Laser contact openings for local poly-si-metal contacts enabling 26.1%-efficient polo-ibc solar cells. *Solar Energy Materials and Solar Cells*, 186:184–193, 2018.

[74] Felix Haase, Christina Hollemann, Sören Schäfer, Agnes Merkle, Michael Rienäcker, Jan Krügener, Rolf Brendel, and Robby Peibst. Laser contact openings for local poly-Si-metal contacts enabling 26.1%-efficient POLO-IBC solar cells. *Solar Energy Materials and Solar Cells*, 186:184–193, November 2018.

[75] Ziv Hameiri, Pooja Chaturvedi, and Keith R. McIntosh. Imaging the local ideality factor by contactless photoluminescence measurement. *Applied Physics Letters*, 103(2):023501, 2013.

[76] Helge Hannebauer, Thorsten Dullweber, Ulrike Baumann, Tom Falcon, and Rolf Brendel. 21.2 percent efficient fineline-printed perc solar cell with 5 busbar front grid. *physica status solidi (RRL) – Rapid Research Letters*, 8(8):675–679, 2014.

[77] F.-J. Haug, T. Söderström, O. Cubero, V. Terrazzoni-Daudrix, and C. Ballif. Plasmonic absorption in textured silver back reflectors of thin film solar cells. *Journal of Applied Physics*, 104(06), 2008.

[78] Jonas Haunschild, Markus Glatthaar, Martin Kasemann, Stefan Rein, and Eicke R. Weber. Fast series resistance imaging for silicon solar cells using electroluminescence. *physica status solidi (RRL) – Rapid Research Letters*, 3(7-8):227–229, 2009.

[79] Jonas Haunschild, Johannes M. Greulich, Hannes Höffler, Sven Wasmer, Gernot Emanuel, A. Krieg, and Lorenz Friedrich. Review of tools and approaches for inline quality control in high efficiency silicon solar cell production. 2017.

[80] Jonas Haunschild, Isolde E. Reis, Teodora Chipei, Matthias Demant, Benjamin Thaidigsmann, Michael Linse, and Stefan Rein. Rating and sorting of mc-si as-cut wafers in solar cell production using pl imaging. *Solar Energy Materials and Solar Cells*, 106:71–75, 2012. SiliconPV.

[81] David Hinken, Klaus Ramspeck, Karsten Bothe, Bernhard Fischer, and Rolf Brendel. Series resistance imaging of solar cells by voltage dependent electroluminescence. *Applied Physics Letters*, 91(18):182104, 2007.

[82] B. Hoex, S. B. S. Heil, E. Langereis, M. C. M. van de Sanden, and W. M. M. Kessels. Ultralow surface recombination of c-Si substrates passivated by plasma-assisted atomic layer deposited Al[sub 2]O[sub 3]. *Applied Physics Letters*, 89:042112–1–042112–3, 2006.

[83] B. Hoex, J. Schmidt, R. Bock, P. P. Altermatt, M. C. M. van de Sanden, and W. M. M. Kessels. Excellent passivation of highly doped p-type Si surfaces by the negative-charge-dielectric Al2O3. *Applied Physics Letters*, 91:112107, 2007.

[84] Zachary C. Holman, Miha Filipič, Antoine Descoeudres, Stefaan De Wolf, Franc Smole, Marko Topič, and Christophe Ballif. Infrared light management in high-efficiency silicon heterojunction and rear-passivated solar cells. *Journal of Applied Physics*, 113(1):013107, 2013.

[85] Zachary C. Holman, Miha Filipič, Benjamin Lipovšek, Stefaan De Wolf, Franc Smole, Marko Topič, and Christophe Ballif. Parasitic absorption in the rear reflector of a silicon solar cell: Simulation and measurement of the sub-bandgap reflectance for common dielectric/metal reflectors. *Solar Energy Materials and Solar Cells*, 120:426–430, 2014.

[86] Zachary C Holman, Stefaan De Wolf, and Christophe Ballif. Improving metal reflectors by suppressing surface plasmon polaritons: a priori calculation of the internal reflectance of a solar cell. *Light: Science Applications*, 2013.

[87] M. J. Hossain. Novel high efficiency quadruple junction solar cell with current matching and optimized quantum efficiency. *ProQuest LLC*, 2016.

[88] M. J. Hossain and K. O. Davis. Photon management for silicon solar cells featuring hole-selective molybdenum oxide rear contacts: An optical simulation study. In *2019 IEEE 46th Photovoltaic Specialists Conference (PVSC)*, pages 1901–1905, 2019.

[89] M. J. Hossain, G. Gregory, H. Patel, S. Guo, E. J. Schneller, A. M. Gabor, Z. Yang, A. L. Blum, and K. O. Davis. Detailed performance loss analysis of silicon solar cells using high-throughput metrology methods. In *2018 IEEE 7th World Conference on Photovoltaic Energy Conversion (WCPEC) (A Joint Conference of 45th IEEE PVSC, 28th PVSEC 34th EU PVSEC)*, pages 2214–2218, 2018.

[90] M. J. Hossain, G. Gregory, E. J. Schneller, A. M. Gabor, A. L. Blum, Z. Yang, D. Sulas, S. Johnston, and K. O. Davis. A comprehensive methodology to evaluate losses and process variations in silicon solar cell manufacturing. *IEEE Journal of Photovoltaics*, 9(5):1350–1359, 2019.

[91] Mohammad Jobayer Hossain, Nafis Iqbal, Gregory Doerk, and Kristopher O. Davis. Enhanced light trapping in carrier selective solar cells using photonic nanostructures. In Balaji Panchapakesan and André-Jean Attias, editors, *Nanoengineering: Fabrication, Properties, Optics, Thin Films, and Devices XVI*, volume 11089, pages 114 – 118. International Society for Optics and Photonics, SPIE, 2019.

[92] Mohammad Jobayer Hossain, Eric J. Schneller, Mengjie Li, and Kristopher O. Davis. Incorporation of spatially-resolved current density measurements with photoluminescence for advanced parameter imaging of solar cells. *Solar Energy Materials and Solar Cells*, 199:136–143, 2019.

[93] Mohammad Jobayer Hossain, Mengdi Sun, Gregory Doerk, Pieter G. Kik, and Kristopher O. Davis. Self-assembled multifunctional nanostructures for surface passivation and photon management in silicon photovoltaics. *Nanophotonics*, 2021.

[94] Mohammad Jobayer Hossain, Bibek Tiwari, and Indranil Bhattacharya. An adaptive step size incremental conductance method for faster maximum power point tracking. In *2016 IEEE 43rd Photovoltaic Specialists Conference (PVSC)*, pages 3230–3233, 2016.

[95] Mohammad Jobayer Hossain, Bibek Tiwari, and Indranil Bhattacharya. Novel high efficiency quadruple junction solar cell with current matching and quantum efficiency simulations. *Solar Energy*, 139:100 – 107, 2016.

[96] Chia-Hsun Hsu, Yun-Shao Cho, Wan-Yu Wu, Shui-Yang Lien, Xiao-Ying Zhang, Wen-Zhang Zhu, Sam Zhang, and Song-Yan Chen. Enhanced si passivation and perc solar cell efficiency by atomic layer deposited aluminum oxide with two-step post annealing. *Nanoscale Research Letters*, 14(1):1–10, 2019.

[97] Xiaobo Hu, Tengfei Chen, Jianyu Hong, Shaoqiang Chen, Guoen Weng, Ziqiang Zhu, and Junhao Chu. Diagnosis of gaas solar-cell resistance via absolute electroluminescence imaging and distributed circuit modeling. *Energy*, 174:85–90, 2019.

[98] Haibing Huang, Jun Lv, Yameng Bao, Rongwei Xuan, Shenghua Sun, Sami Sneck, Shuo Li, Chiara Modanese, Hele Savin, Aihua Wang, and Jianhua Zhao. 20.8 percent industrial perc solar cell: Ald al2o3 rear surface passivation, efficiency loss mechanisms analysis and roadmap to 24 percent. *Solar Energy Materials and Solar Cells*, 161:14 – 30, 2017.

[99] Hannes Höffler, Hasan Al-Mohtaseb, Jonas Haunschild, Bernhard Michl, and Martin Kasemann. Voltage calibration of luminescence images of silicon solar cells. *Journal of Applied Physics*, 115(3):034508, 2014.

[100] Hannes Höffler, Otwin Breitenstein, and Jonas Haunschild. Short-circuit current density imaging via pl image evaluation based on implied voltage distribution. *IEEE Journal of Photovoltaics*, 5(2):613–618, 2015.

[101] ASTM International. Astm g159-98, standard tables for references solar spectral irradiance at air mass 1.5: Direct normal and hemispherical for a 37° tilted surface (withdrawn 2005). 1998.

[102] Sangmoo Jeong, Michael D. McGehee, and Yi Cui. All-back-contact ultra-thin silicon nanocone solar cells with 13.7 percent power conversion efficiency. *Nature Communications*, 4(2950), 2013.

[103] M. K. Juhl and T. Trupke. The impact of voltage independent carriers on implied voltage measurements on silicon devices. *Journal of Applied Physics*, 120(16):165702, 2016.

[104] Bishal Kafle, Abdul Mannan, Timo Freund, Laurent Clochard, Edward Duffy, Marc Hofmann, Jochen Rentsch, and Ralf Preu. Nanotextured multicrystalline al-bsf solar cells reaching 18 percent conversion efficiency using industrially viable solar cell processes. *physica status solidi (RRL) – Rapid Research Letters*, 9(8):448–452, 2015.

[105] Abhijit S. Kale, William Nemeth, Harvey Guthrey, Ellis Kennedy, Andrew G. Norman, Matthew Page, Mowafak Al-Jassim, David L. Young, Sumit Agarwal, and Paul Stradins. Understanding the charge transport mechanisms through ultrathin siox layers in passivated contacts for high-efficiency silicon solar cells. *Applied Physics Letters*, 114(8):083902, 2019.

[106] Jovan Kamcev, David S Germack, Dmytro Nykypanchuk, Robert B Grubbs, Chang-Yong Nam, and Charles T Black. Chemically enhancing block copolymers for block-selective synthesis of self-assembled metal oxide nanostructures. *ACS nano*, 7(1):339–346, 2013.

[107] H. Kampwerth, T. Trupke, J. W. Weber, and Y. Augarten. Advanced luminescence based effective series resistance imaging of silicon solar cells. *Applied Physics Letters*, 93(20):202102, 2008.

[108] Joseph Karas, Lynne Michaelson, Krystal Munoz, Mohammad Jobayer Hossain, Eric Schneller, Kristopher O. Davis, Stuart Bowden, and André Augusto. Degradation of copper-plated silicon solar cells with damp heat stress. *Progress in Photovoltaics: Research and Applications*, 28(11):1175–1186, 2020.

[109] Kamal Katkhouda, Alberto Martinez-Limia, Lutz Bornschein, Radinka Koseva, Torsten Geppert, Andreas Grohe, Hans-Joachim Krokoszinski, and Peter Schaaf. Aluminum-Based Rear-Side PVD Metallization for nPERT Silicon Solar Cells. *IEEE Journal of Photovoltaics*, 4(1):160–167, January 2014. Conference Name: IEEE Journal of Photovoltaics.

[110] Mark J. Kerr, Andres Cuevas, and Ronald A. Sinton. Generalized analysis of quasi-steady-state and transient decay open circuit voltage measurements. *Journal of Applied Physics*, 91(1):399–404, 2002.

[111] Jisoo Kim, Jisun Kim, Jong-Youb Lim, Yeonhee Hwang, Jeongjae Cho, Hoonjoo Choi, and Eunjoo Lee. Laser ablation of aluminum oxide and silicon nitride rear-side passivation for i-perc cell. *Renewable Energy*, 79:135–139, 2015.

[112] Thomas Kirchartz, Anke Helbig, and Uwe Rau. Quantification of light trapping using a reciprocity between electroluminescent emission and photovoltaic action in a solar cell. *MRS Proceedings*, 1101:1101–KK01–04, 2008.

[113] Thomas Kirchartz, Anke Helbig, Wilfried Reetz, Michael Reuter, Jürgen H. Werner, and Uwe Rau. Reciprocity between electroluminescence and quantum efficiency used for the characterization of silicon solar cells. *Progress in Photovoltaics: Research and Applications*, 17(6):394–402, 2009.

[114] Thomas Kirchartz and Uwe Rau. Detailed balance and reciprocity in solar cells. *physica status solidi (a)*, 205(12):2737–2751, 2008.

[115] Takeo Konishi, Koichi Koyama, Keisuke Ohdaira, and Hideki Matsumura. Performance of silicon heterojunction solar cells with various metal-electrodes directly formed on a-Si films without insertion of TCO. In *2018 IEEE 7th World Conference on Photovoltaic Energy Conversion (WCPEC) (A Joint Conference of 45th IEEE PVSC, 28th PVSEC 34th EU PVSEC)*, pages 2036–2038, June 2018. ISSN: 0160-8371.

[116] Kyosung Koo, Hyungju Ahn, Sang Woo Kim, Du Yeol Ryu, and Thomas P. Russell. Directed self-assembly of block copolymers in the extreme: Guiding microdomains from the small to the large. *Soft Matter*, 9(38):9059–9071, October 2013.

[117] Daniel Kray, Martin Hermle, and Stefan W. Glunz. Theory and experiments on the back side reflectance of silicon wafer solar cells. *Progress in Photovoltaics: Research and Applications*, 16(1):1–15, 2008.

[118] Daniel Kray, Martin Hermle, and Stefan W Glunz. Theory and experiments on the back side reflectance of silicon wafer solar cells. *Progress in Photovoltaics: Research and Applications*, 16(1):1–15, 2008.

[119] Mengjie Li, Mohammad Jobayer Hossain, Conner Weik, Nicole Karam Pannaci, Nafis Iqbal, Dylan Colvin, and Kristopher O. Davis. Spatially resolved series resistance analysis of pv modules using electroluminescence and photoluminescence images. In *2021 IEEE 48th Photovoltaic Specialists Conference (PVSC)*, pages 1476–1477, 2021.

[120] Y Lv, YF Zhuang, WJ Wang, WW Wei, J Sheng, S Zhang, and WZ Shen. Towards high-efficiency industrial p-type mono-like si perc solar cells. *Solar Energy Materials and Solar Cells*, 204:110202, 2020.

[121] Christoph Mader, Jens Müller, Sebastian Gatz, Thorsten Dullweber, and Rolf Brendel. Rear-side point-contacts by inline thermal evaporation of aluminum. In *2010 35th IEEE Photovoltaic Specialists Conference*, pages 001446–001449, June 2010. ISSN: 0160-8371.

[122] Yiyong Mai and Adi Eisenberg. Self-assembly of block copolymers. *Chem. Soc. Rev.*, 41:5969–5985, 2012.

[123] Patrizio Manganiello, Marco Balato, and Massimo Vitelli. A survey on mismatching and aging of pv modules: The closed loop. *IEEE Transactions on Industrial Electronics*, 62(11):7276–7286, 2015.

[124] D. L. Meier, E. A. Good, R. A. Garcia, B. L. Bingham, S. Yamanaka, V. Chandrasekaran, and C. Bucher. Determining components of series resistance from measurements on a finished cell. In *2006 IEEE 4th World Conference on Photovoltaic Energy Conference*, volume 2, pages 1315–1318, 2006.

[125] J. Melskens, B. W. H. van de Loo, B. Macco, L. E. Black, S. Smit, and W. M. M. Kessels. Passivating contacts for crystalline silicon solar cells: From concepts and materials to prospects. *IEEE Journal of Photovoltaics*, 8(2):373–388, 2018.

[126] Joachim Müller, Bernd Rech, Jiri Springer, and Milan Vanecek. Tco and light trapping in silicon thin film solar cells. *Solar Energy*, 77(6):917–930, 2004. Thin Film PV.

[127] K.A. Münzera, J. Schöne, A. Teppe, M. Hein, R.E. Schlosser, M. Hanke, K. Varner, H. Mäckel, S. Keller, and P. Fath. Physical properties of industrial 19% rear side passivated al-lbsfr- solar cells. *Energy Procedia*, 8:415–420, 2011. Proceedings of the SiliconPV 2011 Conference (1st International Conference on Crystalline Silicon Photovoltaics).

[128] Jenny Nelson. *The Physics of Solar Cells*. PUBLISHED BY IMPERIAL COLLEGE PRESS AND DISTRIBUTED BY WORLD SCIENTIFIC PUBLISHING CO., 2003.

[129] M. Padilla, B. Michl, B. Thaidigsmann, W. Warta, and M.C. Schubert. Short-circuit current density mapping for solar cells. *Solar Energy Materials and Solar Cells*, 120:282–288, 2014.

[130] R. Peibst, U. Römer, Y. Larionova, M. Rienäcker, A. Merkle, N. Folchert, S. Reiter, M. Turcu, B. Min, J. Krügener, D. Tetzlaff, E. Bugiel, T. Wietler, and R. Brendel. Working

principle of carrier selective poly-Si/c-Si junctions: Is tunnelling the whole story? *Solar Energy Materials and Solar Cells*, 158:60–67, December 2016.

[131] Qing Peng, Yu-Chih Tseng, Seth B Darling, and Jeffrey W Elam. Nanoscopic patterned materials with tunable dimensions via atomic layer deposition on block copolymers. *Advanced materials*, 22(45):5129–5133, 2010.

[132] Florian Pfeffer, Johannes Eisenlohr, Angelika Basch, Martin Hermle, Benjamin G. Lee, and Jan Christoph Goldschmidt. Systematic analysis of diffuse rear reflectors for enhanced light trapping in silicon solar cells. *Solar Energy Materials and Solar Cells*, 152, 4 2016.

[133] Simon Philipps and Werner Warmuth. Photovoltaics report. *Fraunhofer Institute for Solar Energy Systems, ISE*, 2020.

[134] V. A. Popovich, M. Janssen, I. M. Richardson, T. van Amstel, and I. J. Bennett. Microstructure and mechanical properties of aluminum back contact layers. *Solar Energy Materials and Solar Cells*, 95(1):93–96, January 2011.

[135] R Preu, SW Glunz, S Schäfer, R Lüdemann, W Wettling, and W Pfleging. Laser ablation-a new low-cost approach for passivated rear contact formation in crystalline silicon solar cell technology. In *Proceedings of the 16th European Photovoltaic Solar Energy Conference*, pages 1181–1184, 2000.

[136] Ralf Preu, Elmar Lohmüller, Sabrina Lohmüller, Pierre Saint-Cast, and Johannes M. Greulich. Passivated emitter and rear cell—devices, technology, and modeling. *Applied Physics Reviews*, 7(4):041315, 2020.

[137] Uwe Rau. Reciprocity relation between photovoltaic quantum efficiency and electroluminescent emission of solar cells. *Phys. Rev. B*, 76:085303, Aug 2007.

[138] Uwe Rau. Superposition and reciprocity in the electroluminescence and photoluminescence of solar cells. *IEEE Journal of Photovoltaics*, 2(2):169–172, 2012.

[139] Atteq Ur Rehman and Soo Hong Lee. Review of the Potential of the Ni/Cu Plating Technique for Crystalline Silicon Solar Cells. *Materials*, 7(2):1318–1341, February 2014. Number: 2, Publisher: Multidisciplinary Digital Publishing Institute.

[140] Armin Richter, Martin Hermle, and Stefan W. Glunz. Reassessment of the limiting efficiency for crystalline silicon solar cells. *IEEE Journal of Photovoltaics*, 3(4):1184–1191, 2013.

[141] Sven Rissland and Otwin Breitenstein. Considering the distributed series resistance in a two-diode model. *Energy Procedia*, 38:167–175, 2013.

[142] H. Savin, P. Repo, G. von Gastrow, P. von Gastrow, E. Calle, M. Garín, and R. Alcubilla. Black silicon solar cells with interdigitated back-contacts achieve 22.1 percent efficiency. *Nature Nanotechnology*, 10:624–628, 2015.

[143] Jan Schmidt and Armin G. Aberle. Accurate method for the determination of bulk minority-carrier lifetimes of mono- and multicrystalline silicon wafers. *Journal of Applied Physics*, 81(9):6186–6199, 1997.

[144] E. J. Schneller, M. J. Hossain, R. Frota, N. Iqbal, D. Colvin, A. J. Curran, M. Wang, J. L. Braid, L. S. Bruckman, R. H. French, B. D. Huey, J.-N. Jaubert, and K. O. Davis. Spatially resolved characterization of optical and recombination losses for different industrial silicon solar cell architectures. *International Journal of Modern Physics B*, 34(21):2050204, 2020.

[145] Eric J. Schneller, Kortan Öğütman, Siyu Guo, Winston V. Schoenfeld, and Kristopher O. Davis. Crystalline silicon device loss analysis through spatially resolved quantum efficiency measurements. *IEEE Journal of Photovoltaics*, 7(4):957–965, 2017.

[146] D.K. Schroder and D.L. Meier. Solar cell contact resistance—a review. *IEEE Transactions on Electron Devices*, 31(5):637–647, 1984.

[147] Chao Shen, Martin A. Green, Otwin Breitenstein, Thorsten Trupke, Muye Zhang, and Henner Kampwerth. Improved local efficiency imaging via photoluminescence for silicon solar cells. *Solar Energy Materials and Solar Cells*, 123:41–46, 2014.

[148] Chao Shen, Henner Kampwerth, Martin Green, Thorsten Trupke, Jürgen Carstensen, and Andreas Schütt. Spatially resolved photoluminescence imaging of essential silicon solar cell parameters and comparison with cello measurements. *Solar Energy Materials and Solar Cells*, 109:77–81, 2013.

[149] William Shockley and Hans J. Queisser. Detailed balance limit of efficiency of p-n junction solar cells. *Journal of Applied Physics*, 32(3):510–519, 1961.

[150] R.A. Sinton and Andrés Cuevas. A quasi-steady-state open-circuit voltage method for solar cell characterization. In *16th European Photovoltaic Solar Energy Conference*, page 1152–1155, Glasgow, Scotland, 05/2000 2000.

[151] R.A. Sinton and R.M. Swanson. Recombination in highly injected silicon. *IEEE Transactions on Electron Devices*, 34(6):1380–1389, 1987.

[152] Ronald A. Sinton and Andres Cuevas. Contactless determination of current–voltage characteristics and minority-carrier lifetimes in semiconductors from quasi-steady-state photoconductance data. *Applied Physics Letters*, 69(17):2510–2512, 1996.

[153] D. D. Smith, G. Reich, M. Baldrias, M. Reich, N. Boitnott, and G. Bunea. Silicon solar cells with total area efficiency above 25 percent. In *2016 IEEE 43rd Photovoltaic Specialists Conference (PVSC)*, pages 3351–3355, 2016.

[154] Stephan Suckow, Tobias M. Pletzer, and Heinrich Kurz. Fast and reliable calculation of the two-diode model without simplifications. *Progress in Photovoltaics: Research and Applications*, 22(4):494–501, 2014.

[155] B. Tiwari, M.J. Hossain, and I. Bhattacharya. Gap/ingaas/ingasb triple junction current matched photovoltaic cell with optimized thickness and quantum efficiency. *Solar Energy*, 135:618–624, 2016.

[156] T. Trupke, E. Pink, R. A. Bardos, and M. D. Abbott. Spatially resolved series resistance of silicon solar cells obtained from luminescence imaging. *Applied Physics Letters*, 90(9):093506, 2007.

[157] Wei-Chen Tu, Yi-Tsung Chang, Hsin-Ping Wang, Chieh-Hung Yang, Chia-Tze Huang, Jr-Hau He, and Si-Chen Lee. Improved light scattering and surface plasmon tuning in amorphous silicon solar cells by double-walled carbon nanotubes. *Solar Energy Materials and Solar Cells*, 101:200 – 203, 2012.

[158] Vamsi Velidandla, Ben Garland, and Fred Cheung. Automated process metrology in solar cell manufacturing. In *2012 38th IEEE Photovoltaic Specialists Conference*, pages 000489–000495, 2012.

[159] B. Vermang, H. Goverde, A. Uruena, A. Lorenz, E. Cornagliotti, A. Rothschild, J. John, J. Poortmans, and R. Mertens. Blistering in ald al2o3 passivation layers as rear contacting for local al bsf si solar cells. *Solar Energy Materials and Solar Cells*, 101:204 – 209, 2012.

[160] Bart Vermang, Patrick Choulat, Hans Goverde, Jörg Horzel, Joachim John, Robert Mertens, and Jef Poortmans. Integration of al2o3 as front and rear surface passivation for large-area screen-printed p-type si perc. *Energy Procedia*, 27:325–329, 2012.

[161] Bart Vermang, Viktor Fjällström, Jonas Pettersson, Pedro Salomé, and Marika Edoff. Development of rear surface passivated cu(in,ga)se2 thin film solar cells with nano-sized local rear point contacts. *Solar Energy Materials and Solar Cells*, 117:505 – 511, 2013. Dye Sensitized Solar Cells, Organic, Hybrid Solar Cells and New Concepts.

[162] Bart Vermang, Hans Goverde, A Uruena, Anne Lorenz, Emanuele Cornagliotti, Aude Rothschild, Joachim John, Jozef Poortmans, and R Mertens. Blistering in ald al2o3 passivation layers as rear contacting for local al bsf si solar cells. *Solar energy materials and solar cells*, 101:204–209, 2012.

[163] A. Volk, N. Tucher, J. Seiffe, H. Hauser, M. Zimmer, B. Bläsi, M. Hofmann, and J. Rentsch. Honeycomb structure on multi-crystalline silicon al-bsf solar cell with 17.8 percent efficiency. *IEEE Journal of Photovoltaics*, 5(4):1027–1033, 2015.

[164] Lu Wan, Cuili Zhang, Kunpeng Ge, Xueliang Yang, Feng Li, Wensheng Yan, Zhuo Xu, Lin Yang, Ying Xu, Dengyuan Song, and Jianhui Chen. Conductive hole-selective passivating contacts for crystalline silicon solar cells. *Advanced Energy Materials*, 10(16):1903851, 2020.

[165] Hsin-Ping Wang and Jr-Hau He. Toward highly efficient nanostructured solar cells using concurrent electrical and optical design. *Advanced Energy Materials*, 7(23):1602385.

[166] Sven Wasmer, Johannes Greulich, Hannes Höffler, Nico Wöhrle, Matthias Demant, Fabian Fertig, and Stefan Rein. Impact of material and process variations on the distribution of multicrystalline silicon perc cell efficiencies. *IEEE Journal of Photovoltaics*, 7(1):118–128, 2017.

[167] S.R. Wenham and A. Bruce. Analysis and simulation of manufactured screen-printed solar cells. In *Conference Record of the Thirty-first IEEE Photovoltaic Specialists Conference, 2005.*, pages 1659–1662, 2005.

[168] Kenji Yamamoto, Kunta Yoshikawa, Hisashi Uzu, and Daisuke Adachi. High-efficiency heterojunction crystalline si solar cells. *Japanese Journal of Applied Physics*, 57(8S3):08RB20, jul 2018.

[169] Di Yan, Andres Cuevas, James Bullock, Yimao Wan, and Christian Samundsett. Phosphorus-diffused polysilicon contacts for solar cells. *Solar Energy Materials and Solar Cells*, 142:75–82, November 2015.

[170] Y. Yao, J. Yao, V. K. Narasimhan, Z. Ruan, C. Xie, S. Fan, and Y. Cui. Broadband light management using low-q whispering gallery modes in spherical nanoshells. *Nature Communications*, 3(664), 2012.

[171] K. Yoshikawa, H. Kawasaki, W. Yoshida, T. Irie, K. Konishi, K. Nakano, T. Uto, D. Adachi, M. Kanematsu, H. Uzu, and K. Yamamoto. Silicon heterojunction solar cell with interdigitated back contacts for a photoconversion efficiency over 26%. *Nature Energy*, 2, 2017.

[172] K. Yoshikawa, H. Kawasaki, W. Yoshida, T. Irie, K. Konishi, K. Nakano, T. Uto, D. Adachi, M. Kanematsu, H. Uzu, and K. Yamamoto. Silicon heterojunction solar cell with interdigitated back contacts for a photoconversion efficiency over 26 percent. *Nature Energy*, 2(17032), 2017.

[173] Kunta Yoshikawa, Wataru Yoshida, Toru Irie, Hayato Kawasaki, Katsunori Konishi, Hirotaka Ishibashi, Tsuyoshi Asatani, Daisuke Adachi, Masanori Kanematsu, Hisashi Uzu, and Kenji Yamamoto. Exceeding conversion efficiency of 26% by heterojunction interdigitated back contact solar cell with thin film si technology. *Solar Energy Materials and Solar Cells*, 173:37–42, 2017. Proceedings of the 7th international conference on Crystalline Silicon Photovoltaics.

[174] David L. Young, Brian Egaas, Scott Pinegar, and Paul Stradins. A new real-time quantum efficiency measurement system. In *2008 33rd IEEE Photovoltaic Specialists Conference*, pages 1–3, 2008.

[175] David L. Young, Brian Egaas, Scott Pinegar, and Paul Stradins. A new real-time quantum efficiency measurement system. In *2008 33rd IEEE Photovoltaic Specialists Conference*, pages 1–3, 2008.

[176] L. Zeng, Y. Yi, C. Hong, J. Liu, N. Feng, X. Duan, L. C. Kimerling, and B. A. Alamariu. Efficiency enhancement in si solar cells by textured photonic crystal back reflector. *Applied Physics Letters*, 89(11):111111, 2006.

[177] Jia Zhu, Ching-Mei Hsu, Zongfu Yu, Shanhui Fan, and Yi Cui. Nanodome solar cells with efficient light management and self-cleaning. *Nano Letters*, 10(6):1979–1984, 2010. PMID: 19891462.

[178] Yi Zou, Xing Sheng, Kun Xia, Huayu Fu, and Juejun Hu. Parasitic loss suppression in photonic and plasmonic photovoltaic light trapping structures. *Opt. Express*, 22(S4):A1197–A1202, Jun 2014.

[179] Kortan Öğütman, Kristopher O. Davis, Eric Schneller, Vijay Yelundur, and Winston V. Schoenfeld. Integration of spatially resolved ideality factor into local cell efficiency analysis with photoluminescence. *Solar Energy*, 158(C), 12 2017.